DETERMINATION AND MODELING OF RESIDUAL STRESS IN FUNCTIONALLY GRADED WC-Co

by

Leila Tahvilian

A dissertation submitted to the faculty of
The University of Utah
in partial fulfillment of the requirements for the degree of

Doctor of Philosophy

Department of Metallurgical Engineering

The University of Utah

May 2014

The University of Utah Graduate School

STATEMENT OF DISSERTATION APPROVAL

The dissertation of **Leila Tahvilian**

has been approved by the following supervisory committee members:

Zhigang Zak Fang	, Chair	**12/20/2012** Date Approved
K. S. Ravi Chandran	, Co-chair	**12/20/2012** Date Approved
Sivaraman Guruswamy	, Member	**12/20/2012** Date Approved
Daniel O. Adams	, Member	Date Approved
Daniel Belnap	, Member	Date Approved

and by **Manoranjan Misra** , Chair/Dean of

the Department/College/School of **Metallurgical Engineering**

and by David B. Kieda, Dean of The Graduate School.

ABSTRACT

Gradual variations in composition and/or structure through the volume of functionally graded materials (FGMs) generally result in corresponding continuous spatial variations in mechanical/physical properties, and often in significant residual stresses that develop during processing. Due to inhomogeneous properties in these materials, residual stress measurement in FGMs can be a very challenging problem. In this study, residual stresses in functionally graded cemented tungsten carbide (FG-WC-Co) were investigated by numerical, analytical and experimental approaches by means of a layer removal technique. The numerical method consisted of finite element analysis (FEA) modeling for the FGM plate, in order to calculate residual stress distribution over the volume and to develop a method for predicting residual stress levels in closely related materials. The analytical procedure embodied a mathematical approach to determine residual stress distributions, and analytically determined values are compared with those obtained from FEA modeling and experimental results. The experimental approach consisted of fabricating and heat treating FG-WC-Co flat samples, then measuring strain changes by strain gauge after each sequential layer removal from the opposite side of the specimen from the graded region. Good agreement was found between analytical, numerical and experimental results.

Furthermore, thermal residual stress distribution in FG-WC-Co hollow cylinder was examined with an emphasis on the effects of key variables, the gradient profile and

the gradient thickness, on the magnitude and distribution of the stress field. An analytical direct solution based on solving the governing equations of a cylinder composed of a uniform inner core and a functionally graded outer shell was developed. The cylindrical compound was considered as two separate elements: homogeneous cylinder and functionally graded shell. Material properties, such as the elastic modulus and the coefficient of thermal expansion (CTE), were considered to vary as a power function of the radius, and proper mechanical boundary conditions were imposed at the interface of the cylinders.

Finally, having validated the FEA model for the FGM plate, the FEA model approach was investigated for more complex geometries, such as cylindrical and dome-top inserts, and the effects of different design and geometric parameters on the distribution of residual stress are presented.

TABLE OF CONTENTS

CHAPTER 1

INTRODUCTION

Functionally graded materials (FGMs) are composite materials with a continuous variation of composition or microstructure through the graded volume [1-3]. This variation results in a gradient of material properties, such as: mechanical strength, elastic modulus and coefficient of thermal expansion. A number of advantages are attributed to FGMs that make them attractive for industrial applications. Improved residual stress distribution and higher fracture toughness are among the known potential benefits of FGM. These advantages can play a key role in many industrial applications where an enhanced combination of wear resistance and fracture toughness of the mechanical components is demanded [4], and can thus significantly extend the lifetime of components in high wear applications.

Cemented tungsten carbide (WC-Co) is a well-known material used in machining tools and drill bits, due to its superior combination of extremely high elastic modulus and hardness, very high strength, excellent wear resistance, good toughness and very good thermal conductivity [5, 6]. During operations, however, due to its limited fracture toughness, WC-Co can be prone to chipping which often leads to catastrophic fracture of the components. Fracture toughness and hardness of WC-Co are inversely related; therefore, as hardness and wear resistance of WC-Co are improved, fracture toughness

tends to decrease. Because of its use in high wear applications, it is a long-term goal within this materials system to improve the hardness and accordingly, the wear resistance of WC-Co without sacrificing toughness. Since, these mechanical properties are traditionally controlled either by the WC grain size or the Co content, it is appealing to obtain a graded microstructure that provides a hard surface while maintaining a fracture resistant bulk composition.

A new method to manufacture graded WC-Co, based on a novel carburizing heat treatment, was developed by Fang *et al* [7]. In this method, a gradient of carbon content initiates Co migration away from the surface, resulting in an FG material with decreased Co and increased WC at the surface, and local composition gradually transitioning through the graded region to the underlying bulk composition. This gradient results in a variation of elastic modulus, hardness and coefficient of thermal expansion through the FG region.

Nonlinear spatial variations in the thermal expansion coefficient create thermal residual stresses in the graded WC-Co. During heat treatment, as the material cools to room temperature, different areas in the graded region shrink by different values due to variations in composition/microstructure as a function of position. This results in residual stresses forming in the graded region and in the substrate. These stresses can be tensile or compressive and can be significantly adjusted and engineered by control of the compositional gradient and thickness of the graded region during processing, both of which affect local elastic modulus and distribution of residual stresses. These factors significantly raise the level of complexity of the thermo-elastic analysis of such materials. It was shown, however, that graded WC-Co improved the fatigue life and the mechanical

performance of WC-Co tools compared to conventional WC-Co microstructures [8], and it was hypothesized that residual stress at the surface played a key role in the enhanced properties of the graded material. Therefore, determination of the residual stress distribution patterns in graded WC-Co may have practical advantages for understanding and further improving properties in this system.

Among different residual stress measurement techniques, X-ray and neutron diffraction have been commonly used for residual stress determination of WC-Co [9-14]. In these studies, measurements were accomplished on the surface and for homogeneous WC-Co with constant mechanical properties throughout the material volume.

Larsson and Oden [15] determined the residual stress state as a function of depth by measuring the stress at the surface using X-ray diffraction, and then removing material incrementally between measurements. However, there are problems and limitations with X-ray and neutron diffraction techniques as applied to graded materials and coatings. These include issues related to penetration depth, measurement resolution and strain sensitivity, and are examined in more detail elsewhere.

The layer removal technique (LRT), on the other hand, is also a well known technique for measuring residual stress since the mid-1940s when it was used for metals [16]. Then this technique was modified and used for thermal spray coatings [17] and after that for laminated composite [18]. This method was also used by Virkar [19] for ceramic materials. However, in all of the previous work, layer removal was used for constant homogeneous materials with constant elastic modulus and coefficient of thermal expansion. Recently, Ravi Chandran [20] developed an analytical model of layer removal technique for functionally graded materials. In this model, for FGMs, when the elastic

modulus varies as a function of depth, an elasticity theory relating the changes in back-face-strain to the residual stress was developed.

The present dissertation is in two parts. The first part focuses on the residual stress distribution in the FGM plates. In this part, Chapter 3, the layer removal technique was used for the first time to determine the residual stress distribution in functionally graded WC-Co flat specimens, which were fabricated using the carburizing heat treatment technique, mentioned earlier [7]. Also, a finite element model was developed to simulate the LRT numerically. For a fairly wide range of graded WC-Co specimen thicknesses with different gradient profiles and gradient thicknesses, back-face-strain was measured using LRT of the graded region, and stresses were also determined by finite element analysis (FEA).

The second part of this dissertation discusses the residual stress distribution of the other geometric shapes of FGMs. The distribution of residual stress was determined not only by the gradient of material composition, but also by the geometric shape of the component, such as: cylindrical and domed top. Cylindrical tubes and rods are among the most common shapes for components made of cemented tungsten carbide, and residual stress distribution in a hollow cylinder was thus selected as a representative geometry in this study. An additional advantage of choosing a simple geometry is the capacity to derive analytical solutions that may illuminate the understanding of residual stress in a broader range of geometries and applications.

In the FGM hollow cylinders, the displacement, residual strain and stress are spatially dependent, since the material properties are a function of position due to changes in local composition within the graded region. To determine the residual stress,

numerous solutions of the governing equations for FGM have been developed by researchers during the last two decades. Despite the fact that several studies have been done on FGM cylinders [21-22], the existing solutions cannot be directly used for a compound cylinder composed of a FGM outer shell and a uniform internal core because those solutions were only applicable to the specific geometries from which they were derived, and the boundary conditions were also different for various situations. Using general methodologies, however, solutions to the present problem of residual stresses in FG-WC-Co were derived.

In Chapter 4, a direct solution of the governing equations for the thermal stress and displacement in a compound FGM cylindrical component is presented. In this study, a long hollow compound FGM cylinder under a uniform thermal loading was considered. The compound cylinder was simplified by breaking it into two separate elements: a homogeneous cylinder and a FGM cylinder. Mechanical and thermal boundary conditions were also defined at the interface of the homogeneous and heterogeneous regions, and external pressure alone was also considered. The properties of the FGM cylinder were assumed to follow power functions of the radius.

In the specific case of a hollow cylinder, the compositional variation is represented by the gradient profile and described by a power function of radius. Because of the compositional gradient, the elastic modulus (E) and the coefficient of thermal expansion (CTE) also vary following power functions of radius. Hence, the magnitude and the distribution of the different components of the residual stresses, specifically radial stress and hoop stress, were studied as a function of different types of compositional gradients. The effect of gradient thickness representing the key variable of the FGM

design was also investigated. The ratio of the gradient thickness to the internal radius of the cylinder, H/a, was studied in the analytical derivation as a prescribed key variable.

CHAPTER 2

LITERATURE REVIEW

2.1 Overview

Functionally graded materials (FGMs), as an advanced class of composites, bring significant progress in the performance of materials, which have been used under extreme conditions such as high temperature, corrosion, biological systems and other nontraditional environments [23-27]. Gradual changes in composition, microstructure, porosity, texture and/or phase transformation feature the concept of FGM, which results in a variation in the mechanical and physical properties of a given FGM material [4, 28-31].

To maximize the functionality of FGMs, dissimilar constituents, such as ceramic and metal are combined to make graded cer-met composite [32]. Graded cer-met usually consists of ceramic particles embedded in a metal matrix with a gradual variation in its composition/microstructure such that the volume fraction of ceramic in the composite changes while it moves from one side to the other. Consequently, a unique material with a superior combination of material properties, which benefits the characteristics of both ceramic and metal, is created.

Cemented tungsten carbide (WC-Co) is a cer-met widely used in machining, oil drilling, mining, construction, and other industrial applications. In all of these

applications, WC-Co components are prone to suffer from catastrophic fractures due to the relatively low fracture toughness of WC-Co materials [33-34]. Graded-WC-Co is a composite consisting of WC particles embedded in Co matrix with a Co composition that changes from surface to interior. The compositional gradation is introduced to improve the performance of WC-Co tools/bits [35-39]. Due to the cobalt gradient, hence the mismatch between mechanical properties, the distribution of residual stresses in graded-WC-Co varies significantly by gradient profile. The performance of graded-WC-Co component is affected strongly by the distribution of residual stresses.

Residual stresses are generated in functionally graded materials or coating upon cooling from high temperature processing conditions due to the through-thickness variation in elastic modulus (E) and thermal expansion coefficient (α) [40]. Such variations can be intentionally extreme because of the need to achieve certain mechanical properties [41]. Generally, residual stress calculations are one of the most common subjects in the FGM literature [4, 29].

The source of residual stress in a typical FGM structure can be thermal and/or mechanical loading, including static and dynamic loadings. Thermal mismatch between the constituent materials, such as ceramic and metal phases in a cer-met FGM, causes residual stresses to form during temperature changes experienced in both manufacturing and in-service stages. Since the mentioned stresses may cause damage onset and crack propagation, and therefore can affect the lifetime of components especially at high temperature, the temperature distribution in the material and associated thermal stresses at both macromechanical and micromechanical levels during its lifetime should also be considered. In addition, other material properties mismatches, such as modulus of

elasticity and Poisson ratio, between constituent materials creates mechanical residual stress in the FGM structure [42-47].

As discussed in the scientific literature, numerous techniques have been used to study the thermal and mechanical behavior of FGMs. In order to get thermomechanical response, in some investigations, FGMs have been simplified to multiphase materials and modeled at different microscopic and continuum levels using a variety of analytical, computational and experimental approaches [42-47]. A large variety of materials have been the subject of all this research but to the best of our knowledge, there has been no previous numerical, analytical and experimental comprehensive study on the residual stress calculation and prediction of the functionally graded WC-Co drilling bits.

2.2 Functionally Graded Materials (FGMs)

The concept of "functionally graded materials (FGMs)" was originally created in material science and engineering in Japan in the mid-1980s in a national program aimed at developing material for aerospace applications [1]. Before that, General Motors Corporation in 1972 had used a similar concept in fabrication of thermal barrier coatings in diesel engines for its trucks [48]. In addition, the concept of grading visco-plastic materials was explored by several researchers to improve the damping performance in the development of aerospace structures [49].

By definition, FGMs are composite materials in which the composition and/or microstructure of the material may vary, continuously or in discrete steps, with depth beneath a free surface [1]. These changes result in a gradient in the mechanical properties of the materials such as elastic modulus and coefficient of thermal expansion. The main characteristic of this new generation of composites is to provide the design, engineering

and manufacturing of certain materials with special material properties for specific industrial applications that cannot usually be found in ordinary homogeneous materials. In many engineering applications, components are subjected to different loading environments, which sometimes require them to possess certain material properties in order to perform well in service. High strength tools such as drilling bits, which are required to possess a tough core to withstand the torque from the drilling process as well as a very hard surface with high wear resistance to avoid delamination and to postpone any type of chipping and fracture of the bit inserts, are good examples of the industrial demand in this field of engineering. The concept of FGM is claimed to be an appropriate response to such industrial demands and applications.

Typically, FGMs are associated with particulate composites where the volume fraction of particles varies in one or several directions. FGMs may also be developed using fiber-reinforced layers with a volume fraction of fibers that is coordinate dependent, rather than constant [50-51]. In this study, particulate FGM is under consideration. Particulate FGMs are heterogeneous due to spatial variations of volume fractions of the phases, while they may be isotropic locally at specific positions. FGMs usually are made from a ceramic and a metal or a combination of different metals. Ceramics possess high hardness, excellent wear resistance and high thermal resistance, but low fracture toughness, low strength and low thermal conductivity. On the other hand, metals possess high modulus, strength and high fracture toughness, but poor wear resistance and hardness. Figure 2.1 illustrates a schematic of the architecture of particulate FGMs, where spherical or nearly spherical ceramic particles are embedded within an isotropic metal matrix [52].

The variation of volume fraction of ceramic in the metal matrix results in a gradient in the mechanical properties of the materials, such as elastic modulus and coefficient of thermal expansion. Variation in mechanical properties creates the opportunity for obtaining a superior material properties combination through the gradient design of the material constituents, therefore, FGM has been raised as an interesting field of study in recent decades. These materials are currently in the forefront of material investigations, garnering worldwide attention. A broad range of applications are appropriate for FGMs, including: biomechanical, automotive, aerospace, mechanical, civil, nuclear, and naval engineering. The wide range of industrial applications are due to the beneficial advantages of FGMs, such as:

- Improved residual stress distribution
- Reduced stresses through the thickness
- Reduced stress intensity factor
- Enhanced thermal properties
- Higher fracture toughness
- Elimination of stress discontinuity in laminated composites

2.3 Cemented Tungsten Carbide (WC-Co)

As a well-known cer-met, cemented tungsten carbide is composed of a hard, brittle ceramic, (WC), embedded in a tough ductile metal matrix (Co). Figure 2.2 illustrates a typical microstructure of WC-10 wt. % Co. The WC-Co microstructure is made of angular and hard WC grains that are nearly completely surrounded by ductile Co binder formed either by liquid phase sintering (LPS) of WC/Co under vacuum or by LPS

followed by a low pressure hot iso-static pressing (Sinter HIP). In Figure 2.2, the lighter phase is the WC, while the darker phase is the Co binder. Owing to their unique combinations of high modulus, strength, and moderate fracture toughness, cemented tungsten carbides (WC-Co alloys) are widely used for demanding applications, including cutting tools, rock drill bits, and other high wear-inducing environments [53-56]. Products are successfully produced commercially with a high degree of control and reliability in mechanical properties.

Crucial mechanical properties of WC-Co composite mainly include hardness, transverse rupture strength (TRS), and fracture toughness. Hardness ranges from 850 to 2000 kg/mm^2 (Vickers hardness, 30kgf, H_V), toughness ranges from 9.0 to 25.0 MPa (critical stress intensity factor, plane strain fracture toughness, K_{IC}) and fracture strength of WC-Co composites ranges from 1.5 to 4.0 GPa (transverse rupture strength, TRS). Like all other composite materials, the mechanical properties of cemented tungsten carbide are strongly influenced by their microstructural parameters.

2.4 Functionally Graded Cemented Tungsten Carbide (FG-WC-Co)

Rock drill bit cutting inserts, which are usually made of cemented tungsten carbide, are prone to suffer from chipping during operations. This is often the cause of a catastrophic fracture of the components, due to the low fracture toughness of WC-Co materials [27]. Mechanical properties of WC-Co, such as toughness and hardness of WC-Co, are controlled either by the WC grain size or the Co content. Due to the inverse relation between the hardness and toughness (Figure 2.3), it is always desirable to improve the hardness and accordingly, the wear resistance of WC-Co without sacrificing

FG-WC-Co is a WC-Co composite in which Co composition and/or WC grain size changes from the surface to a specific depth of the bulk. For example, a WC-Co with lower cobalt content near the surface and higher cobalt content in the core provides FG-WC-Co with a hard-surface-tough-core structure [36-38]. Such a hard-surface-tough-core structure creates a supreme combination of high wear resistance and high fracture toughness in a single component. Significant rise to the performance of the graded WC-Co component is gained in comparison to the homogeneous WC-Co materials [39]. The microstructure of FG-WC-Co is shown in Figure 2.4. The variation of dark phase, which is the Co phase, is shown in this figure. Also, a gradient of Co content with respect to depth is shown in this figure.

This gradient results in a variation of elastic modulus, hardness and coefficient of thermal expansion, which improved wear resistance at the surface while the fracture toughness stayed constant within the bulk of the material. This gradient causes thermal residual stress in the material.

2.5 Fabrication Process of FG-WC-Co

Fabrication methods of FG-WC-Co are classified into two major categories of: powder consolidation process and atmosphere heat treatment process. In the first class, a powder compact is built using different layers, in which each layer possesses different grain size, or Co composition, or carbon composition or a combination of the above. Then the powder compact is consolidated/sintered to full density [57-58]. A variety of methods, such as die compaction, injection molding, electrophoretic deposition, and tape casting etc., are available for producing powder compacts with gradients [57-61].

The second major class of FG-WC-Co fabrication methods is atmosphere heat treatment process, which relies on natural phenomenon of mass transport to create compositional gradients in WC-Co components by controlling atmospheres during sintering or postsintering heat treatment [62-63]. As a new technique in this class of FG-WC-Co manufacturing methods, a novel carburizing heat treatment technique was developed by Fang *et al* [7]. In this method, a gradient of carbon content initiates Co migration away from the surface, resulting in an FG material with decreased Co and increased WC at the surface, and local composition gradually transitioning through the graded region to the underlying bulk composition. This gradient results in a variation of elastic modulus, hardness and coefficient of thermal expansion through the FG region.

2.6 Residual Stress in FGMs

Residual stress by definition is the stress that remains in a stationary body while it is in equilibrium with its surroundings. Residual stress can be detrimental or beneficial to the performance of the material or the life of the component, depending on the application and type of the residual stress [64]. In some cases compressive stresses are deliberately created to improve the component life. For instance, compressive stress in tools that are subjected to wear often benefit the fracture life of the components. This is more significant in the multiphase materials in which residual stress can arise from the differences in elastic modulus, thermal expansion and stiffness.

In functionally graded materials, the gradient in material properties is generally the primary source of residual stress generation through the volume of the material. To benefit the advantages of FGMs from the residual stress point of view, this subject has

been taken into consideration by researchers over the last two decades. FGM has been used to redistribute and reduce thermal stresses [65, 66], thereby limiting the stresses at critical locations and thus suppressing the onset of permanent (plastic) deformation, damage, or cracking [67, 68]. Reduction in stress concentration can also occur because of graded transitions at the intersection between an interface and a free surface [69, 70]. Similarly, by altering the gradients in elastic and plastic properties across the interface, the local driving force for crack growth across an interface can be increased or reduced [71, 72]. Smooth transitions in composition across an interface also improve interfacial bonding between dissimilar materials [73].

Getting more wear and damage resistance in the material, particularly at the surfaces, higher fracture toughness inside the material and greater crack growth resistance between the dissimilar materials are demanded in industrial applications, such as: gas and oil industries, power plants, rock cutting inserts and mining.

2.7 Methods of Measuring Residual Stress in FGMs

2.7.1 Overview

Residual stress considerations within FGM structures have been studied extensively, both experimentally and through computer simulations [74-77]. This has been a consuming topic for researchers from the inception of FGMs, since these residual stresses have significant roles affecting the performance of the FGMs. Most of the previous research has centered on modeling efforts due to the difficulties and uncertainties related to the mechanical testing of FGMs. However, limited experimental determination of residual stresses has been achieved in the study of these materials. The

experimental methods for measuring residual stresses generally tend to fall within two categories; first, nondestructive analysis technique (X-ray, neutron, fluorescence, etc.) and second, destructive mechanical techniques.

2.7.2 Nondestructive Methods

The nondestructive techniques seek to correlate the residual stresses within the microstructure to differences between the interaction of the energy beams and the atomic structures in the material. For example, X-ray or neutron interaction measure differences in the lattice length between bonded and unbonded layer compositions. Any observed changes are assumed to correspond to the residual stress in the respective matrixes [78, 79].

X-ray diffraction (XRD) has been used in WC-Co composite by a number of researchers. French [9] studied the affective factors on the stress measurement of WC-Co by different XRD techniques and expressed a clear explanation of the measurement procedure. French also [10] analyzed the effect of Co content on temperature induced stresses and predicted lower compressive stress with increasing Co content. This was in disagreement with previous theories. Other authors used neutron diffraction to measure residual stress in WC-Co composites. Krawitz *et al.* [11], Mari *et al.* [12] and Coats and Krawitz [13] used this technique to determine the average stresses in the WC phase of a homogeneous WC-Co. In another study, Delfosse *et al.* [14] determined compressive residual stresses using XRD in the WC phase in multilayer WC-Co samples, where each layer had constant WC and Co contents. Finally, Larsson and Oden [15] used XRD in a functionally graded WC-Co to determine the 3-dimensional residual stress state as a

function of depth.

2.7.3 Mechanical Stress Measurement Method

These methods are based on the monitoring of changes in component distortion, either during the generation of the residual stress, or afterwards, by deliberately removing material to allow the stress to relax.

2.7.3.1. Curvature

These methods are usually used to determine the stress within coatings and layers. The deposition of a layer can cause the substrate to bend. The changes in curvature during deposition make it possible to calculate variations in stress as a function of deposit thickness. Curvature measurements can also be used to determine the stresses by incremental layer removal. This has been used for metallic and polymeric composites, and for thin coatings produced using chemical and physical vapor deposition (CVD and PVD). Since the stress distribution associated with a given curvature is not unique, there is some ambiguity in this approach.

2.7.3.2. Hole Drilling

The undisturbed portions of a stressed sample will relax into a different shape when such a region is machined; this provides data for the calculation of residual stress. The machining operation involves drilling a hole, around which the strain is measured. Although it is possible to infer the variation in stress with depth by incrementally deepening the hole, it is difficult to obtain reliable measurements when the depth is

beyond the size of the diameter. This method is, however, cheap and widely used. If the residual stresses exceed 50% of the yield stress, localized yielding can introduce errors. Although the method is used for coatings, it is not practical for thin (<100μm), or brittle coatings.

2.7.3.3 Compliance Methods

The crack compliance method involves cutting a small slot to determine the relaxation of stress in the vicinity of the crack using a strain gauge interferometer. Increasing the depth of the slot allows the stress field normal to the crack to be resolved as a function of depth for relatively simple stress distributions.

2.7.3.4 Ultrasonic Methods

Changes in ultrasonic speed can be observed when a material is subjected to a stress, the changes providing a measure of the stress averaged along the wave path. The acoustoelastic coefficients necessary for the analysis are usually calculated using calibration tests. Different types of waves can be employed, but the commonly used technique is the critically refracted longitudinal wave method. The greatest sensitivity is obtained when the wave propagates in the same direction as the stress.

2.7.3.5 Layer Removal Technique

Layer removal technique was developed for the first time in 1945 by Rosenthal and Norton [80]. This method was based on unbalancing the force and momentum equilibrium due to removing material and observing the resulting deformation on the

remaining material. In 1951, Treuting and Read [81], presented another treatment of this method for determining the biaxial residual stress in a sheet material by removing successive uniform layers of material from the surface of a test specimen and measuring the resulting curvature In this study, based on the equilibrium, a stress versus curvature relation was derived, based on the depth of material removed. Isotropic material behavior and constant material properties over the specimens under experiment was assumed in this approach. Although this study has been used and referenced by numerous researchers over several decades, considerable difficulties and uncertainties regarding the stress-curvature relation and the measurement technique exist. Using the analysis described by Treuting and Read, many studies have been published without significant changes in the original work, on measurement of thermoplastic residual stresses in the form of bars, plaques or sheets [82-90]. For example, in 1958, Mura *et al.* used this technique to measure quenching stresses in a bearing ring. Small modifications were considered to match small changes with respect to geometry changes and new boundary conditions [91]. Also, in 1968, Rathun and Coffin employed this technique for measuring residual stress in quenched plate [92]. Lake, in a separate attempt, followed a similar method using hole drilling in residual stress measurement [93].

Layer removal analysis, which contains depth-varying Young modulus, was first examined by White in 1985 to determine residual stress distribution in moldings [94]. Two different cases were considered and it was indicated that the residual stresses in moldings with depth variation in modulus, obtained by the Treuting and Read technique, may depart significantly from the real values of residual stress. It was shown that simplifications made by Treuting and Read were no longer valid. Later, in 1989, Paterson

and White presented a new method for the analysis of residual stresses in polymer moldings with depth-varying Young's modulus [95]. Examples of applications were given by the authors. However, the same uncertainties and difficulties as mentioned for the simplified technique were still valid in terms of both mathematical derivation and experimental procedure. In another attempt, layer removal was examined for localized residual stresses in welding [96]. In this study, Cheng investigated the effect of dimensions and geometry limitations on the accuracy of this technique specifically for localized residual stress. For cold-rolled steel strip, the layer removal method along with X-ray and neutron diffraction residual stress determination techniques were employed to determine the residual stress distributions [97].

Virkar *et al.* proposed a strain gauge technique to determine residual stress distribution using the concept of layer removal [19, 98]. This technique consists of mounting a strain gauge on one surface and recording the strain generated by incrementally grinding off the opposite surface. Virkar used this technique for measurement of residual stress in oxide-ZrO2 three-layer composite. Using strain gauges in this method enhanced the deformation measurement methods, which were previously proposed and used by other researchers. However, there are some limitations and uncertainties regarding this technique. First, this method was only developed for the homogeneous materials with constant material properties and needed more extensive development in order to be employed for more generalized materials with variations in material properties. Second, the results shown in these studies were reduced to presentation of measured strain versus thickness of grinding material instead of demonstration of the through-thickness residual stress distribution. Indeed, this technique

has been used by several researchers for different materials, ceramics and polymers, to improve the residual stress measurement using the layer removal technique [98].

The layer removal method was written as a Society of Automotive Information Report in 1965 [99]. This report was used by Kim *et al.* in 1992 to offer a method of measuring the through-thickness residual stress in thermally-sprayed coatings [100]. This method then was extended by Greving et al. to a modified layer removal method for evaluating through-thickness residual stress distribution in coated materials. The modified method was verified with a three-dimensional finite element analysis and then was validated for six industrial thermal spray coatings: stainless steel, aluminum, Ni-5Al, two tungsten carbides and a ceramic thermal barrier coating [101, 102]. A modified layer removal method then was used for residual stress evaluation in composites and specifically in polymer composites by Eijpe and Powell in 1997 [18, 103]. This method was published as an ASM standard by the ASM Thermal Spray Society in 2002 [104].

2.8 Modeling and Analysis of Residual Stress in FGM

Modeling and analysis of residual stress in FGMs has been reviewed and classified by Birman and Byrd [4]. A wide spectrum of subjects from different homogenization approaches to residual stress calculation for the static and dynamic loadings to different methods of optimization and different techniques of fabrication were studied and investigated.

In functionally graded structures, material distribution can be designed to various spatial specifications. A typical FGM structure in dozens of papers is a ceramic-metal particulate composite with a gradient in the volume fraction of ceramic particles

embedded in a metallic matrix. The material property gradient is based on the compositional variation along only one direction, *z*. The following equation, used in a number of investigations as the representative function of volume fraction of ceramic in composite [4] has been considered for the compositional variation in *z* direction and used in both computational and analytical modeling.

$$V_C = \left(\frac{2z+h}{2h}\right)^N \quad for \quad \frac{-h}{2} \leq z \leq \frac{h}{2} \tag{2.1}$$

where, *h* is the thickness of the graded zone, V_C is the volume fraction of ceramic in the metal matrix, *N* is a volume fraction exponent and *z* is the direction of volume fraction variation. The volume fraction of ceramic at the interface between homogeneous and heterogeneous regions is considered as Vc_1. Te ceramic volume fraction in the heterogeneous region varies with *z*, *h* and *N*, from Vc_1 to Vc_2 at the free surface.

2.8.1 Homogenization of FGM

According to the continuous variation of volume fraction of constituents as a function of coordinate in functionally graded composites, superior performance compared to conventional composites is provided under prescribed loading conditions [105-107]. Order of the accuracy of the estimating method for the effective material properties of the functionally graded composite has a very significant role in optimizing the material performance. Because of this point of view, several averaging methods to calculate thermomechanical properties have been developed for two-phase composites. The rule of mixtures [108], the mean-field micromechanics models [109-110] and the unit cell model [111] are the most common homogenization methods for dual-phase FGMs.

A large number of studies have been accomplished in estimation of mechanical property of phase heterogeneous composites. Since currently FGMs are usually associated with particulate composites [4], the averaging approaches in the material property calculations, which are under attention in this study, are concentrated on particulate composites to use for particulate–type FGMs where the volume fraction of particles varies in one or several directions. The published papers in this area can be classified broadly into theoretical and experimental categories [112].

Theoretical methods for homogenization of FGMs are split into two possible approaches. The first approach assumes material is homogeneous in microscopic scale but heterogeneous in macroscopic scale. The second approach considers material is heterogeneous both microscopically and macroscopically. Basically these approaches are chosen based on the tense of gradient of gradation relative to the size of the considered representative volume element. In the case where the properties of material vary gradually with spatial coordinates, the first approach is considered. However, if the variations of material properties are rapid-changing functions of the coordinate, tending to the second approach is unavoidable. In this case, the RVE (microstructure) and the structure (macrostructure) are both heterogeneous.

This effect was totally neglected in one of the simplest approaches called the dilute model, while it was still considered in more advanced averaging techniques, such as the Mori–Tanaka and self-consistent methods. Among all the approximation approaches, the self-consistent models by Hill [113] and other early investigators, the mean-field micromechanics models by Mori–Tanaka [109] and Wakashima and Tsukamoto [110], the rule of mixtures and the unit cell model by Ravichandran [111] are

simple and convenient to apply for predicting the overall material properties and responses. Here, we briefly describe three methods for consideration, the linear rule of mixtures, the modified rule of mixtures by Tamura et al. [108] and the Wakashima–Tsukamoto estimate.

2.8.1.1 Linear Rule of Mixtures

A generalized law of mixtures was developed by Fan *et al.* [114] to predict the mechanical properties of two-phase composites. There is no limitation for applying this law in the case of volume fraction, grain size or phase distribution, and excellent agreement with experimental data has been shown.

A two component material has been considered by Wakashima *et al.* [115]. The effective value for a particular material property, shown by P, is estimated by three different well-known equations:

- Voigt-type:

$$P = f_A P_A + f_B P_B \tag{2.2}$$

where, P_A and P_B are the values of a particular property for pure A and pure B and f_A and f_B are their respective volume fraction. For the 100% dense material, $f_B = 1 - f_A$. For an FGM the volume fractions are functions of position along the graded region.

- Reuss –Type:

$$\frac{1}{P} = \frac{f_A}{P_A} + \frac{f_B}{P_B} \tag{2.3}$$

Both of above equations have limited validity. A more general expression is discussed:

$$P = f_A P_A + f_B P_B + f_A f_B Q_{AB} \tag{2.4}$$

where, Q_{AB} is a function that depends on P_A, P_B, f_A and f_B as well as on microstructure-dependent quantities.

Another expressions has been derived by Christensen [112] based on effective medium theory which has some analogy with the work of Fan *et al.* [114].

According to the linear rule of mixtures, the simplest estimate, any material property P(x) at a point x in dual-phase metal-ceramic materials is approximated by a linear combination of volume fractions and individual material properties of metal and ceramic constituents m and c:

$$P(x) = P_m V_m(x) + P_C(1 - V_m(x)) \tag{2.5}$$

Because this estimate can not reflect the detailed constituent geometry, the dispersion structure and so on, its accuracy is well known to be highly questionable.

2.8.1.2 Modified Rule of Mixtures

As a higher accuracy method, Tamura *et al.* [108] offered the modified rule of mixtures in which the graded region is descritized to small representative volume element sublayers, and where each is treated as a homogeneous material. In this model, uniaxial stress σ and strain ε are expressed in terms of the average stresses and strains and the volume fractions of metal and ceramic constituents:

$$\sigma = \sigma_m V_m + \sigma_c(1 - V_{m)} \tag{2.6}$$

$$\varepsilon = \varepsilon_m V_m + \varepsilon_c(1 - V_{m)} \tag{2.7}$$

Together with the introduction of the stress–strain transfer ratio defined by:

$$q = (\sigma_c - \sigma_m)/(\varepsilon_c - \varepsilon_m) \tag{2.8}$$

where $0 < q < +\infty$

The averaged Young's modulus is calculated by:

$$E = \left[\left(\frac{q + E_c}{q + E_m}\right) V_m E_m + (1 - V_m)E_c\right] \Big/ \left[\left(\frac{q + E_c}{q + E_m}\right) V_m + (1 - V_m)\right] \tag{2.9}$$

It is worth noting, while q approaches$+\infty$, the averaged Young's modulus calculated from modified rules of mixture, Eq. (2.9), is equal to the averaged Young's modulus calculated from regular rules of mixture, Eq. (2.5). However, the modified rule of mixtures is restricted to the Young's modulus, so any appropriate averaging method must be used to estimate the other thermomechanical properties. Usually, the linear rule of mixtures is being conventionally employed [105, 107 and 108].

2.8.1.3 Unit Cell Method

In this method, Chandran [111] derived a simple expression for elastic properties based on a unit cell representing the microstructure of the two-phase composite. For this purpose, parallel and series arrangements of two phases, which were respectively denoted by the iso-strain and iso-stress composite configurations, were considered. Thereby, using the basic relationships of elastic properties for both arrangements, the effective elastic

modulus of the composite was derived only from the elastic moduli of the constituents without the need for knowledge of other elastic constants. The two-phase composite in this model was assumed to be a particulate composite with the strain compatibility between the particle and the matrix. Under uniaxial loading condition, uniform strain over the entire cross section of the composite was considered. Perfect bonding between the particle and the matrix was also assumed. The interaction stresses between inclusions were ignored to the order of simplicity.

Considering all the above assumptions the elastic modulus of the two-phase composite was driven and given as:

$$E_e = \frac{(E_C E_m - E_m^2)\left(1 - V_C^{1/3} + V_C\right) + E_m^2}{E_C + (E_m - E_C)V_C^{1/3}} \tag{2.10}$$

in which the subscripts *c* and *m* refer to the ceramic and metal, respectively, and E_e is the effective modulus of elasticity of the composite. It is assumed that material properties are isotropic for each phase separately. The above equation assumes the condition of equivalence of Poisson's ratios of the matrix material and the particle phase. The shear modulus of the system can be similarly calculated. Also, the composite Poisson's ratio, based on the same system of parallel and series arrangements can be calculated [111].

2.8.2 Modeling and Analysis of Residual Stress of FGM Plates

A number of studies have been reported on modeling FGM plates in which the material properties varies through the thickness. Different analytical and computational approaches have been employed in these studies. As a powerful computational technique, FEA, has been developed and used to investigate different issues regarding functionally

graded materials. In 1993, Williamson and Rabin developed an elastic-plastic finite element model for Ni-Al_2O_3 gradient materials [116]. A comparison of predicted stresses in graded material with nongraded material was accomplished and the effects of graded thicknesses and composition profile on stress distribution were investigated. In this study an attempt was also made to optimize the design of the FGM to achieve reduction in critical stress components. The optimization was only accomplished based on specific stress components. Croce and Venini developed a finite element model of shear-deformable Reissner–Mindlin FGM plates with a power law gradient of properties in the thickness direction [117]. In another study, a three-layered plate composed of a ceramic layer, a metal layer and a FGM layer sandwiched in between, subjected to a uniform thermal loading, was considered. While plastic effects in the metal phase was taken in to account, residual stress distribution through the plate was determined [118]. The constitutive law for the metallic phase incorporated plasticity through a power law strain hardening model. The solution was validated through a comparison with the finite element results. The critical temperature corresponding to the onset of plasticity was determined as a part of the solution. The stress distribution was shown to be effectively controlled by an appropriate gradation in the FGM layer. A three-dimensional finite element analysis for FGM plates under a uniform, linear or sinusoidal thermal and pressure loading with respect to the thickness was presented by Na and Kim [119]. Another paper by Na and Kim contains a three-dimensional solid finite element analysis of a thermal buckling problem [120].

2.8.3 Modeling and Analysis of Residual Stress of FGM Cylinders

As the material properties are a function of positions and governing equations for the displacement, the residual strain and stress distributions are coordinate dependent. Numerous solutions have been developed by researchers during the last two decades [121-123]. The analytical solution for the stress distribution, in thick FGM cylinders and spheres with material properties as linear functions of radius (r), under radial thermal load was developed by Lutz and Zimmerman [124]. One-dimensional steady thermal stress in a FGM hollow sphere and cylinder under different assumptions of temperature distributions was studied using a perturbation technique by Obata and Noda [125, 126]. Tutuncu and Ozturk considered functionally graded cylindrical and spherical vessels subjected to internal pressure. The analytical solutions for the stresses, where the material properties vary from obeying a simple power law of radius, were given by theses authors [127].

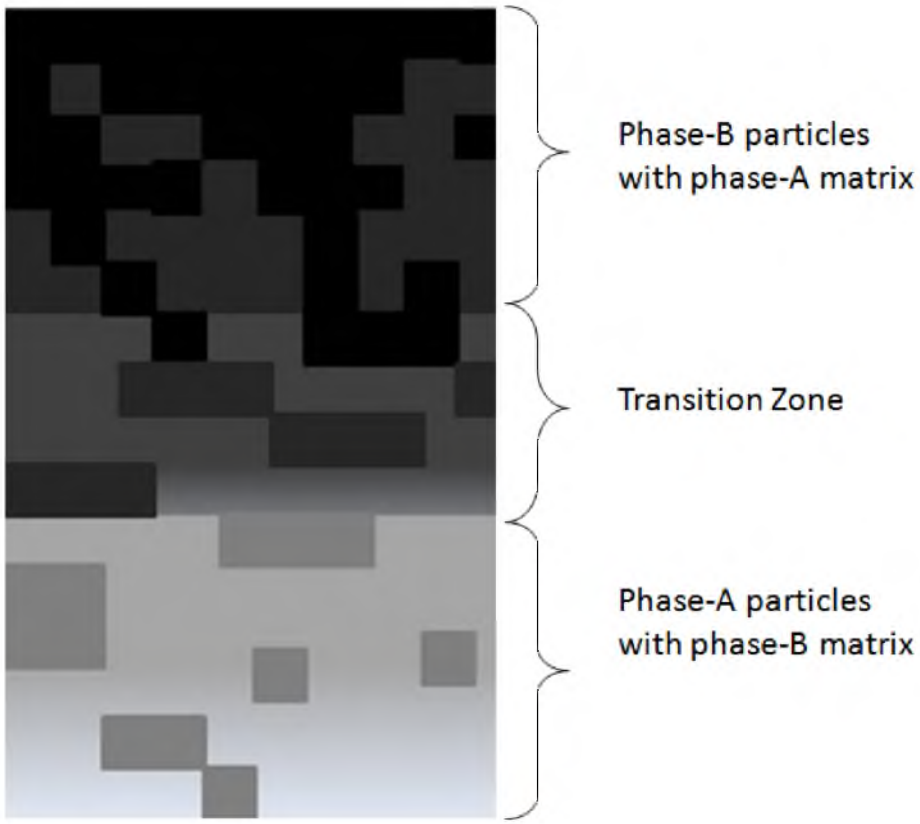

Figure 2.1. A particulate FGM with the volume fractions of constituent phases graded in one (vertical) direction. Adapted from [52].

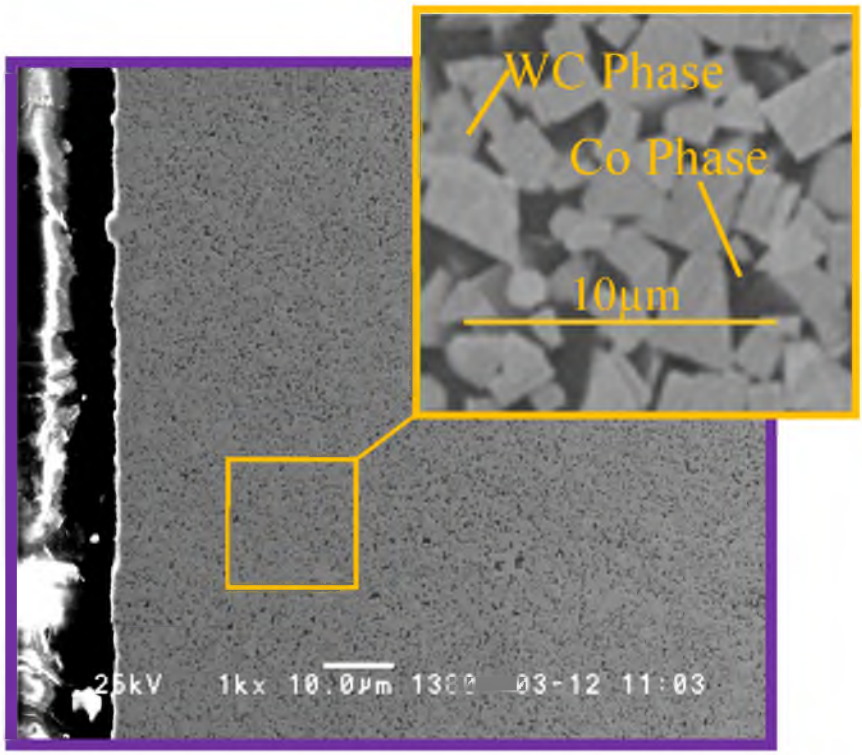

Figure 2.2. Microstructure of WC-10 wt. % Co composites. Lighter phase is WC with 5μm; grayer phase is Co binder, photo taken from polished surface with scanning electronic microscope (SEM).

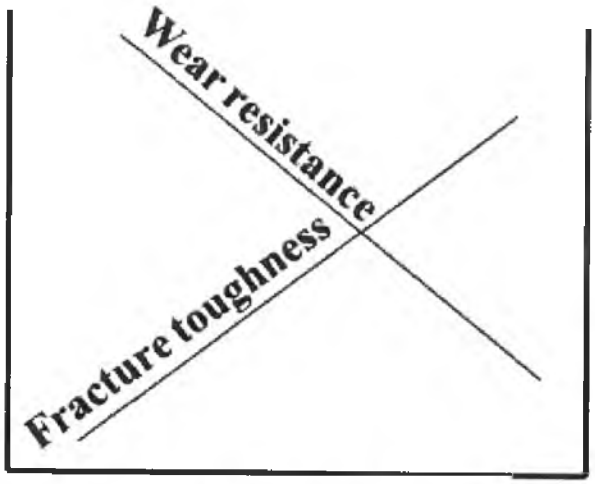

Figure 2.3. Inverse relationship between the fracture toughness and the wear resistance of WC-Co.

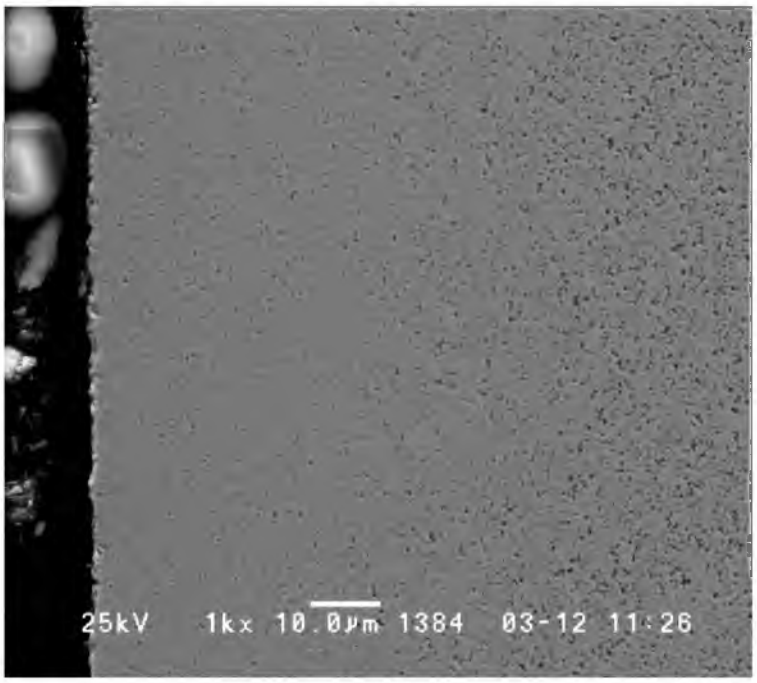

Figure 2.4. The microstructure of FG WC-10 wt. % Co.

CHAPTER 3

DETERMINTION OF RESIDUAL STRESS IN FGM PLATE

3.1 Overview

Gradual variations in composition and/or structure through the volume of functionally graded materials (FGMs) generally result in corresponding spatial variations in mechanical and physical properties, and often in significant residual stresses that are developed during processing. Due to inhomogeneous properties in these materials, residual stress measurement (determination) in FGMs can be a very challenging problem. In this section, residual stresses in functionally graded cemented tungsten carbide (FG-WC-Co) were investigated via numerical, analytical and experimental approaches by means of a layer removal technique. The numerical method consisted of finite element analysis (FEA) modeling for the FGM plate, in order to calculate residual stress distribution over the volume and to develop a method for predicting residual stress levels in closely related materials. The analytical procedure included using a proposed mathematical expression to determine residual stress distributions, and values are compared with those obtained from FEA modeling and experimental results. The experimental approach consisted of fabricating and heat treating FG-WC-Co flat samples, then measuring strain changes by strain gauge, after each sequential layer removal from the opposite side of the specimen from the graded region. Good agreement between

analytical, numerical and experimental results was achieved. At the beginning of the section, and before jumping into the layer removal technique, an existing analytical modeling of the residual stress, which is a direct mathematical solution for calculation of through-the-thickness residual stress in a FGM one-dimensional plate is described [127]. This part is then followed by an FEA modeling of the FGM one-dimensional plate; then, the results of both will be compared and discussed.

3.2 Mechanical Properties of Functionally Graded Materials

Mechanical properties like elastic modulus, coefficient of thermal expansion and Poisson's ratio are well known for homogeneous materials such as metals and ceramics. However, for FGMs, measurement of mechanical properties is a challenging subject due to the microscopic in-homogeneity, which creates location-dependent material properties. A large number of studies have been accomplished in estimation of mechanical properties of FGMs. Currently, FGMs are usually associated with particulate composites [4]. The averaging approaches in the material property calculations under consideration in this study, are concentrated on particulate composites to use for particulate–type FGMs where the volume fraction of particles varies in one or several directions. The published papers in this area can be classified broadly into theoretical and experimental categories [129]. Theoretical methods for homogenization of FGMs are split into two possible approaches. The first approach assumes material homogeneous in microscopic scale but heterogeneous in macroscopic scale. The second approach considers material heterogeneous both microscopically and macroscopically. Basically these approaches are chosen based on the tense of gradient of gradation relative to the size of the considered

representative volume element. In the case where the properties of material vary gradually with spatial coordinates, the first approach is considered. However, if the variations of material properties are rapid-changing functions of the coordinate, tending to the second approach is unavoidable. In this case, the RVE (microstructure) and the structure (macrostructure) are both heterogeneous.

The composite under study in this research, FG-WC-Co, is a cer-met composed of a ceramic, WC, and a metal, Co. In this composite, Co composition and accordingly, material properties of composite, vary gradually from surface to the depth of material. Due to this gradual variation, the first approach, which is homogeneous microstructure and heterogeneous macrostructure is considered in this dissertation. Variation of the volume fraction may be any prescribed function of the coordinate, but the most popular functions in the articles are classified into two groups: the piecewise variation and the exponential function. The piecewise variation of volume fraction acts as multi-cer-met layers with homogeneous material properties in each layer. From another point of view, a number of investigators considered the following equation as the representative function of volume fraction of ceramic with respect to thickness coordinate:

$$V_{WC} = \left(\frac{2z+h}{2h}\right)^{N} \quad for \quad \frac{-h}{2} \leq z \leq \frac{h}{2} \tag{3.1}$$

where V_{WC} is the volume fraction of WC in the Co matrix, h is the thickness of the gradient region, N is a volume fraction exponent and z is the direction of volume fraction variation.

According to the continuous variation of volume fraction of constituents as a function of coordinate in functionally graded composites, the mechanical and physical

properties of the functionally graded material changes by location. To estimate the effective material properties in FGM, several homogenization methods are developed for particulate composites [130]. Among all averaging methods, the rules of mixture [131], the mean-field micromechanics models [132, 133] and the unit cell model [111] are the most common homogenization methods for dual-phase FGMs. Based on what Ravichandran showed [127], the unit cell model is an appropriate homogenization model for functionally graded cemented tungsten carbide. Accordingly, the elastic modulus of two-phase composites varies with volume fraction as:

$$E(z) = \frac{(E_{WC}E_{Co} - E_{Co}^2)\left(1 - V_{WC}^{1/3} + V_{WC}\right) + E_{Co}^2}{E_{WC} + (E_{Co} - E_{WC})V_{WC}^{1/3}} \tag{3.2}$$

in which the subscripts *WC* and *Co* refer to the ceramic (WC) and metal (Co) and *E(z)* is the modulus of elasticity of the composite with respect to graded direction which is the *z* direction. Coefficient of thermal expansion is the other affected property of material by the variation of volume fraction in *z* direction. The thermal expansion coefficient (α) of the composite is considered variable as [127]:

$$\alpha(z) = \alpha_{Co}(1 - V_{WC}) + \alpha_{WC}V_{WC} \tag{3.3}$$

Equation (3.3) is reasonable to use only when the difference of coefficient of thermal expansion between the constituents is less than $10 \times 10^{-6}\ K^{-1}$ and not very large.

A similar equation is used for Poisson ratio:

$$\nu(z) = \nu_{Co}(1 - V_{WC}) + \nu_{WC}V_{WC} \tag{3.4}$$

in which $\nu(z)$ is the Poisson ratio of the composite.

Table 3.1 is the constant values of material properties of constituent phases used for thermal residual stress calculations.

3.3 Residual Stress in an FGM Plate: Analytical Modeling

In an FGM plate the material properties are varied by changing the volume fractions of the constituents. An example of such materials is a FG coating deposited on top of a homogeneous substrate [134, 135]. FG plates have been studied analytically and computationally by several authors [136–146]. Among studied analytical methods, a direct analytical solution proposed by Ravi Chandran in 1995 [127] provides a simple direct method for calculation of through-the-thickness residual stress in an FGM plate. Despite the fact that this analytical model is based on some simplifying assumptions, this method is still valid for residual stress determination of quite a wide range of FGMs. Specifically for cer-met FGMs, this method has been referred to and used in a considerable number of studies. In this section, the general principles of this technique are first briefly described and are then used for verification of the developed FEA model, which is discussed later.

An infinitely long FGM plate of thickness h and unit depth is considered, (Figure 3.1). It is assumed that the FGM consists of metal and ceramic components, with one side of the plate being fully metal while the other side is fully ceramic. In between both the surfaces, the composition of metal and ceramic is represented in terms of the volume fraction of one of the components as a function of distance in z direction. The composition in any xy plane is held constant. The function of the volume fraction is the same as what is explained in the previous section and in equation (3.1).

The gradual change in volume fraction of the components causes gradual changes in the mechanical properties through the thickness. Elastic modulus, coefficient of thermal expansion and the Poisson's ratio are considered as described in 3.2 section.

Residual stresses caused by the variation of material properties in the process of manufacturing FGM, or after any cooling or heating process, involve two principle contributions, one coming from stress equilibrium due to contraction or expansion and the other arising from moment equilibrium due to asymmetric stress distribution [147]. These two are named as $\sigma_t(z)$ and $\sigma_b(z)$ and are calculated in sequence in Christensen [127]. The total stress in the FGM plate in absence of any other constraint is given by :

$$\sigma_{res}(z) = E(z)\left[\alpha(z) - \frac{A_1}{E_1} + \frac{\left(A_2 - \frac{A_1}{E_1}E_2\right)(zE_1 - E_2)}{E_1E_3 - E_2^2}\right]\Delta T \tag{3.5}$$

in which

$$A_1 = \int_{-h/2}^{h/2} \alpha(z)E(z)dz \tag{3.5a}$$

$$A_2 = \int_{-h/2}^{h/2} \alpha(z)E(z)zdz \tag{3.5b}$$

$$E_1 = \int_{-h/2}^{h/2} E(z)dz \tag{3.5c}$$

$$E_2 = \int_{-h/2}^{h/2} E(z)zdz \tag{3.5d}$$

$$E_2 = \int_{-h/2}^{h/2} E(z) z dz \tag{3.5e}$$

3.4 Residual Stress in an FGM Plate: Finite Element Modeling

Using MACRO programming features in the FEA commercial software, ANSYS, namely APDL, an FGM plate under plane stress condition was modeled and is shown in Figure 3.2. The dimensions of the plate should satisfy the conditions and the assumptions considered in the analytical section. To satisfy the plane stress condition, the ratio of the length and width of the plate should be large enough with respect to the thickness. Under the circumstances, the stress along the thickness direction could be ignored. According to the one-dimensional gradient assumption, the material properties vary only along the thickness, the z direction. To apply this assumption into the FE modeling, the plate is discretized to a limited number of layers in which each layer has uniform material properties such as elastic modulus and coefficient of thermal expansion (homogeneous microstructure and heterogeneous macrostructure). Assuming that the material properties are isotropic and invariable with the changes of temperature and the analytical model is a perfect elastic body without plastic deformation, the distributions of residual stresses induced during uniform cooling from the sintering temperature (1300 ℃) to room temperature (25 ℃) were calculated by FE.

In this study, element PLANE82 was initially used. This element type is a higher order version of the element PLANE42. In fact, element PLANE82 is more accurate for the application of mixed (quadrilateral-triangular) automatic meshes and can tolerate irregular shapes without as much loss of accuracy. This element can be used either as a plane element (plane stress or plane strain) or an axisymmetric element. PLANE82 is

defined by eight nodes, in which two degrees of freedom at each node are considered, which are translations in the nodal *x* and *y* directions [148]. The alternative element type studied in this project was SHELL99. SHELL99 is used for layered applications of a structural shell model. SHELL99 allows up to 250 layers. The element has six degrees of freedom at each node: translations in the nodal *x*, *y*, and *z* directions and rotations about the nodal *x*, *y*, and *z*-axes.

The element is defined by eight nodes, average or corner layer thicknesses, layer material direction angles, and orthotropic material properties. While SHELL91 uses less time for elements of under three layers, SHELL99 uses less time for elements with three or more layers. It is shown in the verification section that a good agreement between results from finite element method and analytical method is achieved by using SHELL99 element in the finite element modeling.

3.4.1 Convergence and Verification of the FEA Model

In this section, an FGM strip, infinitely long in the *x* direction, with 100 mm length, *x* direction, and 10 mm height, *z* direction, is considered (Figure 3.2). The strip is fully ceramic (Al_2O_3) at the bottom line and changes to fully metal (Ni) at the top line. The material in the intermediate region consists of varying proportion of Al_2O_3 and Ni. The volume fractions of the ceramic phase varies in the *z* direction following equation (3.1). Elastic modulus, coefficient of thermal expansion and the Poisson's ratio are considered as described in section 3.2. Values of constants used in the above equations for Ni and Al_2O_3 are presented at Table 3.1. To verify the FEA model for the one-dimensional (1-D) beam problem, residual stress achieved from the FEA model is

compared to that from the analytical solution [127].

In the calculation of residual stresses, three gradient profiles, as shown in Figure3.3 were considered. These profiles were drawn based on the power equation (3.1) in which, by changing the power N, different shapes for the gradient profiles were obtained. Figure 3.3 shows three shapes for the profiles of the ceramic volume fraction through the thickness of the strip for three chosen powers as N=0.2, 1 and 5. A linear profile was achieved with N=1, however, concave and convex profiles were given with N<1 and N>1, respectively. These choices represent only a few possibilities of many that could be considered.

The elastic modulus, E, as well as the coefficient of thermal expansion, α, obeying equation (3.2) and (3.3), varied gradually with respect to z through the thickness. According to the linear relationship between α and V_C and relatively linear relationship between E and V_C, the same patent as variation of V_C through the thickness for E is expected, as illustrated in Figure 3.4.

As the next step, the convergence of the FEA model is studied through (i) mesh refinement, and (ii) layer refinement for N=0.2. Figures 3.5 through 3.7 show the convergence trend of the FEA model. As illustrated , while N is equal to 0.2 and for 10 descretized layers, residual stress distribution is not smooth, which represents that the model is not converged enough. By increasing the number of layers to 40, the model is converged well along the thickness of the plate except at the edges of the model, where residual stress graph is a still a little bit nonsmooth. Further increasing of the number of layers to 80 even eliminates the nonsmooth edges of the residual stress distribution. Therefore, it is well shown that the model is pretty well converged at 80 layers. However,

since the difference between the 40 layers and 80 layers is not considerable, it is allowable to use 40 layers in case of memory limitation or number of nodes restrictions in ANSYS.

The final step is to show the agreement between the FEA model and the analytical model. Figure 3.8 shows the verification of the FEA model by excellent agreement with the analytical solution of Ravichandaran [127], corresponding temperature dependent and temperature independent mechanical properties of the material of interest, in which N varies between 0, 2 and 5.

3.5 Finite Element Modeling of Residual Stress in FG-WC-Co Plate

A thin FG-WC-Co plate was modeled using APDL in the commercial software, ANSYS. The plate was composed of a homogeneous substrate and a heterogeneous (FGM) region with a one-dimensional gradient of material properties through the thickness, the z direction. The plate was segmented into very thin layers in the FG region (Figure 3.9), in which each layer was considered to have a uniform composition and, accordingly, identical elastic modulus and thermal expansion coefficient. Due to the symmetry of the problem, only one-quarter of the real sample was modeled. Figure 3.9 is the representation of the mesh structure, in which different colors represent differences in the material properties.

In this meshed model, the material property gradient was based on the compositional variation along the z direction. The following equation was employed as the representative function of volume fraction of ceramic in the graded region [4]. This

equation was used to determine the compositional variation in the z direction, which was taken as an input for FEA modeling.

$$V_C(z) = (V_{C1} - V_{C2})\left(\frac{h-2z}{h}\right)^N + V_{C2} \qquad for \ -h/2 \leq r \leq h/2 \qquad (3.6)$$

where, h is the thickness of the graded zone, V_C is the volume fraction of ceramic in the metal matrix, N is a volume fraction exponent and z is the direction of volume fraction variation. The volume fraction of ceramic at the interface between homogeneous and heterogeneous regions was considered as V_{C1}. The ceramic volume fraction in the heterogeneous region varies with z, h and N, from V_{C1} to V_{C2} at the free surface. The volume fraction of ceramic at each discrete layer, through the thickness of the FGM region, was calculated and different gradient profiles plotted for the selected N values.

Having V_C values for each discrete layer in the FGM region, the effective elastic modulus of the layer was calculated by the unit cell method using equation (3.2) [127]. The coefficient of thermal expansion (CTE) of WC-Co in the FGM region was determined using equation (3.3). In FEA modeling, it was assumed that material properties were isotropic in each meshed layer.

Uniform thermal loading from the sintering temperature to room temperature, during furnace cooling of the samples, was considered and the model assumed a perfect elastic body during the cooling cycle. Once the model was entirely established by its geometry, material properties, boundary conditions and thermal loading, the static solution was utilized and the residual stress distribution throughout the thickness of the FGM was calculated. The designed FEA model was compared to the one-dimensional case using the analytical method previously presented in 3.3 of the current study. The

verification procedure of the analytical method was given in 3.4.1.

In the FEA model, a WC-16 wt. % Co block with a graded region from the surface to the depth *h,* is considered. Thus, the block consists of a homogenous substrate and a FG-WC-Co region. The Co content in the homogeneous substrate is maintained at 16 wt. % from $z=-(h_1+h/2)$to $z=-h/2$ and varies gradually as expressed in equation (3.6) from $z=-h/2$ to $z=+h/2$ and from 16 wt. % Co to 10 wt. % Co. In the homogeneous region, the material properties, i.e., elastic modulus and thermal expansion coefficient values for WC-16%Co are equal to $540GPa$ and $5.5\times10^{-6}/^{\circ}C$, and for the FGM region, elastic modulus and thermal expansion coefficient vary with the position obeying equation (3.2) and equation (3.3) relatively.

Figure 3.10 and Figure 3.11 show the distribution of elastic modulus, E, and coefficient of thermal expansion, α, as a function of position along the thickness of the plate. Different gradient profiles are considered in Figures 3.10 and 3.11. In equation (3.6), the gradient profile is represented by the power index, N, which directly appears in material properties and therefore in residual stress and strain distributions. N can be selected from a wide range of possibilities, however, the range of N values selected in this study are as 0.1, 0.2, 0.5, 0.8, 1, 2, 5 and 10. The values of E and α are normalized based on their values in the homogenous region. For the values such as N<0.5, the variation of material properties is sharper closer to the surface and then smoothly converts to the values in the homogeneous region at the interface. These gradient schemes are relatively closer to those obtained from the experimentally fabricated samples. However, other values are also considered to gain the optimum N value that can exist by studying gradient profile effects on the residual stress distribution.

Figure 3.12 represents the stress distribution versus thickness of the WC-Co plate for different values of *N*. As illustrated, at the surface of the homogeneous region with WC-16 wt. % Co, the residual stress is compressive and its magnitude decreases linearly, then converts to tensile stress and gets to a maximum before reaching the intersection of homogeneous and heterogeneous regions. Additionally, the slop of the linear portion changes for different *N* values. Larger *N* results in a greater slope as well as a larger compressive intercept and higher tensile stress at the intersection of the homogeneous and heterogeneous regions. In the FG region, the residual stress follows almost the same trend as the Co profile and finally, at the surface with WC-10Co, it converts to compressive stress again except for *N*=5 and 10.

Figure 3.12 shows that the highest compressive stress belongs to *N*=0.5, 0.8 and 1 whereas it gets to zero for *N*=5 and to a small tensile stress for *N*=10. Higher compressive stress at the surface is desirable since a negative value of stress can improve the cutting tool lifetime and performance. Another effective value of stress distribution on the lifetime of a tool is the magnitude of stress at the interface of the homogeneous and graded regions, which current demands call for it to be smaller. Tensile stress at the interface increases while the value of *N* increases such that almost zero stress for *N*=0.1 reaches to 100 *MPa* for *N*=10, which is a significant value of residual stress. The sharp variation of material properties at the interface for larger *N* values causes the higher tensile stress at the interface.

Figure 3.13 shows the comparison of biaxial stresses distribution, σ_{xx} and σ_{yy}, as a function of position through the thickness of the WC-Co plate. As presented, the graph of stress distribution in the *x* direction is perfectly coincided with the stress in the *y*

direction. This evidence confirms the plane stress condition, which was considered as a pre-assumption in the analytical method. Figure 3.13 also justifies the idea of measuring strain only in the *x* direction, which is accomplished in this study.

3.6 Layer Removal Technique for FGM: Theory and Analytical Development

In this section, an analytical development of layer removal technique is presented to determine the residual stress distribution in an FGM plate. As comprehensively discussed in Chapter 2, layer removal technique has been used and modified by numerous researchers to determine the residual stress for different homogeneous materials as well as coatings and multilayered composites. However, this technique has never been used for FGMs. The analytical model, which is presented in this section, has been developed by Ravi Chandran for the first time for determination of residual stress in FGM using layer removal technique. A thin flat FGM plate with one-dimensional gradient of material properties along the thickness, *z* direction, is considered, (Figure 3.14). The variation of material properties creates residual stress through the thickness of the FGM plate, which is a nonsymmetric profile. Figure 3.14(a) shows a schematic of the FGM plate, the distribution of elastic modulus and the distribution of the residual stress before grinding. Figure 3.14(b) shows how one part of stress is removed from the stress profile while one layer of material is removed by grinding.

The gradient of the material properties was assumed to be a one-dimensional profile, thus, the elastic modulus, $E(z)$, and thermal expansion coefficient, $\alpha(z)$, are only a function of the *z* coordinate. According to the plane stress condition, $\sigma_{zz} = 0$ and the

stresses in the x and y directions were considered as a function of z alone, such that $\sigma_{xx}=\sigma_{yy}=\sigma(z)$. The strains in the x and y directions are given by:

$$\varepsilon_{xx} = \varepsilon_{yy} = \varepsilon(z) = \frac{\sigma_{xx} - \nu\sigma_{yy}}{E(z)} = \frac{(1-\nu)\sigma(z)}{E(z)} \tag{3.7}$$

The layer removal technique is based on the principle of maintaining force and moment equilibrium in the initial material, before layer removal, as well as in the remaining material, after layer removal. By definition, the force balance for a steady balanced sample before material removal is given as:

$$b\int_0^d \sigma(z)dz = 0 \tag{3.8}$$

where, b is the width and d is the total thickness of sample. Since in this technique, at each step, a δ thickness of material is ground off the surface, the force balance in term of stress distribution before grinding, which is $\sigma(z)$, is no longer maintained after each time material is ground. In other words, the force equilibrium in the remaining material cannot be satisfied only by integrating the forces, which are created by $\sigma(z)$. Therefore, the integral presented in equation (3.8) will not be zero anymore over the domain of remaining material, equation (3.9).

$$b\int_0^{d-\delta} \sigma(z)dz = b\int_0^d \sigma(z)dz - b\int_{d-\delta}^d \sigma(z)dz = -b\int_{d-\delta}^d \sigma(z)dz \neq 0 \tag{3.9}$$

To re-achieve the force equilibrium in the remaining material, a balancing stress $\sigma_s(z,\delta)$, is defined and added to the original stress distribution, $\sigma(z)$, equation (3.10).

$$\sigma_s'(z,\delta) = \sigma(z) + \sigma_s(z,\delta) \tag{3.10}$$

In which, the new defined stress, $\sigma_s'(z,\delta)$, satisfies the force balance equation, equation (3.11).

$$b\int_0^{d-\delta} \sigma_s'(z,\delta)dz = 0 \tag{3.11}$$

To calculate the $\sigma_s(z,\delta)$ and accordingly the $\sigma'_s(z,\delta)$, an average value of $\sigma_s(z,\delta)$ is defined and determined as $\sigma_{s_{avg}}(z,\delta)$. This is equal to the force in the removed material divided by the attributed area in the remaining material, equation (3.12).

$$\sigma_{s_{avg}}(z,\delta) = \frac{b\int_{d-\delta}^{d}\sigma(z)dz}{b\int_0^{d-\delta}dz} = \frac{\int_{d-\delta}^{d}\sigma(z)dz}{(d-\delta)} \tag{3.12}$$

Therefore, $\sigma_s(z,\delta)$, is calculated as:

$$\sigma_s(z,\delta) = E(z)\frac{\sigma_{s_{avg}}(z,\delta)}{E_{avg}(\bar{z})} = E(z)\frac{\sigma_{s_{avg}}(z,\delta)}{1/(d-\delta)\int_0^{d-\delta}E(z)dz} \tag{3.13}$$

In the above equation, the numerator is the average of stress attributed to the removed material and the denominator is the average elastic modulus of the inhomogeneous plate. Dividing the numerator by the denominator gives the average balancing strain, assuming iso-strain condition. When the average balancing strain is multiplied by $E(z)$, the balancing uniform stress is distributed according to the local modulus, under iso-strain condition throughout the beam. Therefore, considering equation (3.9) and (3.12), equation (3.13) is rewritten as:

$$\sigma_s(z,\delta) = -E(z)b\frac{\int_0^{d-\delta}\sigma(z)dz}{\int_0^{d-\delta}E(z)dz} \tag{3.14}$$

Until this point, the force equilibrium has been re-achieved after layer removal procedure, however, the moment equilibrium has not been satisfied yet, equation (3.15).

$$M(\delta) = b\int_0^{d-\delta}\sigma'(z,\delta)zdz \neq 0 \tag{3.15}$$

Substituting equations (3.10) and (3.14) in the equation (3.15), the bending moment produced by a nonsymmetric stress profile across the thickness, can be rewritten as follows:

$$M(\delta) = b\int_0^{d-\delta}\left(\sigma(z) - E(z)\frac{\int_0^{d-\delta}\sigma(z)dz}{\int_0^{d-\delta}E(z)dz}\right)zdz \tag{3.16}$$

For moment balance, a moment of this magnitude but with the opposite sign must be created. This moment creates an additional stress term that must be added to the net stress in equation (3.10). However, this moment-induced stress distribution must be calculated for the inhomogeneous plate, in the same sense as that for the homogeneous plate. The moment and moment-induced stress relationship for an inhomogeneous plate that has an arbitrary variation of elastic modulus across the thickness has been derived and given as:

$$\sigma_b(z) = -M(\delta)E(z)\frac{z\int_0^{d-\delta}E(z)dz - \int_0^{d-\delta}E(z)zdz}{\left(\int_0^{d-\delta}E(z)dz\right)\left(\int_0^{d-\delta}E(z)z^2dz\right) - \left(\int_0^{d-\delta}E(z)zdz\right)^2} \tag{3.17.a}$$

Defining:

$$I_1 = \int_0^{d-\delta} E(z)dz \tag{3.17.b}$$

$$I_2 = \int_0^{d-\delta} E(z)zdz \tag{3.17.c}$$

$$I_3 = \int_0^{d-\delta} E(z)z^2dz \tag{3.17.d}$$

The equation (3.17.a) is rewritten as:

$$\sigma_b(z) = -M(\delta)E(z)\frac{zI_1 - I_2}{I_1I_3 - {I_2}^2} \tag{3.18}$$

The final stress distribution which satisfies both force balance and moment balance is given as:

$$\sigma(z,\delta) = \sigma(z) + \sigma_s(z,\delta) + \sigma_b(z) \tag{3.19}$$

After substituting for different terms in equation (3.20), the final stress distribution can be rewritten as:

$$\sigma(z,\delta) = \sigma(z) - E(z)\frac{\int_0^{d-\delta}\sigma(z)dz}{\int_0^{d-\delta}E(z)dz} - \left(\int_0^{d-\delta}\left(\sigma(z) - E(z)\frac{\int_0^{d-\delta}\sigma(z)dz}{\int_0^{d-\delta}E(z)dz}\right)zdz\right)\left(E(z)\frac{zI_1 - I_2}{I_1I_3 - {I_2}^2}\right) \tag{3.20a}$$

Simplifying equation (3.20.a),

$$\sigma(z,\delta) = \sigma(z) - E(z)\frac{\int_0^{d-\delta}\sigma(z)dz}{I_1} - \left(\int_0^{d-\delta}\left(\sigma(z) - E(z)\frac{\int_0^{d-\delta}\sigma(z)dz}{I_1}\right)zdz\right)\left(E(z)\frac{zI_1 - I_2}{I_1I_3 - {I_2}^2}\right) \quad (3.20b)$$

Considering $z=0$ at the surface, on which the strain gauge is mounted, the net stress will be simplified as:

$$\sigma(0,\delta) = \sigma(0) + \frac{E(0)}{I_1I_3 - {I_2}^2}\left(\int_0^{d-\delta}(I_2z - I_3)\sigma(z)dz\right) \quad (3.21)$$

where, $E(0)$ is the $E(z)$ and $\sigma(0)$ is $\sigma(z)$ at the surface, on which the strain gauge is mounted. According to equation (3.7), the corresponding strain is:

$$\varepsilon(0,\delta) = \frac{(1-\nu)\sigma(0,\delta)}{E(0)} \quad (3.22)$$

The strain detected by the strain gauge is:

$$\varepsilon_m(0,\delta) = \frac{(1-\nu)}{I_1I_3 - {I_2}^2}\left(\int_0^{d-\delta}(I_2z - I_3)\sigma(z)dz\right) \quad (3.23)$$

For a homogeneous material in which the elastic modulus is constant, the strain measured by strain gauge reduces to:

$$\varepsilon_m(0,\delta) = \frac{(1-\nu)}{E(d-\delta)^2}\left(\int_0^{d-\delta}\big(6z - 4(d-\delta)\big)\sigma(z)dz\right) \quad (3.24)$$

This is the same as the formula driven by Virkar *et al.* in 1990 [98].

Therefore, to calculate the stress distribution profile, strain for different removed material thicknesses, is measured by the strain gauge bonded to the back surface and further, stress profile, $\sigma(z)$, is calculated from the equation (3.24).

3.7 Layer Removal Technique for FGM: Finite Element Analysis

To simulate layer removal technique, FEA model from the previous accomplishment, sections 3.4 and 3.5, was used to determine the strain at the back surface of the FGM plate. Layer by layer, material was removed from the FEA model and back-face strain was determined for each layer removal step. Back-face strain was named as $\varepsilon_{FEA}(\delta)$, which represents the back-face strain after removing δ thickness of material. Layer removal, was continued until the entire elimination of the graded region. In this simulation, all the conditions and assumptions of the initial model was satisfied, at every step of the material removal. The variation of calculated strain by FEA versus removed material thickness, δ is then plotted and compared with that obtained from analytical method. Figure 3.15 is a flowchart that explains the comparison procedure of the back-face strain determined by FEA modeling of the LRT and the analytical modeling of the LRT. The results of this comparison for three different gradient profiles are shown in Figure 3.16. As it is shown, the analytical and FEA results, $\varepsilon_{FEA}(\delta)$ and $\varepsilon_{theory}(\delta)$ are in a perfect agreement, which demonstrates the verification of the analytical work led to the derivation of equation (3.23).

3.8 Layer Removal Technique for FGM: Experimental Work

3.8.1 Sample Description

Fully sintered flat samples with WC-10 wt. % Co (wt. % is excluded subsequently in sample labeling) with approximately $2\mu m$ grain size of WC, were obtained from commercial WC-Co manufacturers, were employed in this study. The specimens were subjected to a novel carburizing heat treatment technique [44, 149 and 150] to fabricate graded WC-Co. During fabrication, the thickness and compositional profile of the graded region were controlled by numerous process factors, such as the treatment temperature, partial pressure of the atmospheric gases, holding time and number of cycles [143-144]. The geometry and dimensions of the specimens prepared for this study are shown in Figures 3.17-3.19. Table 3.2 gives sample dimensions, gradient thicknesses, h, of o.8 mm, 1.2 mm and 2.2 mm, as well as a range of sample thicknesses, d.

3.8.2 Co Gradients and Hardness

In this study, three batches composed of four samples each, were heat treated to create specific gradient profiles and gradient thicknesses. Measurements of Co content and hardness in graded WC–10Co were examined as a function of depth in a polished cross-sectioned surface, perpendicular to the graded free surface of test samples. Since cobalt measurement was a destructive process requiring cross sectioning, Co profiles could not be measured directly for each individual sample and, therefore, a single representative sample was used for each group. The Co content was measured using an energy dispersive spectroscopy (EDS) technique. Each data point of the Co composition was an average value obtained by scanning a 100×1000 μm^2 rectangular area with the

longer axis of the rectangle parallel to the surface of the sample. The rectangular area for measurement was spaced at 100 μm increments in the direction perpendicular to the surface. The standard deviation of the data was approximately ±0.36. Hardness was measured by a Vickers hardness tester under a load of 1 kgf (HV1) with a dwell time of 5s.

3.8.3 Sample Preparation for Strain Measurement

Strain gauges were obtained from a commercial supplier, Vishay Micro-measurement, and these bonded resistance gauges were applied using standard techniques [17], but with modifications described herein to meet the experimental configurations for layer removal. Surfaces were cleaned by grinding with silicon carbide paper 220-400 grit, and cleaned with neutralizers and conditioners as recommended by strain gage supplier. The axial strain gauge (CEA-05-250UW-350) was bonded to the center of the non-FG surface, parallel to the longitudinal edges of the specimen, using the M-bond AE-10 adhesive as shown in Figure 3.18. A 3-wire, twisted, multistrand wire lead was then soldered to the tab of the strain gauge. All leads from all gauges had the same length and wire diameter. The soldered areas were then cleaned using the solvent cleaners by Vishay Micromeasurement. The ASTM E 1237 standard procedure was followed as closely as possible for gauge installation. Nonconductive protective coatings were then applied in two steps, as M-Coat A and 3140 RTV, in order to keep the gauges, wires, and solder joints absolutely dry, as well as to protect them from any mechanical damage during handling and grinding. A strain gauge was also applied to a homogeneous WC-10Co sample (identical microstructure substrate material) as a reference control. The control

sample was wired and handled in the same manner as FG specimens. A model P-3500 portable strain indicator by Vishay Micromeasurement manufacturer was used in the strain measurement in this study with 1 microstrain resolution.

3.8.4 Layer Removal and Strain Measurement Procedure

Layer removal experimentation involved two types of measurements: 1) strain; and 2) specimen thickness. To measure the strain, the bonded gauge on each sample was connected to the strain indicator in a half-bridge, and then the bridge was balanced (the output indication was set to zero). Initial measurements of these quantities were required before grinding to remove material. To measure the thickness of each FGM specimen, a micrometer caliper was used at the four corners of the specimen, avoiding the strain gauged region. After setting the initial strain indicator reading to zero, the specimens were inserted into the designed fixture, Figure 3.19, and the fixture was positioned on the grinding table. In the grinding process, the fixture was attached to a table which was placed beneath the grinding wheel to remove a layer of uniform thickness. Grinding subsequently removed a 25-50 μm layer of material from the FG side of the specimen. Initial experimentation indicated that removal of layers below 10 μm were beneath the detection sensitivity of the strain gauges. After removing each layer, the specimen was allowed to reach ambient thermal equilibrium, and the strain was measured. Grinding and strain measurements were iteratively repeated and recorded until the FG region was completely removed from the specimen. Once strain measurements ceased changing with layer removal, it was considered indicative that residual stresses in the remaining substrate were negligible.

Thickness and strain measurements and grinding processes were then iteratively repeated and recorded until the FG region was completely removed from the specimen. Once strain measurements ceased changing with layer removal, it was considered indicative that residual stresses in the remaining substrate were negligible, and the process was terminated.

3.9 Experimental Results and Discussions

3.9.1 Gradient Profiles: Measured Co content and Hardness

Figures 3.20-22 show the gradient profiles of Co content for samples of varying gradient thickness: 0.8 mm, 1.2 mm and 2.2 mm. Different gradient profiles and gradient thicknesses were obtained by varying process parameters that control the carburizing heat treatment method. The cobalt content increased gradually from approximately 6% at the surface to a maximum value of 10.5-11 wt. %, making a small dip below 10 wt.% and then approaching the nominal 10% Co content in the bulk. To effectively employ the Co composition profiles obtained from direct measurement into the developed FEA model, trend curves were fit to the Co profiles, using the polynomial curve fitting function for plots in Figures 3.20-22. Figure 3.20 shows the Co content profile and the hardness gradient, which illustrates the inverse relationship between Co content and hardness. The surface of the FG WC–Co samples in our study showed approximately 4 wt. % lower Co content than the homogeneous interior core of the FG WC–Co or of the as-received material; corresponding to an increase in hardness of approximately 200–300 HV1 between the surface and the interior.

Figure 3.23 shows a comparison between three different Co gradient profiles.

Comparing the three profiles, the rate of Co compositional change (i.e., the profile slope) increased as the gradient zone thickness decreased. In other words, although the minimum and maximum values of Co content in the graded region of specimens was fairly consistent for all three profiles, the thickness of the gradient zone varied. This experimental sample set was designed to investigate the relative effects of gradient thickness on the magnitude and distribution of stress and strain within the samples.

3.9.2 Comparison between Layer Removal Technique and FEA Modeling

Figures 3.24-28 present strain changes at the substrate surface (back-face) as a function of the material thickness removed from the graded surface. Each figure presents two series of back-face strain data from the WC-10Co samples with varying gradient thicknesses; one data series is experimentally measured strain using the layer removal technique, and the other is the numerically determined data using the developed FEA model. Figures 3.24-26 represent samples 1-3 from Table 3.2 with a gradient thickness of 0.8 mm, associated with the cobalt composition profile shown in Figures 3.20, but with different sample thicknesses. Although the FEA model underestimates the strain slightly compared to the experimental data near the interface of the graded region and substrate of the thinnest sample, Figure 3.24, and in a portion of the graded region in Figures 3.25, generally the FEA data are in good agreement with measured values. The thickest sample, 8.2 mm shows excellent agreement between the FEA model and experimental values.

Figure 3.27 represents samples 4-6, with a gradient thickness of 1.2 mm and a variation of Co between 6.5 wt. % and 10.8 wt. %, shown in Figure 3.21. Measured strain

values for samples 4-6 were averaged for Figure 3.27, since each sample had the same gradient thickness and sample thickness. Similarly, Figure 3.28 shows an averaged profile for samples 7-9, with a 2.2 mm gradient thickness and a Co composition ranging from 6% to a high value of 11%.

Considering Figures 3.26 to 3.28, with varying gradient thickness but the same sample thickness, the experimentally measured back-face strain curves show that the magnitude of strain change is directly related to the gradient thickness, with thicker gradient zones showing larger magnitudes of strain. As material was removed from the graded region, strain change would plateau and, eventually, as the graded region was totally removed, the grinding process was terminated. This correlation between the back-face strain and the depth of grinding in the graded region was seen in all curves obtained by either FEA modeling or experimentation, Figures 3.24 to 3.28, with all curves reaching values asymptotic to a constant strain value near the interface between the graded and homogeneous substrate regions.

In general, comparing the results from the experimental layer removal technique and the FEA modeling, good agreement was found between the two methods in terms of determination of strain changes as a function of the thickness of material removed by grinding. Although sample 1 and samples in group 3 showed a divergence of 15-20% between the magnitudes of strain determined by the two techniques in certain regions of the curves, all other samples were within a few percent, and the trends with grinding depth were quite similar. A number of factors may have influenced deviation between the results of the experimental method and FEA. Potential sources of error, or deviation between experimental and FEA values, include: lack of homogeneity of Co distribution

within the samples, nonuniformity of the size and composition of the graded region within the samples, deviation of FEA input variables (E, α and ν) from actual values in the material, and deviation from perfectly flat samples due to the grinding process.

3.9.3 Effect of Sample Thickness on the Measured Strain Changes and Residual Stress Distribution

As discussed in the introduction, residual stress distribution in FGM is affected by different geometrical parameters. One basic, and particularly relevant, parameter is the total thickness of the specimen. To study the effects of total sample thickness on residual stress distribution and on the variation of strain, analyses were undertaken by LRT experiments and by FEA modeling of samples 1-3, with constant Co gradient profiles and graded region thickness, but different sample thicknesses: d=4.67, 6.27 and 8.2 mm.

The specific values and distributions of through-thickness residual stress were calculated by FEA for samples 1-3, and are presented in Figure 3.29. As total sample thickness increased, the residual compressive stress on the FG surface of the sample, which is the sample's working surface, also increased; -205 MPa, -235 MPa and -284 MPa for thicknesses of 4.67 mm, 6.2 mm and 8.2 mm, respectively. The FEA results on compressive stress at the surface are validated by the X-ray diffraction work on a similar FG-WC-Co system, reported by Larssson and Odén [15]. Higher compressive residual stress on the working surface and lower tensile stresses on the interface of the substrate and FGM region are beneficial for the FG-WC-Co samples. Such residual stresses increase the wear resistance and postpone fracture initiation by deterring carbide pullout, thereby increasing the lifetime of the WC-Co components [24]. Work on FG-WC-Co by

Xu *et al.* on closely related materials also showed that the fatigue life of FG WC-10Co was increased compared to homogeneous WC-10Co [24], and hypothesized that residual compressive stresses at the surface may have contributed to the improved fatigue performance of the functionally graded material over conventional microstructures of tungsten carbide. Figure 3.29 presents modeled FEA residual stress distribution through the thickness of the graded samples, and shows compressive residual stress at and near the surface of samples for each thickness analyzed. Aside from supporting the observed results and hypothesis of Xu *et al.* regarding compressive stress and fatigue properties [24], this figure shows the sensitivity of residual stress to sample geometric parameters, specifically sample total thickness in this system.

Figure 3.30 shows three calculated FEA graphs of the back-face strain variations as a function of the removed material thickness for three FG WC-10Co samples with different sample thicknesses: d=4.67mm, 6.27mm and 8.2 mm. Once again, these samples had similar Co gradient profiles and gradient thicknesses, h=0.8mm. The plateau portions of these graphs represent the total back-face strain in the specimens before grinding. The curves in Figure 3.30 show that strain values were quite sensitive to the total thickness removed from the samples, and that the strain values were inversely related to the sample's thickness; changes in back-face strain increased with decreasing thickness of the samples. With decreased sample thickness, the induced deformation in the sample, which is the result of changes in the residual stress distribution after material removal, was higher and became evident as increased back-face strain in the material.

In Figure 3.31, the same inverse relation between the back-face strain variations and the total sample thickness was observed using experimental LRT data for the same three

sample thicknesses. Comparison of Figure 3.30 and Figure 3.31 shows that the LRT method was again in very good agreement with the FEA method.

3.9.4 Effect of Gradient Thickness on the Measured Strain Changes and Residual Stress Distribution

Another major parameter in the design of FG components is the gradient thickness. To study the effect of gradient thickness on the residual stress distribution, and therefore on the variance of strain, samples 3, 6 and 8 with similar sample thicknesses but different gradient profiles and thicknesses were considered. The specific values and distributions of the through-thickness residual stress for samples 3, 6 and 8 were determined by FEA modeling. Figure 3.32 shows the stress distribution for these samples, which possessed a sample thickness of 8.2 mm, but different gradient Co profiles and gradient thicknesses, h=0.8mm, 1.2 mm and 2.2 mm.

Figure 3.32 shows that by increasing the gradient thickness of the samples (with the same sample thickness), compressive stress on the FG surface of the sample, which is the sample's working surface, is decreased. This would indicate probable degradation of wear performance for components with thicker gradients, compared to thinner graded regions. However, since during service applications sample wear gradually reduces the gradient thickness, the samples with higher gradient thickness may actually exhibit a longer performance life due to the larger volume of material with reduced Co content.

Reciprocally, thinner graded regions with higher compressive residual stress might resist wear initially, but would have less of a gradient thickness available to withstand wear processes. Thus, a balance between the advantages of both thinner and

thicker graded regions would likely yield the strongest wear performance. A decisive optimization of the gradient thickness should be achieved by further in service experimental tests on samples with different gradient profiles and thicknesses for a specific applications with given conditions.

Figure 3.33 shows curves of the calculated FEA back-face strain variations as a function of the removed material thickness for three FG WC-10 wt. % Co samples with constant sample thicknesses, d=8.2 mm and different gradient profiles and gradient thicknesses. It was observed that the samples were sensitive to the gradient profile and thickness and that the strain values were inversely related to gradient thickness; back-face strain increased while the gradient thickness of the sample decreased. In this case, a greater portion of the sample was occupied by the graded Co composition and, thus, the thickness of the homogeneous substrate was smaller. The entire sample was affected more significantly by the residual stress magnitude and distribution with a larger gradient thickness, which resulted in a higher-value back-face stress and a greater back-face strain.

In Figure 3.34, the same relation between the back-face strain variation and gradient thickness for the three samples is also presented, as measured by the layer removal experiments. The two methods again show similar trends and magnitudes.

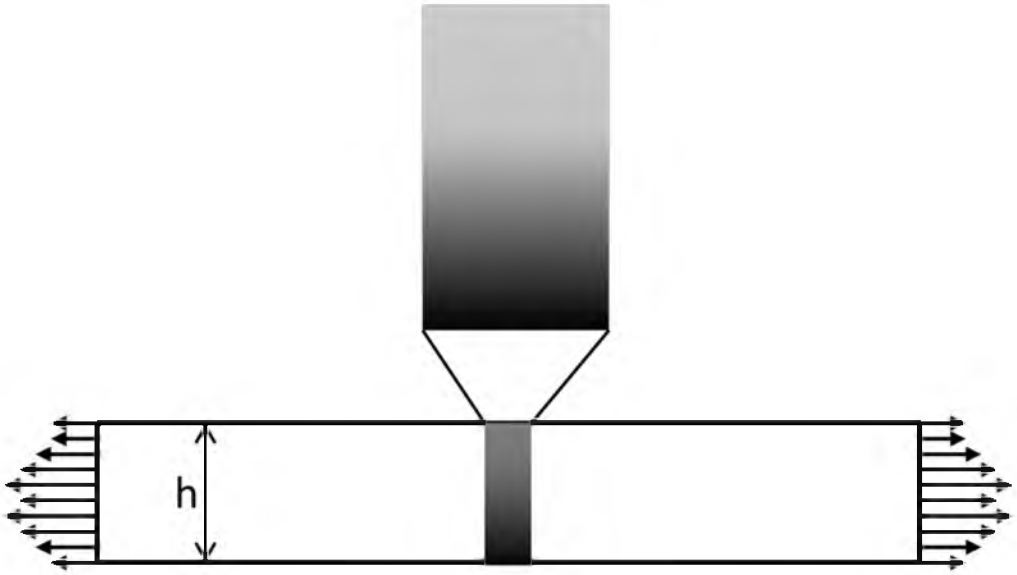

Figure 3.1 A schematic of the FGM system.

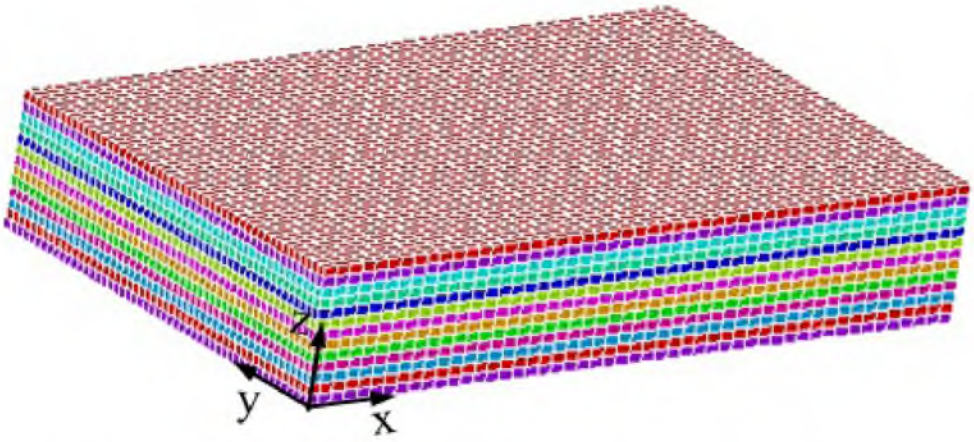

Figure 3.2 Three-dimensional FEA model of FGM plate.

Table 3.1 Material properties and constant values of Ni and Al_2O_3. Adapted from [127].

Consrtant	Al_2O_3	Ni
α (T independent)	8×10^{-6}	17×10^{-6}
$\mu_{0\ (MPa)}$	1.55×10^{5}	0.789×10^{5}
$T_{m\ (K)}$	2320	1726
$d\mu/dT$	-0.35	-0.64
ν	0.22	0.3

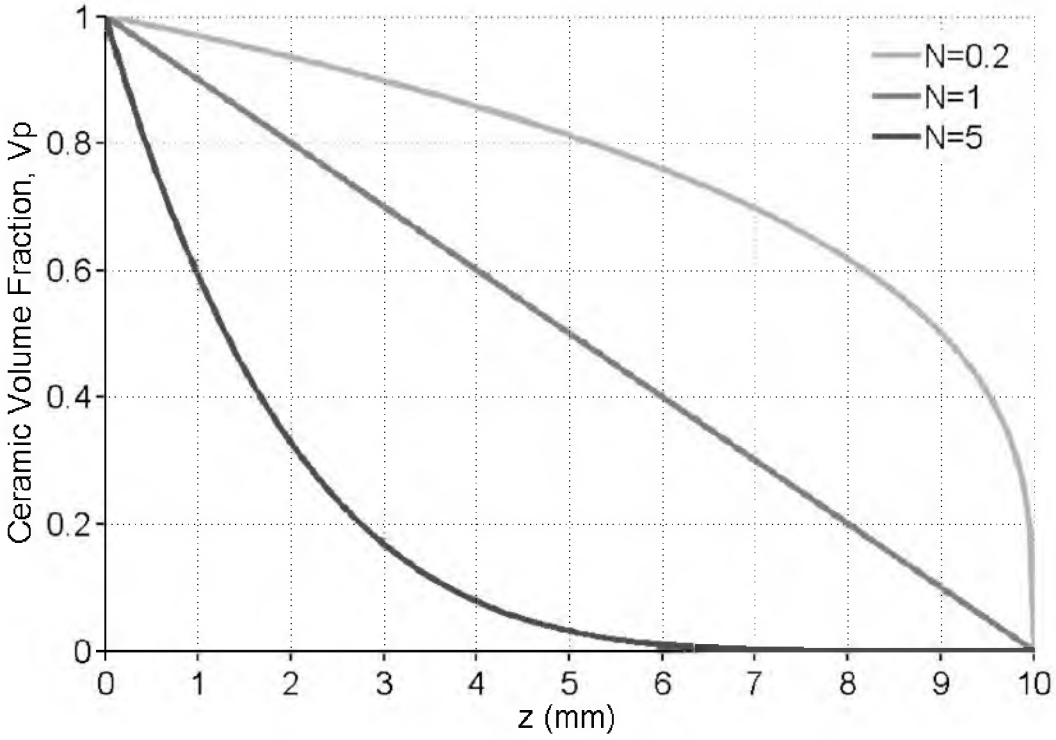

Figure 3.3 Three types of variation in the ceramic volume fraction.

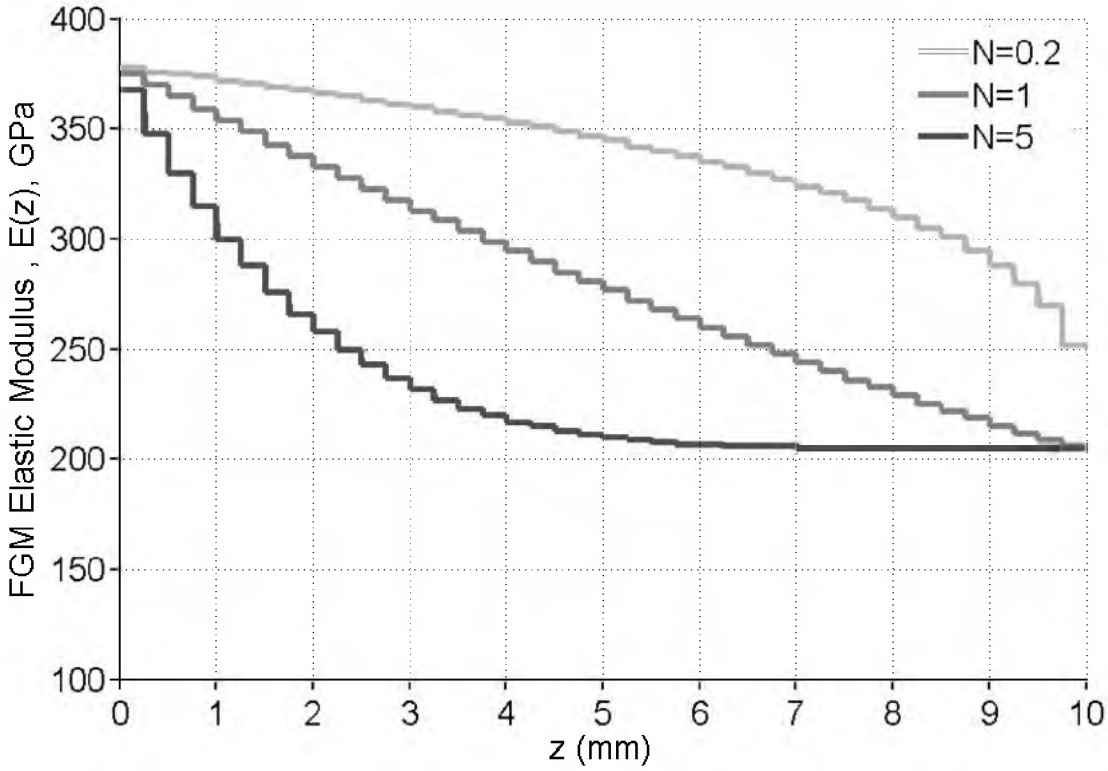

Figure 3.4 Variations of FGM elastic modulus, *E(z)*, through thickness.

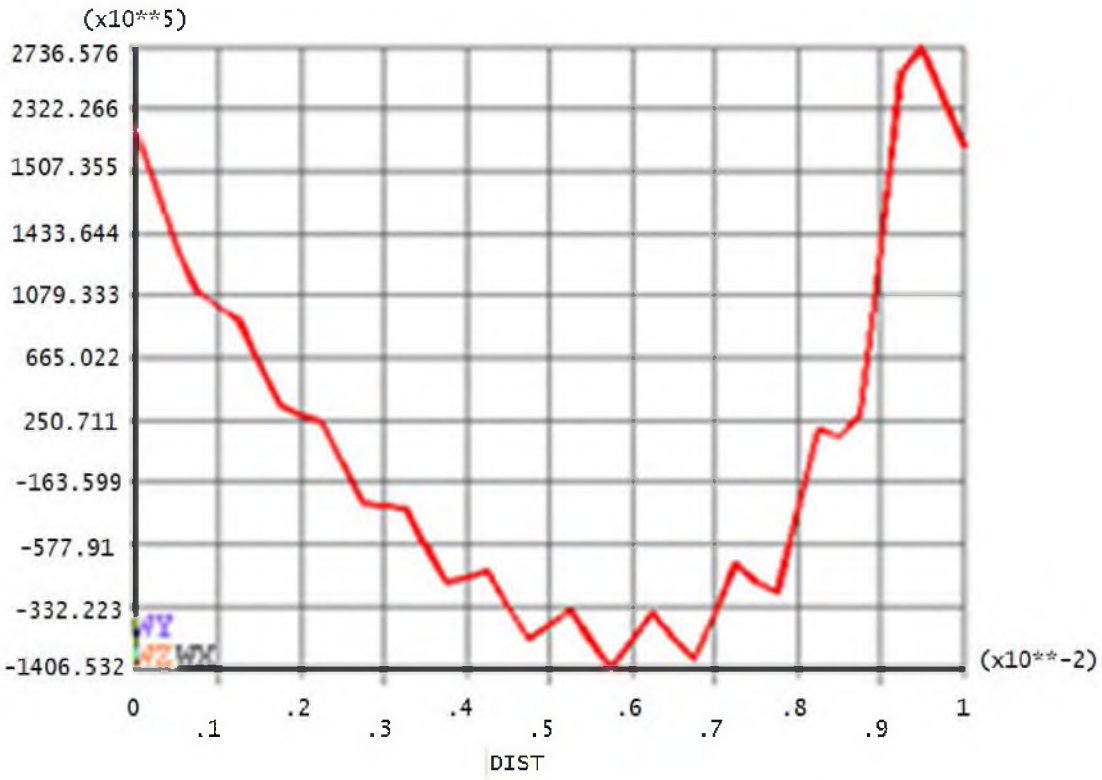

Figure 3.5 Residual stress using FEA modeling corresponding to N=0.2 and number of layers=10.

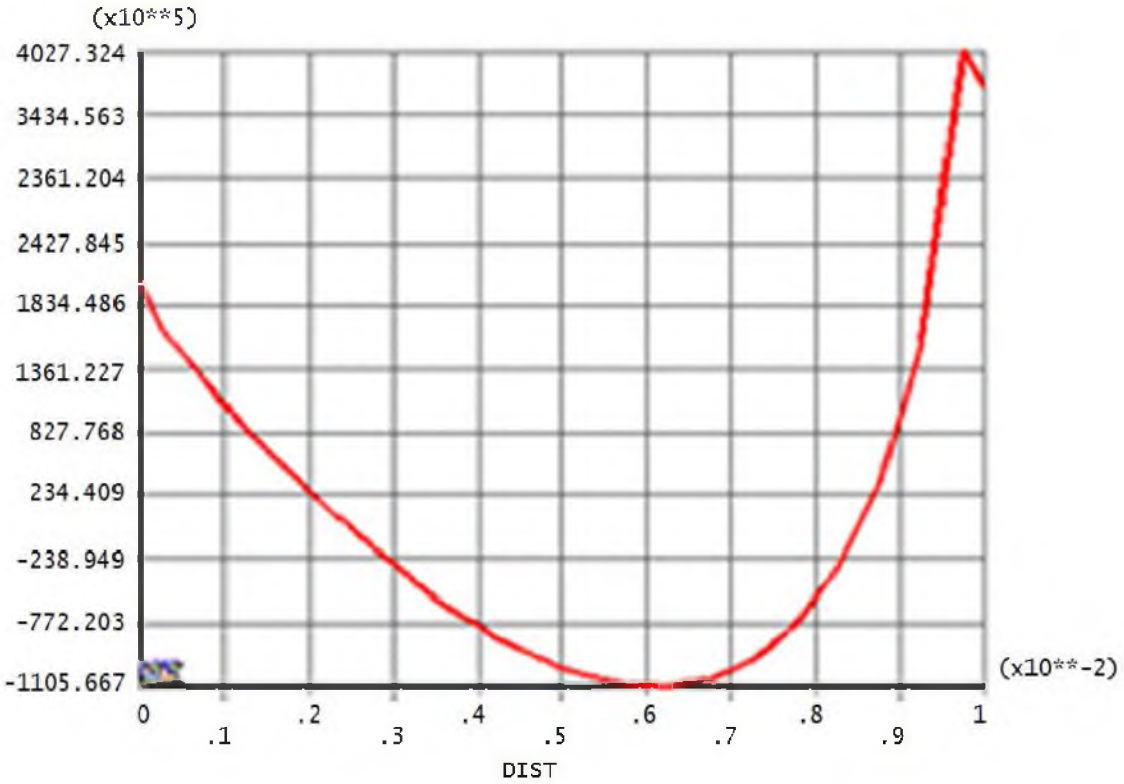

Figure 3.6 Residual stress using FEA modeling corresponding to N=0.2 and number of layers=50.

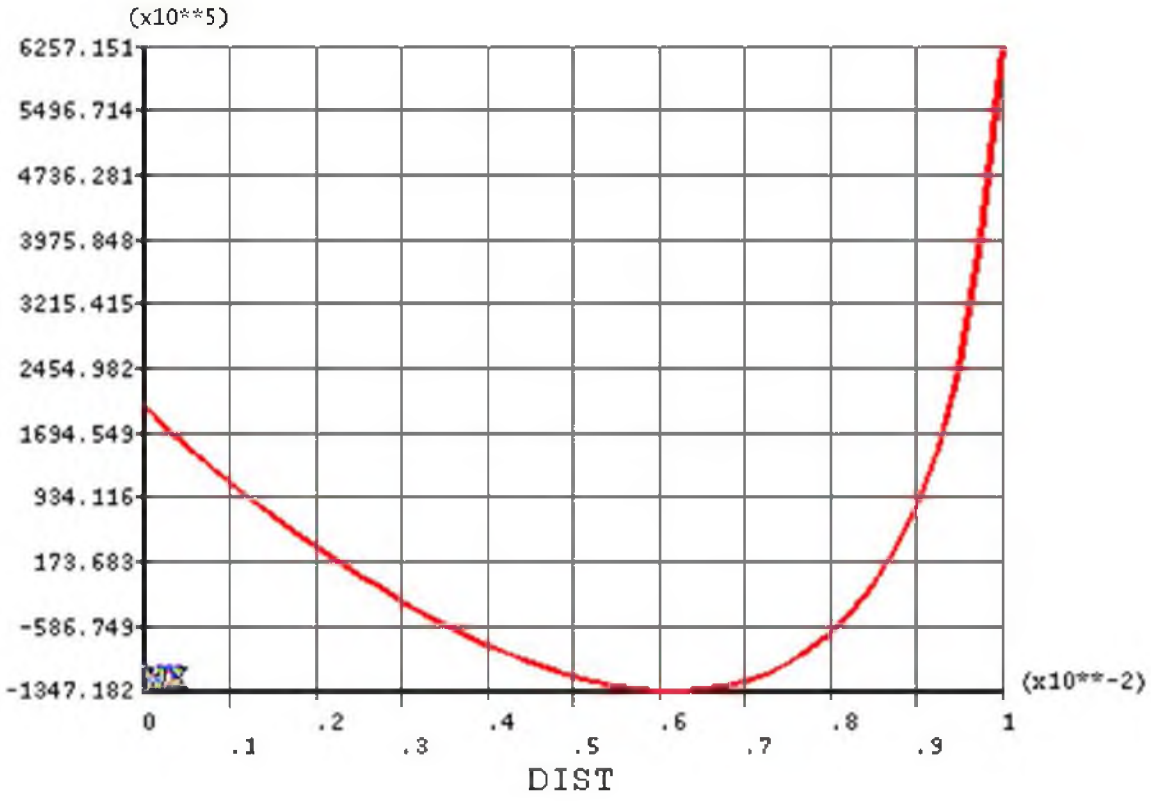

Figure 3.7 Residual stress using FEA modeling corresponding N=0.2 and number of layers=80.

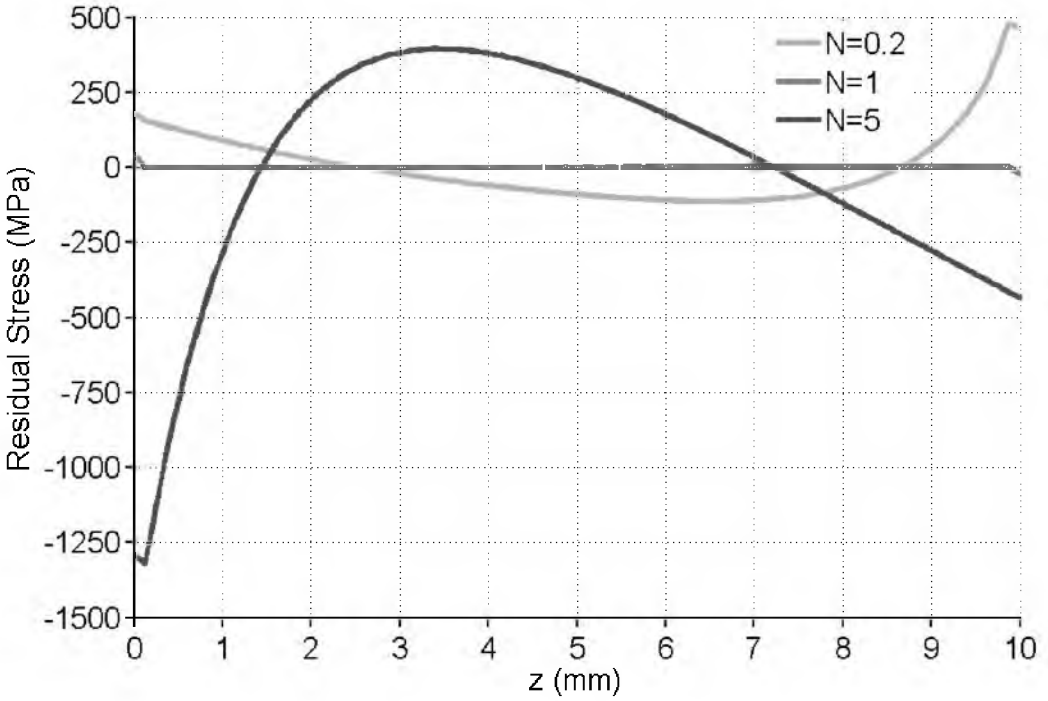

Figure 3.8 Residual stress distributions from FEA modeling for three different profiles, *N* values, 0.2, 1 and 5.

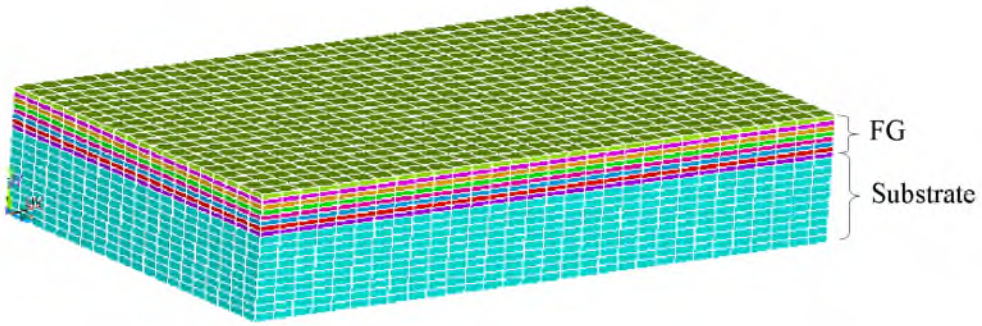

Figure 3.9 Three-dimensional FEA model showing discretization of FGM region.

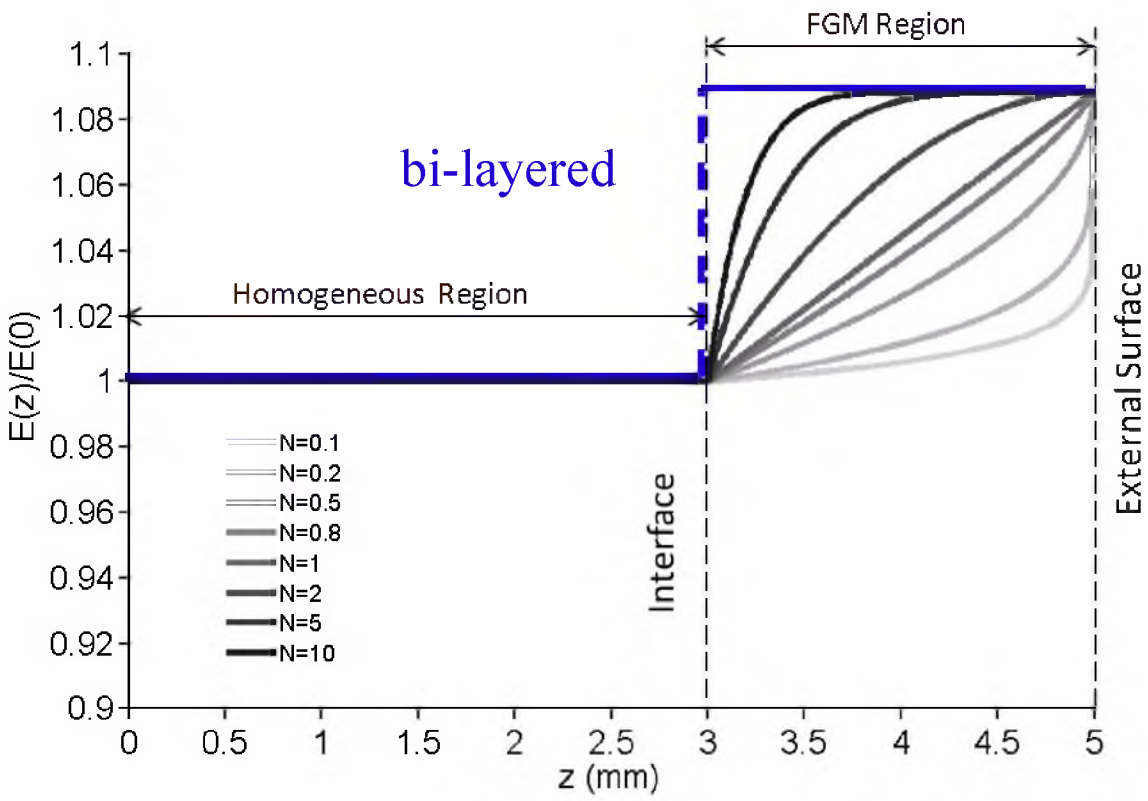

Figure 3.10 Distribution of elastic modulus in WC-Co plate for different gradient profile represented by power index, N, where the homogeneous region consists of WC-16Co with thickness of $h_1=3$ *mm*, and gradient region composed of WC-10Co with thickness of $h=2$ *mm*. $E_{homo.}=540$ *GPa*, $\alpha_{homo.}=5.86x10\text{-}6\ /^{o}C$ and $E_{Surf.}=590$ *GPa*, $\alpha_{Surf.}=5.5x10\text{-}6/^{o}C$.

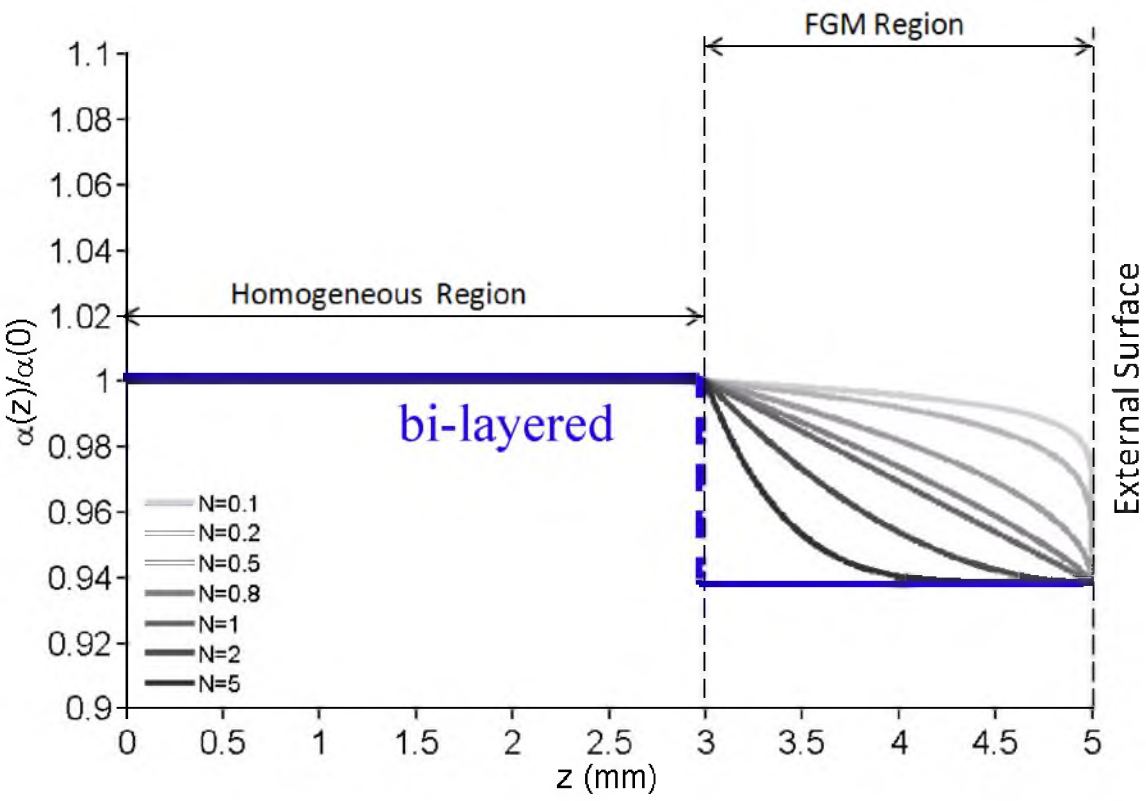

Figure 3.11 Distribution of coefficient of thermal expansion in WC-Co plate for different gradient profiles represented by power index, N, where the homogeneous region consists of WC-16Co with thickness of h_1=3 mm, and gradient region composed of WC-10Co with thickness of h=2 mm. $E_{homo.}$=540 GPa, $\alpha_{homo.}$=5.86x10-6 /°C and $E_{Surf.}$=590 GPa, $\alpha_{Surf.}$=5.5x10-6/°C.

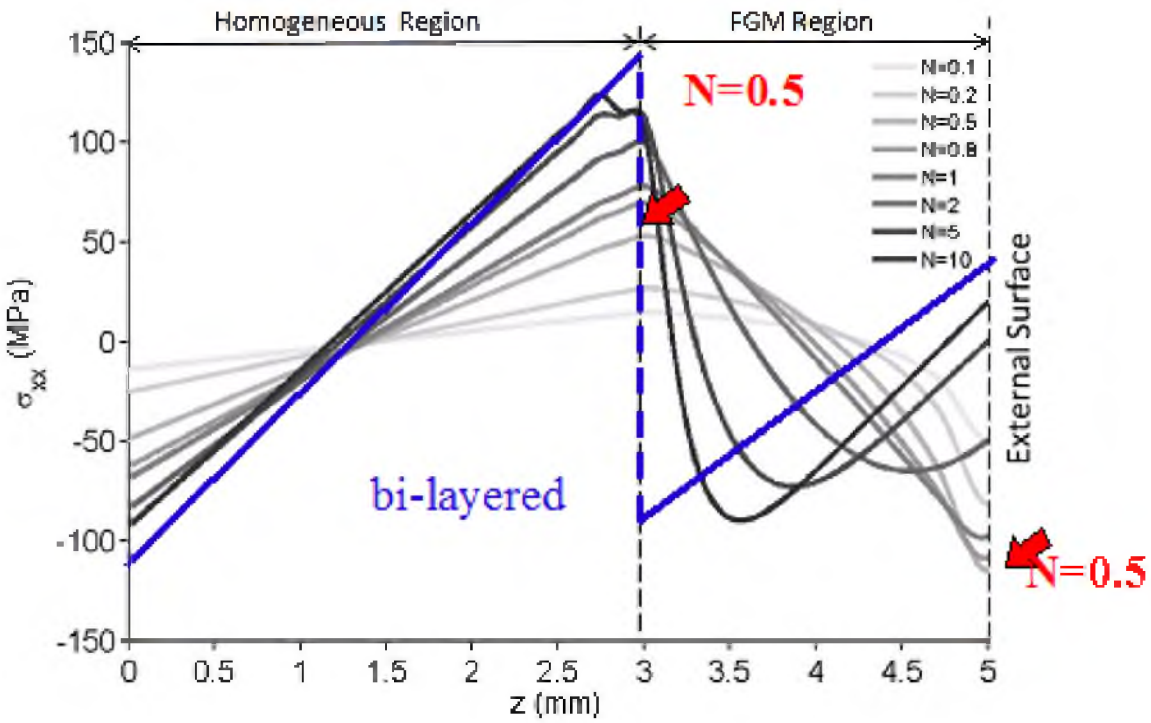

Figure 3.12 Distribution of residual stress in the *x* direction in WC-Co plate for different gradient profile represented by power index, *N*, where the homogeneous region consists of WC-16Co with thickness of h_1=*3 mm*, and gradient region composed of WC-10Co with thickness of *h=2 mm*. $E_{homo.}$=*540 GPa*, $\alpha_{homo.}$=*5.86x10-6 /°C* and $E_{Surf.}$=*590 GPa*, $\alpha_{Surf.}$=*5.5x10-6/°C*.

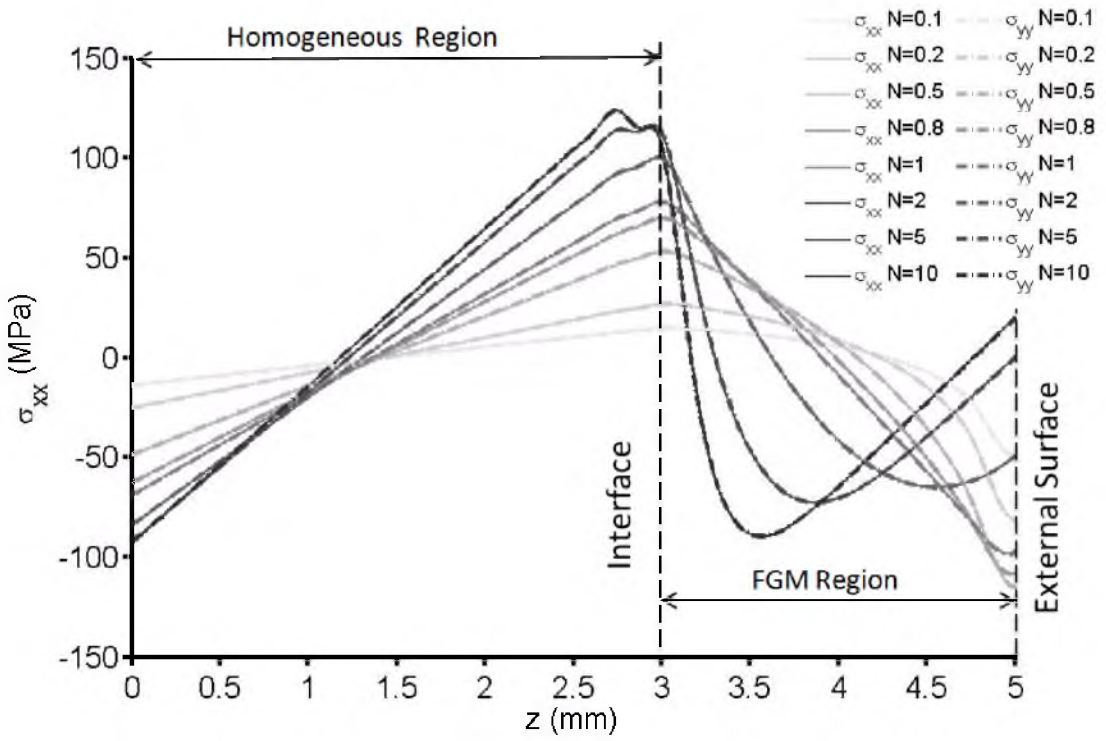

Figure 3.13 Comparison of residual stress distribution in the *x* direction as well as the *y* direction in WC-Co plate for different gradient profiles represented by power index, *N*, where the homogeneous region consists of WC-16 wt. % Co with thickness of h_1=*3 mm*, and gradient region composed of WC-10 wt. % Co with thickness of *h=2 mm*. $E_{homo.}$=*540 GPa*, $\alpha_{homo.}$=*5.86x10-6 /°C* and $E_{Surf.}$=*590 GPa*, $\alpha_{Surf.}$=*5.5x10-6 /°C*.

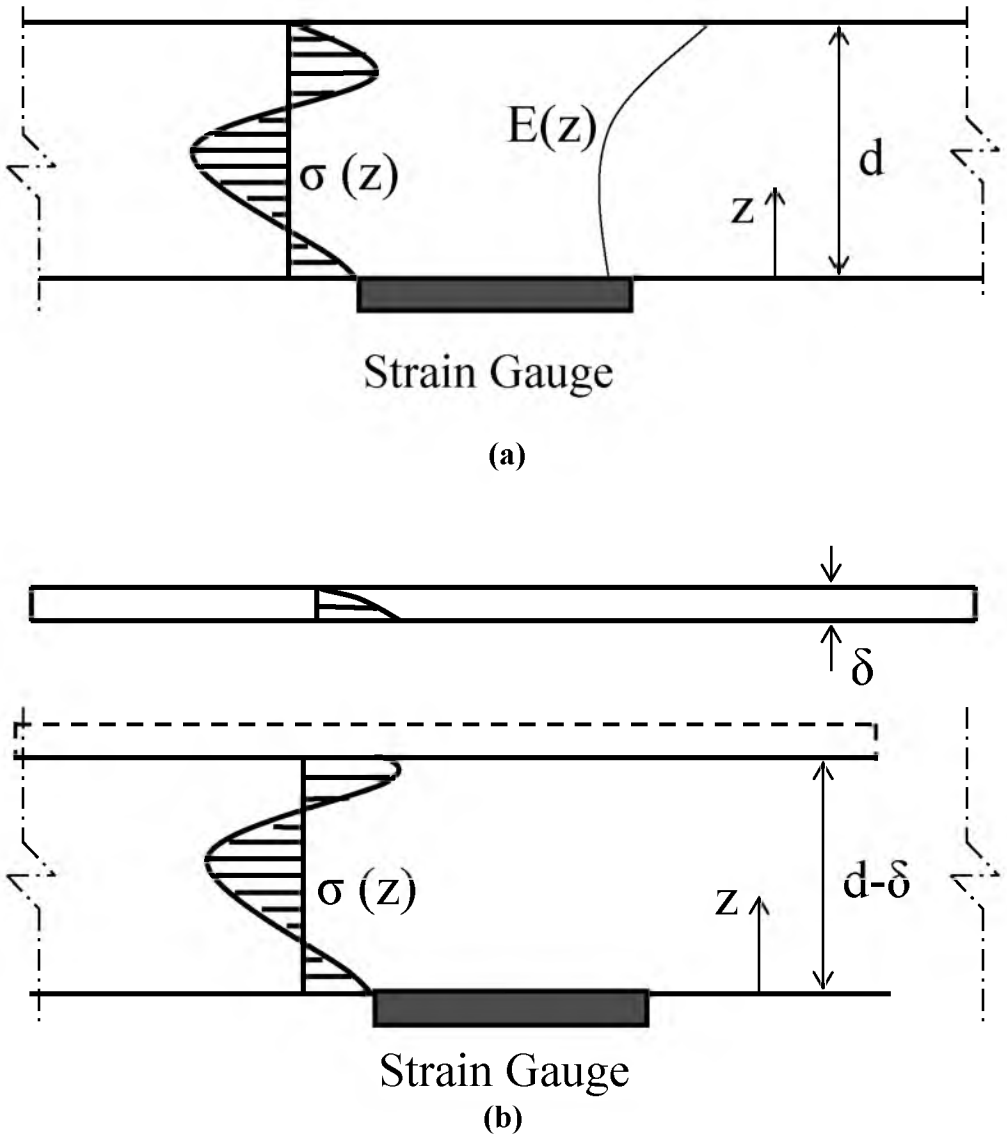

Figure 3.14 The schematic display and geometry of the FGM plate before grinding, (a), and after grinding a layer of thickness δ, (b). Through-the-thickness stress distribution, $\sigma(z)$, and the elastic modulus distribution, $E(z)$, are shown in (a) and the changes in stress distribution is shown in (b).

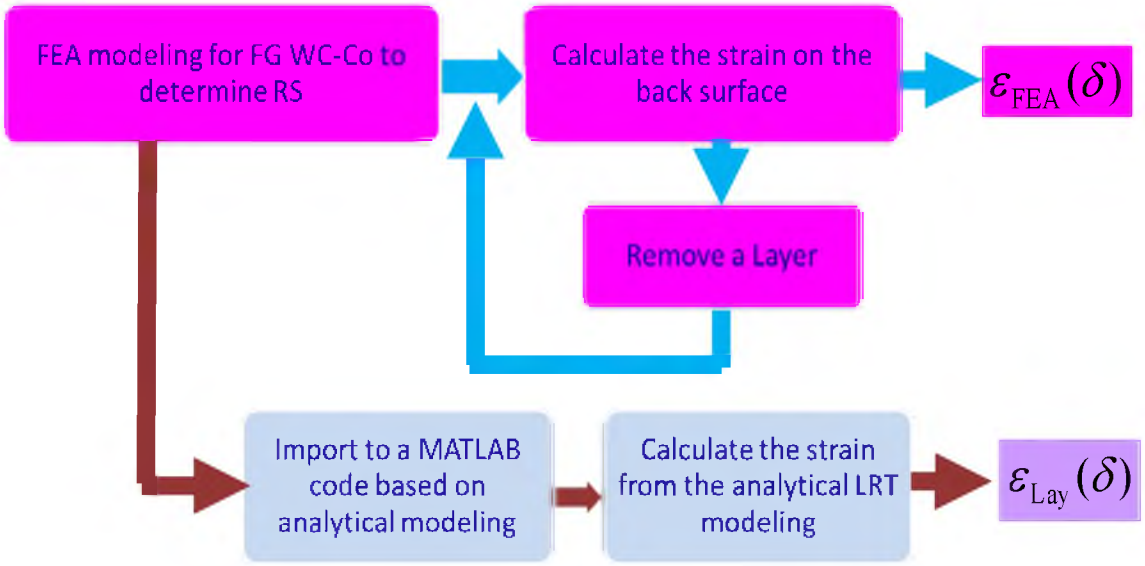

Figure 3.15 Flowchart of the comparison procedure of back-face strains, $\varepsilon_{FEA}(\delta)$ and $\varepsilon_{Lay}(\delta)$, which were calculated using FEA modeling of LRT and the analytical modeling of LRT.

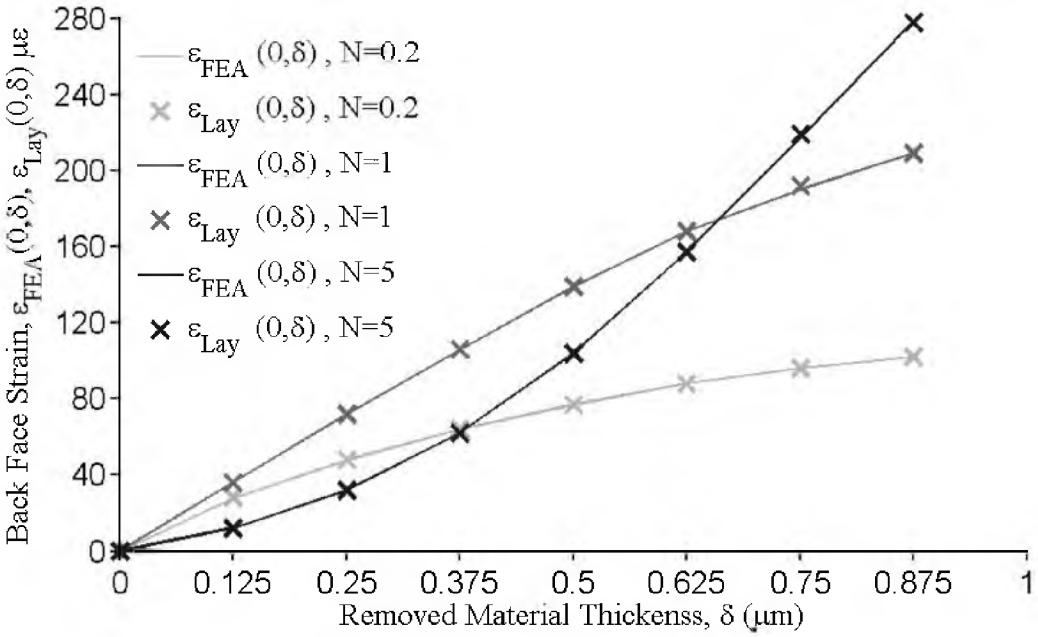

Figure 3.16 Calculated strain versus removed layer thickness, $\boldsymbol{\delta}$, from FEA modeling and mathematical expression for the three different N values.

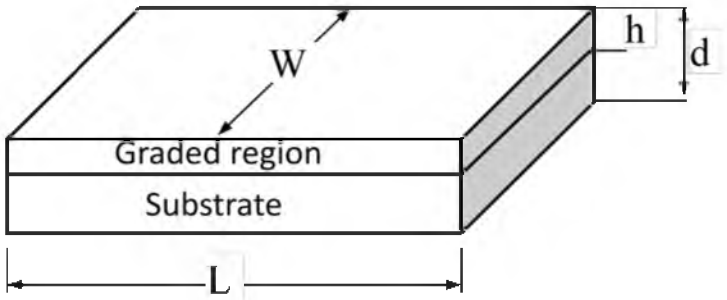

Figure 3.17 Geometry and dimensions of WC-Co specimens.

Table 3.2, Dimensions and gradient thicknesses of WC-Co specimens.

Label	Initial Cobalt wt. %	L mm	W mm	dmm	h mm
Sample 1	10	30.90	18.25	4.67	0.8
Sample 2	10	29.70	18.20	6.24	0.8
Sample 3	10	32.60	18.32	8.20	0.8
Sample 4	10	32.60	18.52	8.25	1.2
Sample 5	10	32.64	18.68	8.20	1.2
Sample 6	10	32.77	18.61	8.20	1.2
Sample 7	10	32.68	18.64	8.16	2.2
Sample 8	10	32.65	18.65	8.23	2.2
Sample 9	10	32.71	18.65	8.11	2.2

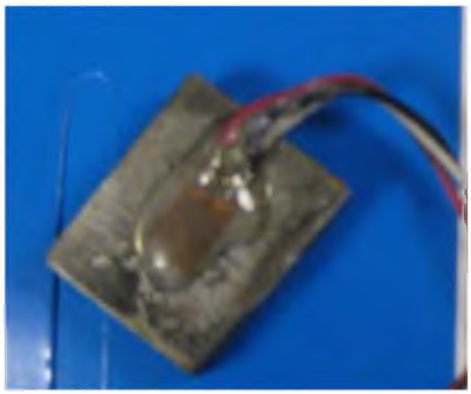

Figure 3.18 Strain gauge bonded to the specimen.

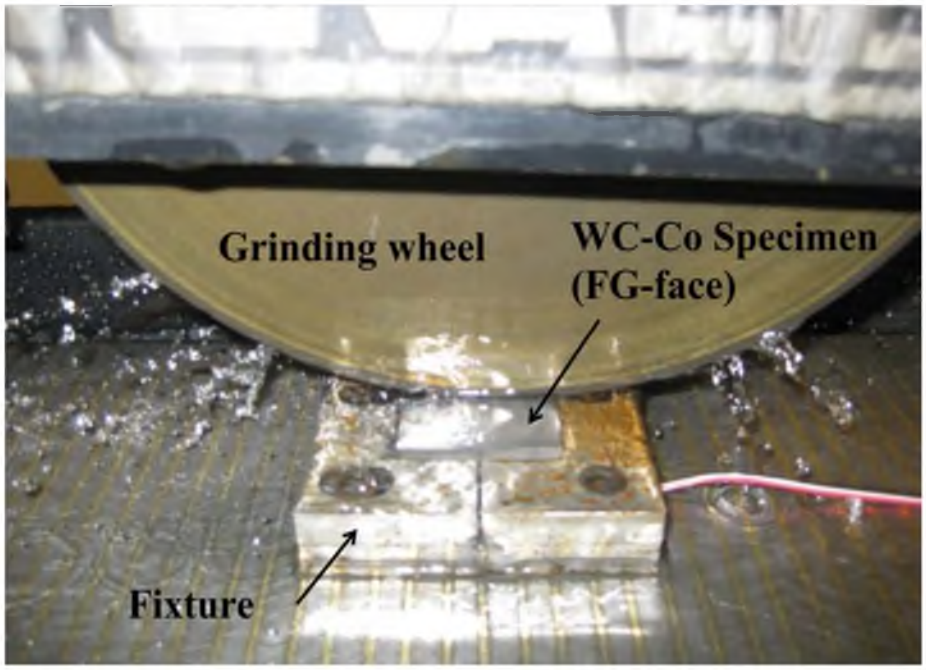

Figure 3.19 Photograph of experimental setup for layer removal, showing strain gauged sample in fixture for the flat WC-Co specimens.

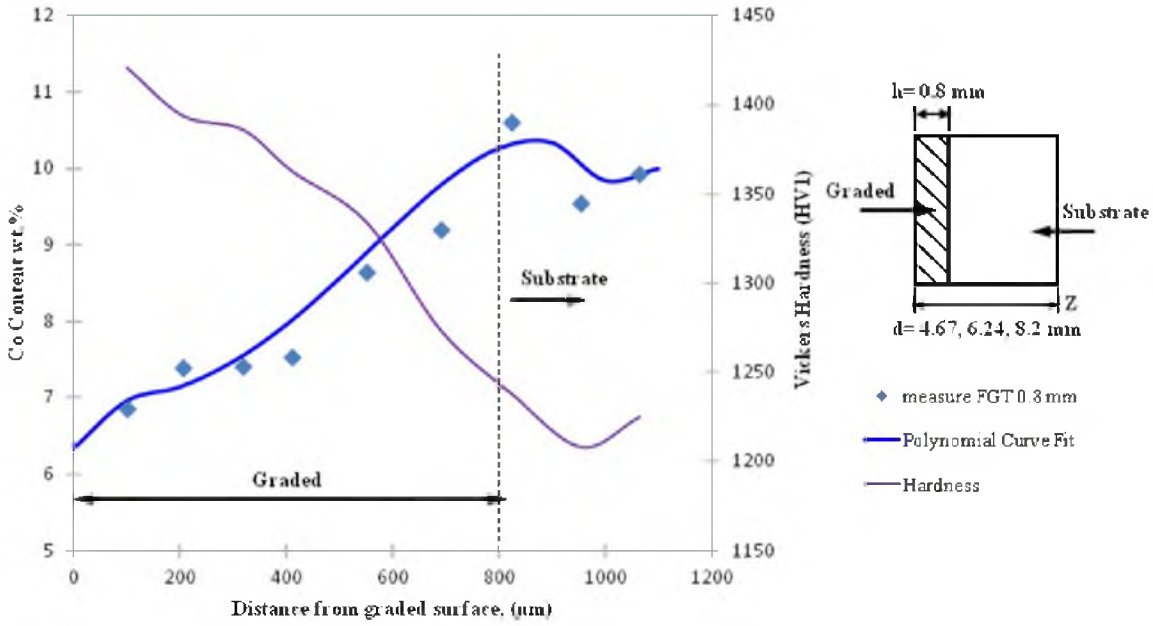

Figure 3.20 Gradient profile of Co content for flat WC10Co specimen with gradient thickness of 0.8 mm.

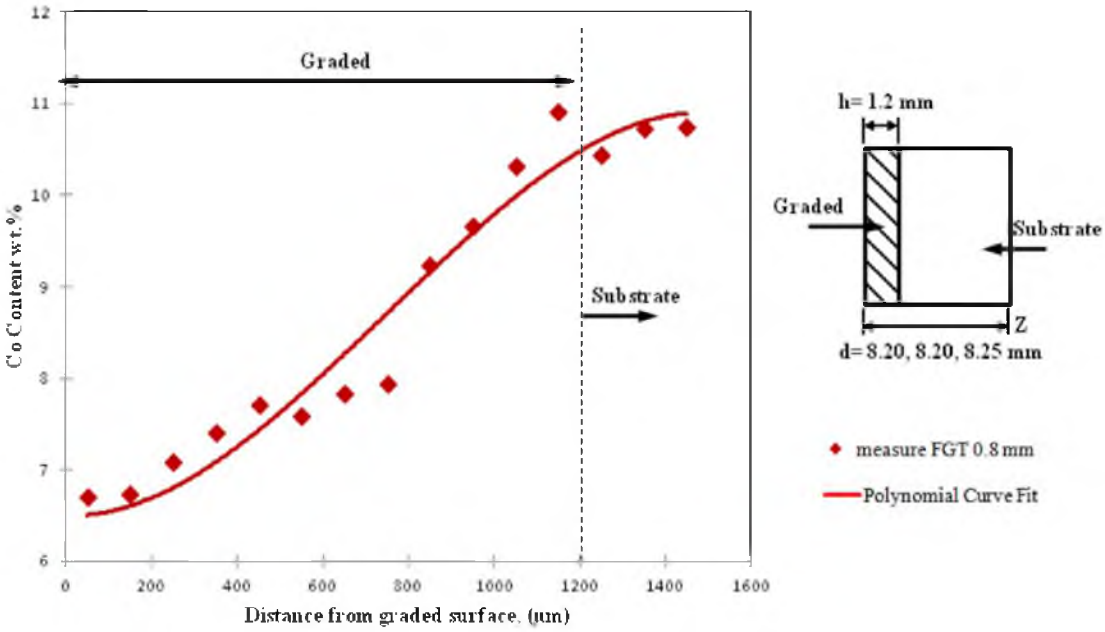

Figure 3.21 Gradient profile of Co content for flat WC10Co specimen with gradient thickness of 1.2 mm.

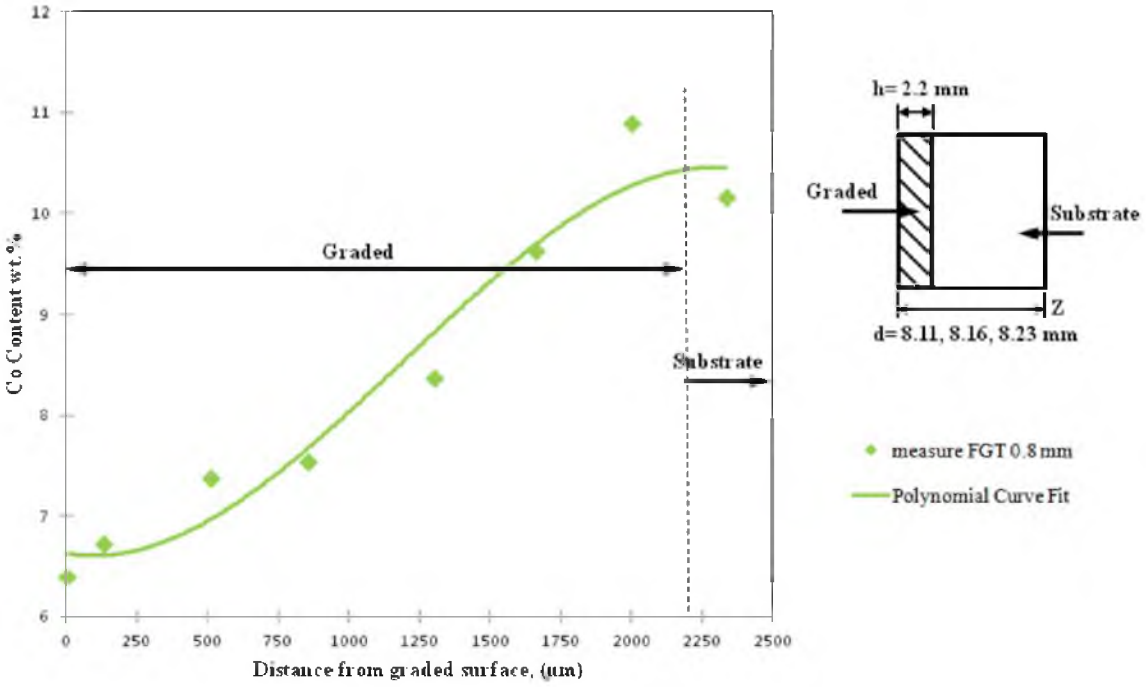

Figure 3.22 Gradient profile of Co content for flat WC10Co specimen with gradient thickness of 2.2 mm.

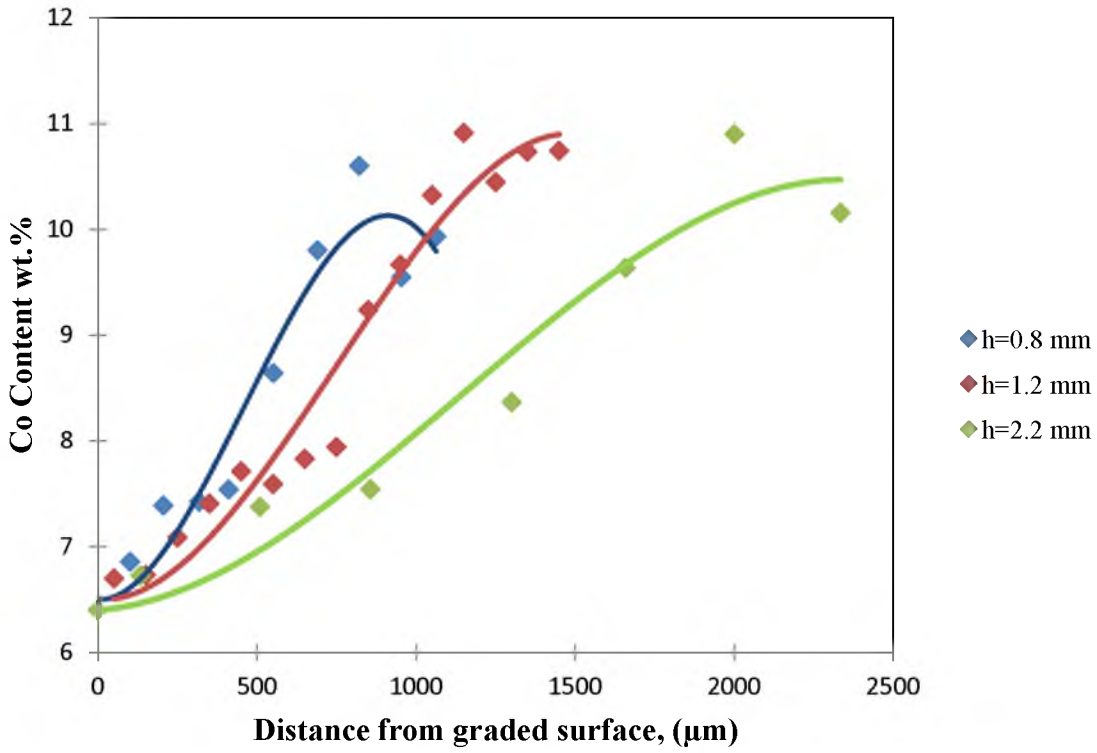

Figure 3.23 Comparison of Co gradient profiles for different gradient thicknesses, 0.8 mm, 1.2 mm and 2.2 mm.

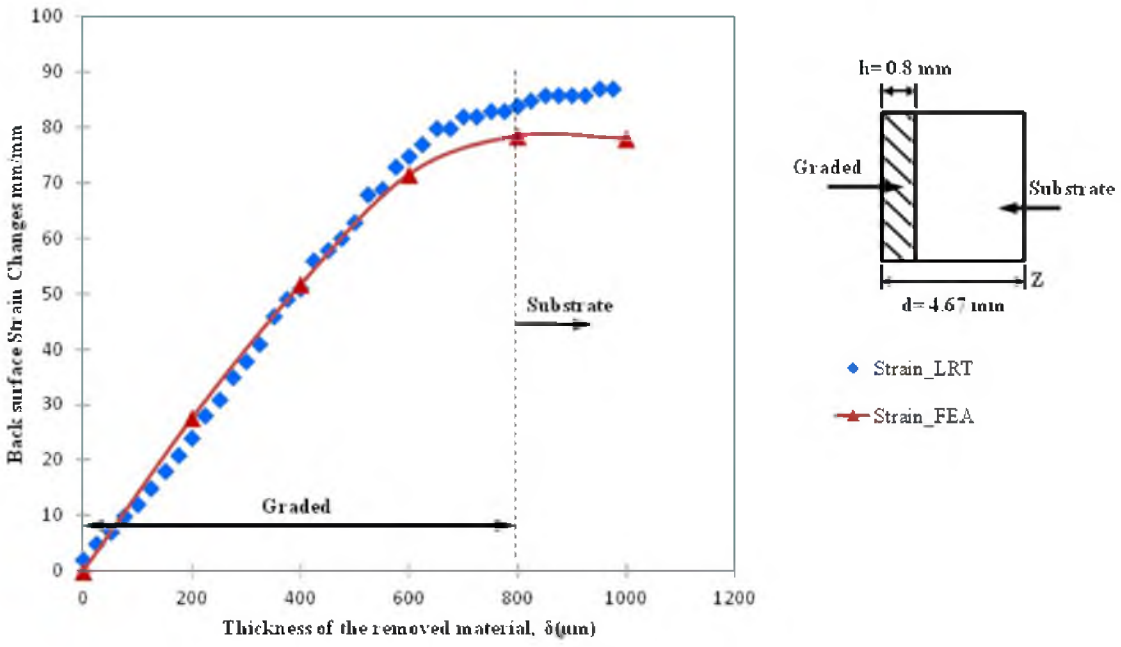

Figure 3.24 Back-face strain changes determined by FEA modeling and the experimental (LRT) process as a function of the removed material from the graded region for sample 1 with a gradient region thickness, *h*=0.8 mm, and total sample thickness of 4.67 mm.

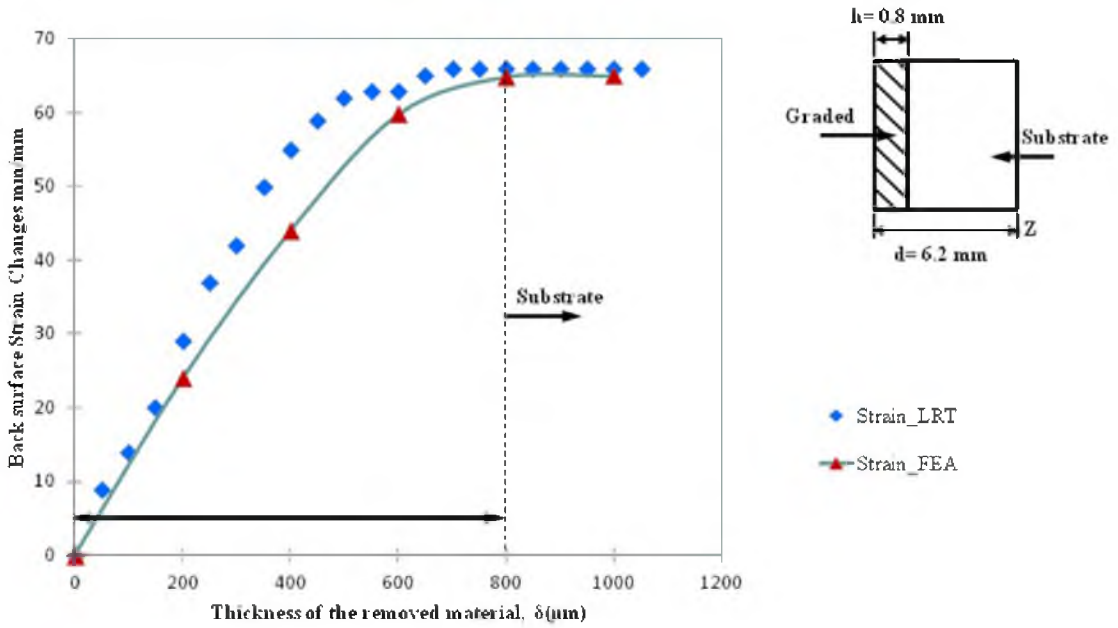

Figure 3.25 Back-face strain changes determined by FEA modeling and the experimental (LRT) process as a function of the removed material from the graded region for sample 2 with a gradient region thickness, h=0.8 mm, and total sample thickness of 6.2 mm.

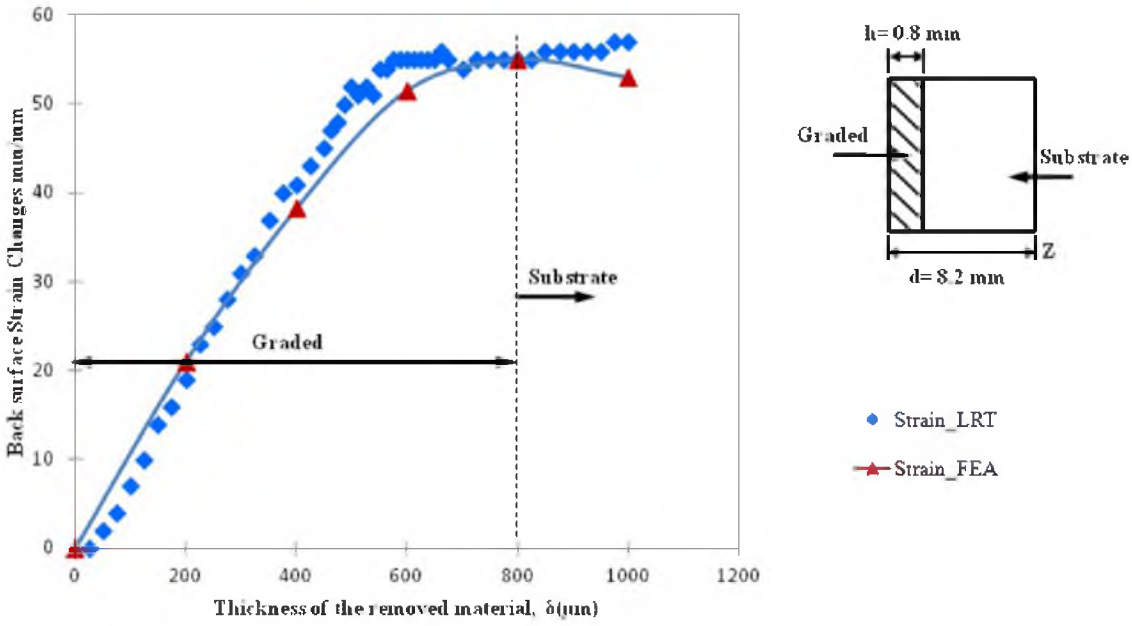

Figure 3.26 Back-face strain changes determined by FEA modeling and the experimental (LRT) process as a function of the removed material from the graded region for sample 3 with a gradient region thickness, h=0.8 mm, and total sample thickness, d=8.2 mm.

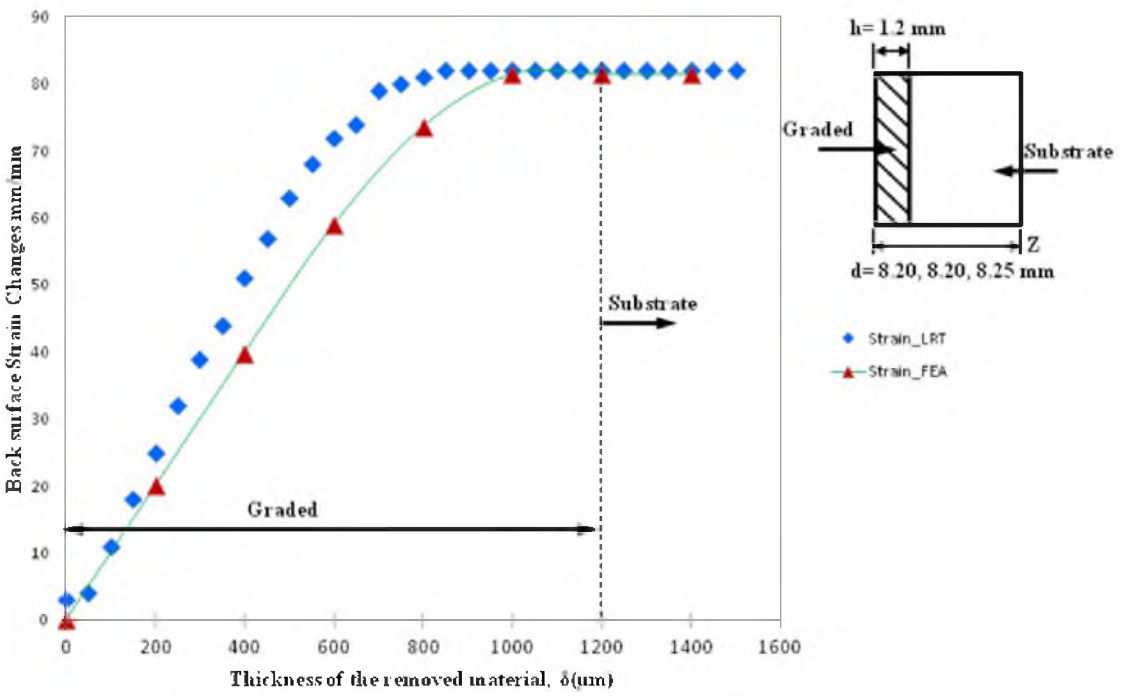

Figure 3.27 Back-face strain changes determined by FEA modeling and the experimental (LRT) process as a function of the removed material from the graded region for samples 4, 5 and 6 with gradient region thickness, *h*=1.2 mm, and total sample thickness of approximately 8.2 mm.

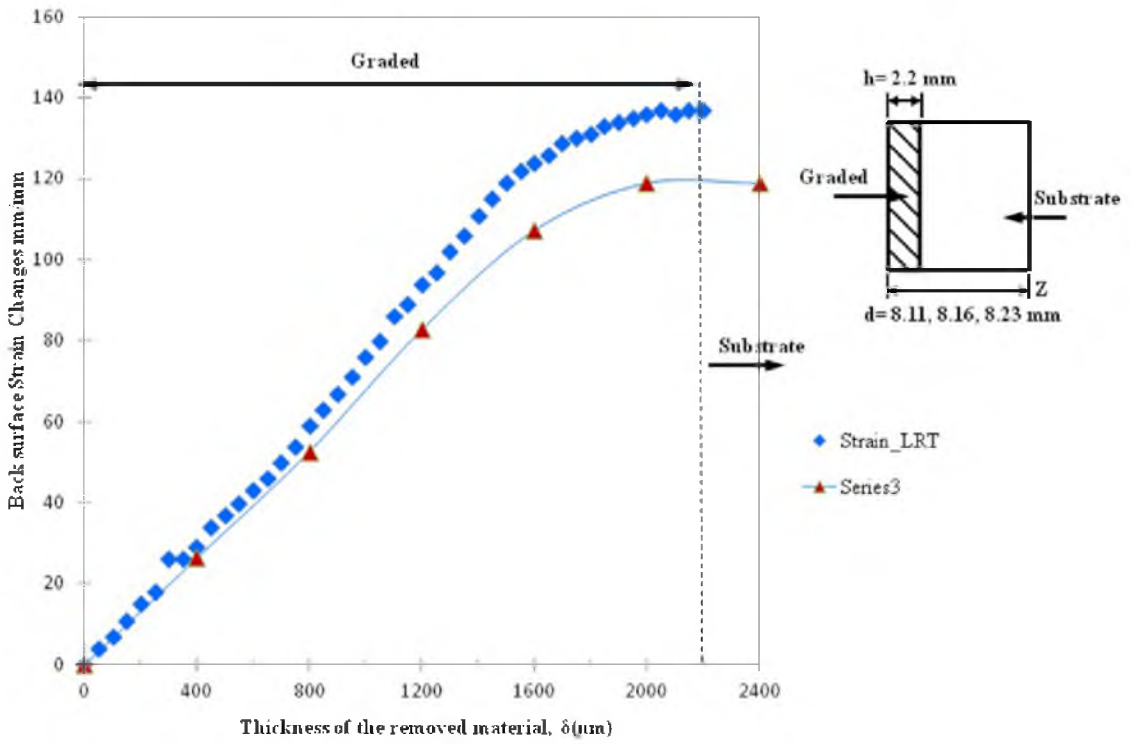

Figure 3.28 Back-face strain changes determined by FEA modeling and the experimental (LRT) process as a function of the removed material from the graded region for samples 7, 8 and 9 with a gradient region thickness, *h*=2.2 mm, and total sample thickness of approximately 8.15 mm.

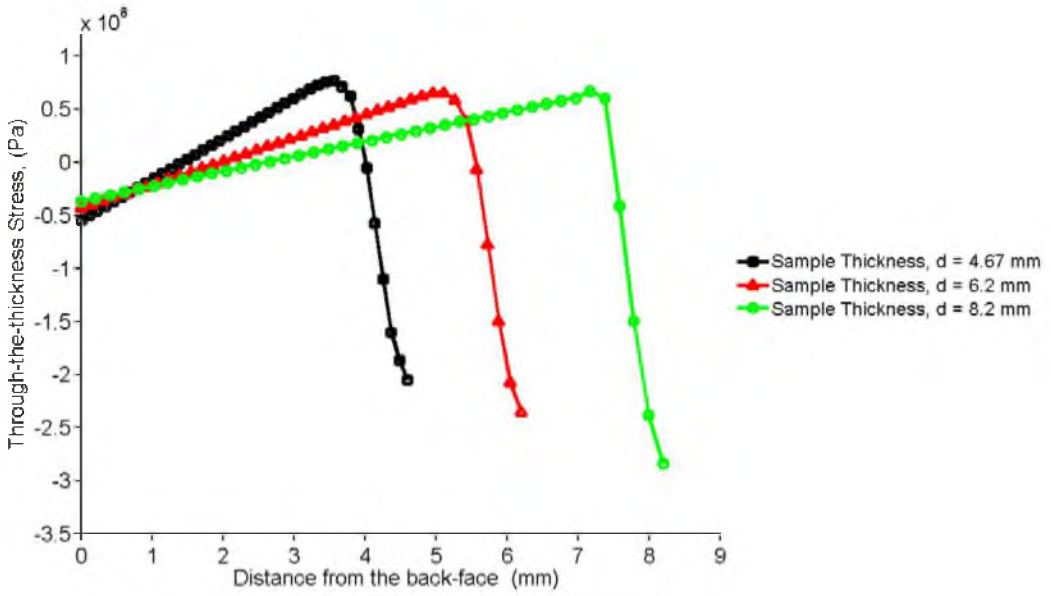

Figure 3.29 Residual stress distribution in FG WC10Co using FEA showing the effect of total sample thickness, *d*, on the magnitudes and distribution of residual stress for samples with constant gradient thickness, *h*=0.8 mm.

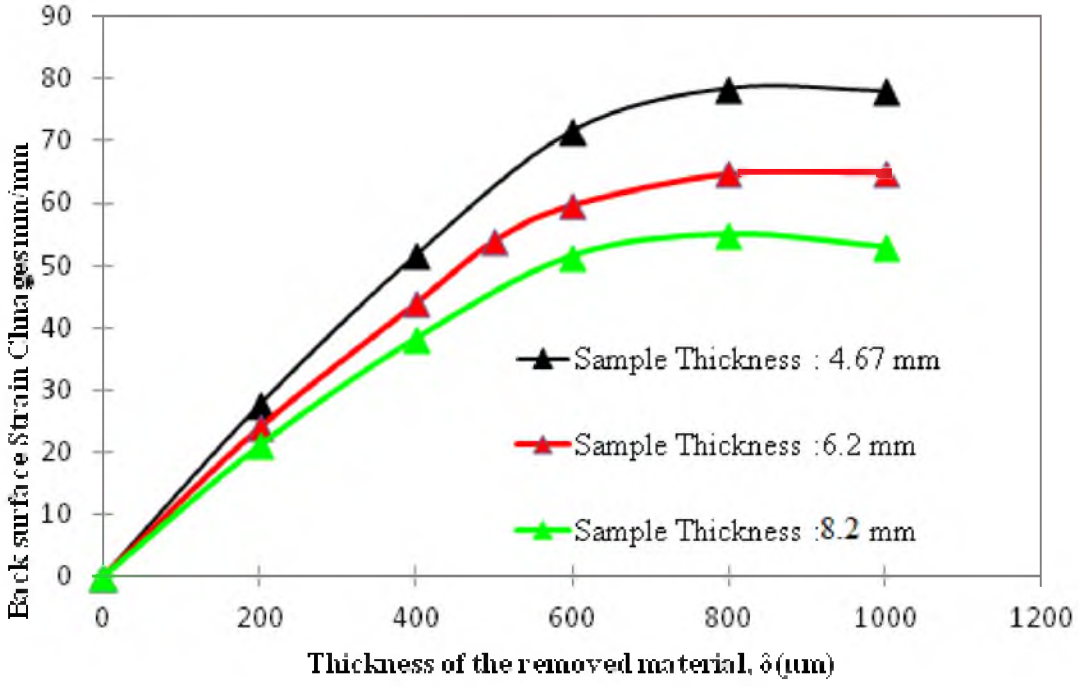

Figure 3.30 Back-face strain calculated by FEA as a function of the thickness of the removed FG material for a gradient profile thickness of 0.8 mm with different sample thicknesses, *d*=4.67 mm, 6.27 mm and 8.2 mm.

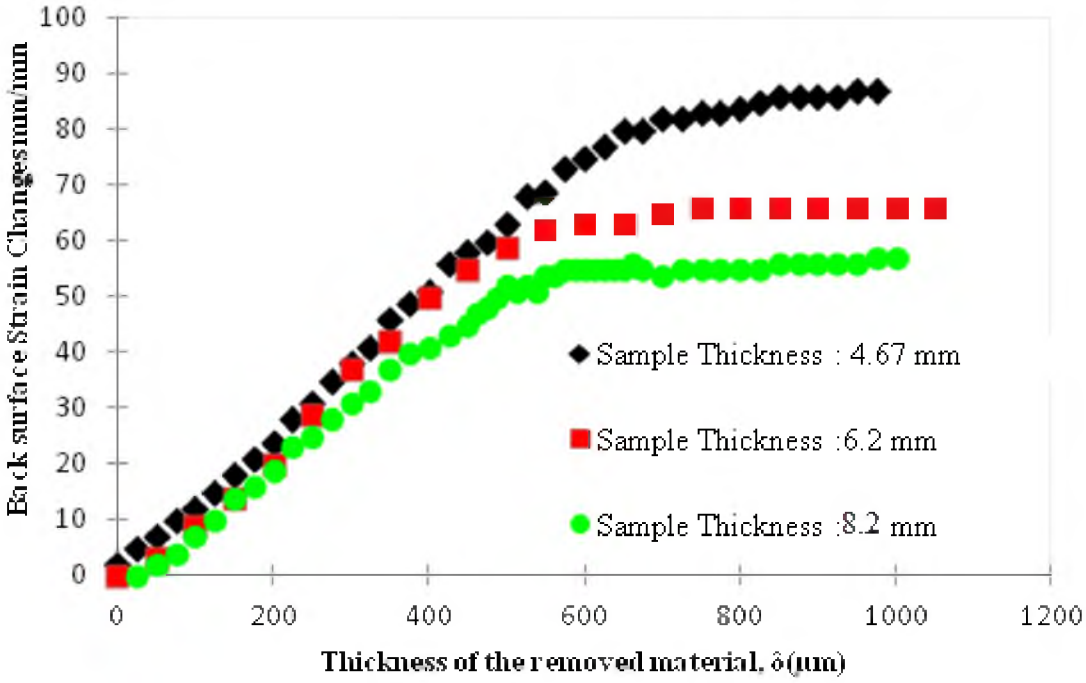

Figure 3.31 Experimental LRT back-face strain measured as a function of the thickness of the removed FG material for a gradient profile thickness of 0.8 mm with different sample thicknesses, *d*=4.67 mm, 6.27 mm and 8.2 mm.

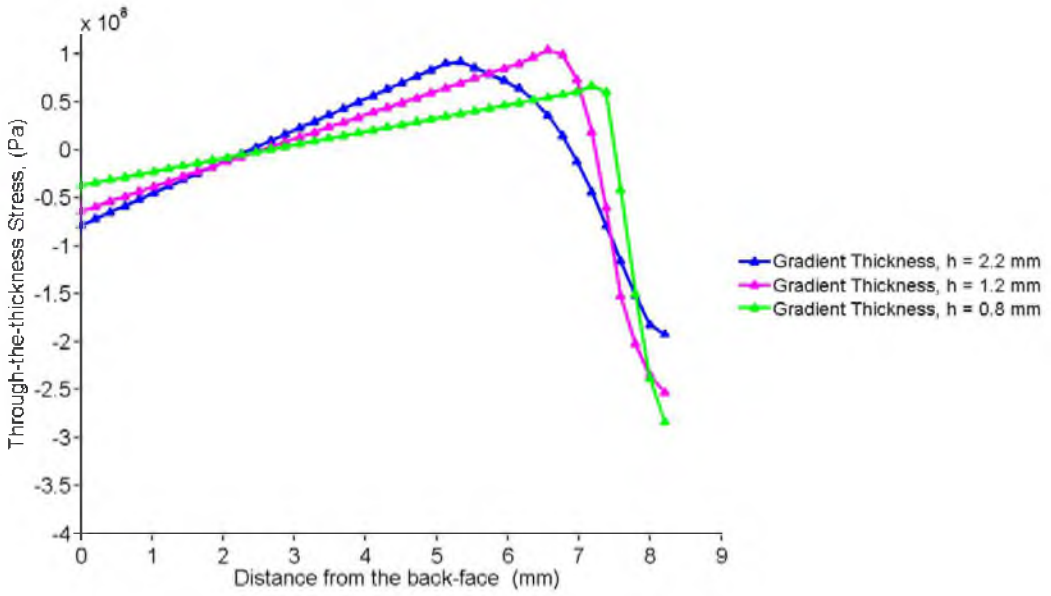

Figure 3.32 Residual stress distribution in FG WC10Co using FEA, showing the effect of gradient thickness on the magnitudes and distribution of residual stress for WC-10Co with constant sample total thickness, d=8.2 mm, and different gradient thicknesses, h=0.8 mm, 1.2 mm and 2.2 mm.

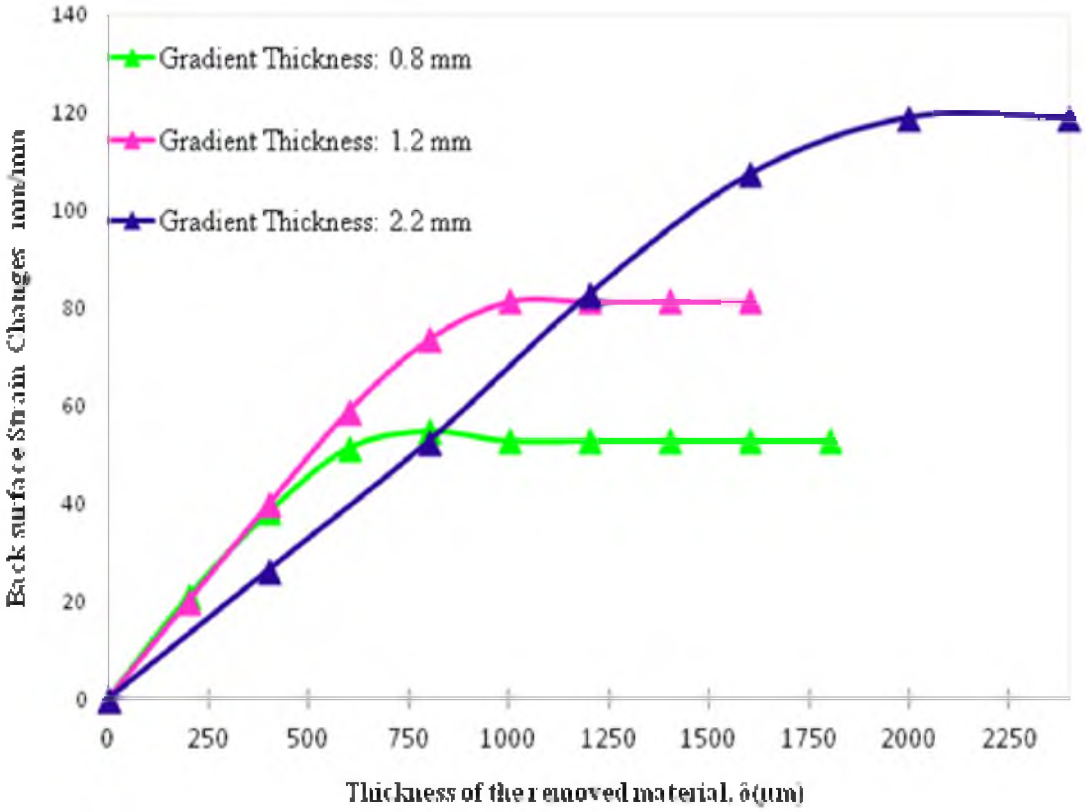

Figure 3.33 Back-face strain calculated by FEA as a function of the thickness of the removed material for a sample thickness of d=8.2 mm with different gradient profiles and thicknesses, h=0.8 mm, 1.2 mm and 2.2 mm.

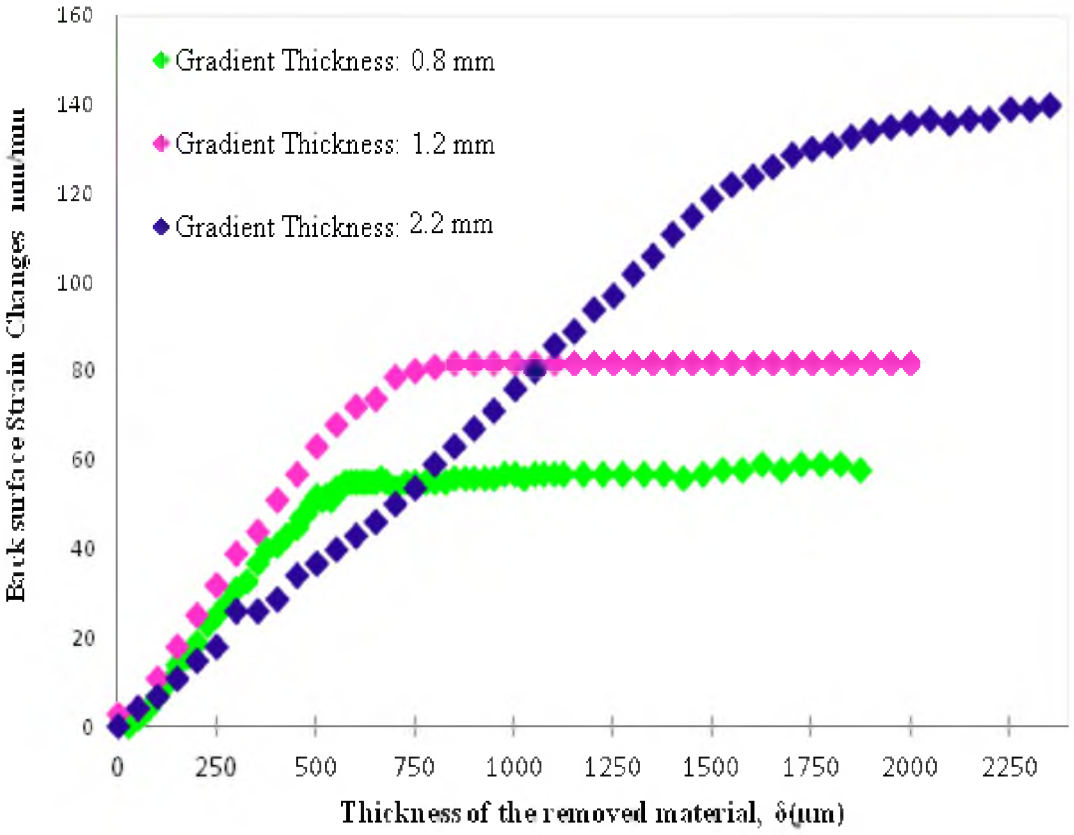

Figure 3.34 Back-face strain calculated by LRT as a function of the thickness of the removed material for a sample thickness of d=8.2 mm with different gradient profiles and thicknesses, h=0.8 mm, 1.2 mm and 2.2 mm.

CHAPTER 4

MODELING RESIDUAL STRESS IN OTHER GEOMETRIC SHAPES

4.1 Cylindrical Functionally Graded WC-Co Inserts

4.1.1 Overview

The thermal residual stress distribution in a functionally graded cemented tungsten carbide (FG-WC-Co) hollow cylinder was examined with an emphasis on the effects of key variables, such as gradient profile and gradient thickness on the magnitude and distribution of the stress field. An analytical direct solution based on solving the governing equations of a cylinder composed of a uniform inner core and a functionally graded outer shell was developed, considering the cylindrical compound as two separate elements: a homogeneous cylinder and a functionally graded shell. Through the graded shell, material properties such as the modulus of elasticity and the coefficient of thermal expansion (CTE), except Poisson's ratio, were considered to vary as a power function of the radius, and proper mechanical boundary conditions were imposed at the interface of the two cylinders. Practical values for the two variables, gradient profile and gradient thickness, were evaluated in the mathematical solution for the FG-WC-Co compound, and their effects on the stress distribution were studied. An examination of different gradient profiles showed that with excess Co content in the graded region, compressive

radial stresses were created, while with decreasing Co content through the graded region tensile stresses were generated at the interface. The effect of gradient thickness was shown to have a greater effect on radial stress, compared to hoop stress, and increasing the gradient thickness significantly increased the radial stress magnitude.

4.1.2. Analytical Derivations

To establish an analytical model, a long cylinder is deemed as the superposition of two separate elements: one a hollow homogeneous cylinder and the other a hollow FGM cylinder, Figure 4.1. The analytical model is presented in the form of mathematical equations, which describe the stress distribution for the cylindrical compound. Stress-strain, compatibility and equilibrium equations were expanded for both homogeneous and FGM cylinders. The set of ordinary differential equations (ODEs) obtained from each element mathematical expansion was solved analytically; and the parametric constants that emerged in the solutions of the ODEs were then calculated by satisfying the mechanical boundary conditions. The final comprehensive stress distribution was calculated by substituting the constants into the mathematical solutions.

4.1.2.1. Homogeneous Hollow Cylinder

In a homogeneous hollow cylinder, with constant elastic modulus (E), CTE(α) and Poisson ratio (ν), the stress-strain equations for radial stress, σ_r, and hoop stress, σ_θ, considering zero axial displacement, $w = 0$, and plane strain condition, $\varepsilon_z = 0$, under uniform thermal load, ΔT, are given as follows [151]:

$$\sigma_r = \frac{E(1-\nu)}{(1+\nu)(1-2\nu)}\varepsilon_r + \frac{E\nu}{(1+\nu)(1-2\nu)}\varepsilon_\theta - \frac{E}{(1-2\nu)}\alpha\Delta T \tag{4.1a}$$

$$\sigma_\theta = \frac{E(1-\nu)}{(1+\nu)(1-2\nu)}\varepsilon_\theta + \frac{E\nu}{(1+\nu)(1-2\nu)}\varepsilon_r - \frac{E}{(1-2\nu)}\alpha\Delta T \tag{4.1b}$$

The compatibility equations for plane strain and axisymmetric conditions in the cylindrical coordinate system *r, θ, z,* with corresponding displacement components *u, v, w,* are reduced to the two following components [151]:

$$\varepsilon_r = \frac{du}{dr} \tag{4.2a}$$

$$\varepsilon_\theta = \frac{u}{r} \tag{4.2b}$$

Accordingly, shear stresses are zero and other stress components do not change with respect to *z*. Therefore, radial stress σ_r, and hoop stress, σ_θ, satisfy the equilibrium equation as follows:

$$\frac{d\sigma_r}{dr} + \frac{1}{r}(\sigma_r - \sigma_\theta) = 0 \tag{4.3}$$

Substituting equations (4.1a), (4.1b), (4.2a) and (4.2b), in the equilibrium equation, (4.3), the ordinary differential equation (ODE) for the radial displacement component, *u,* is as follows:

$$u'' + \frac{1}{r}u' - \frac{1}{r^2}u = 0 \tag{4.4}$$

This is an Euler differential equation with the following general solution:

$$u^{g}_{\mathrm{hom}\,o}(r) = A_1 r + A_2 r^{-1} \tag{4.5}$$

In which, A_1 and A_2 are parametric constants that will be calculated later. Using the general solution for the displacement ODE, equation (4.5), in the stress-strain equations (4.1a and 4.1b), stress components are rewritten as follows :

$$\sigma_{r_{\mathrm{hom}\,o}} = \frac{E}{(1+\nu)(1-2\nu)}\left(A_1 - (1-2\nu)\frac{A_2}{r^2} - (1+\nu)\alpha\Delta T\right) \tag{4.6a}$$

$$\sigma_{\theta_{\mathrm{hom}\,o}} = \frac{E}{(1+\nu)(1-2\nu)}\left(A_1 + (1-2\nu)\frac{A_2}{r^2} - (1+\nu)\alpha\Delta T\right) \tag{4.6b}$$

The above equations describe the distribution of stress components in the homogeneous core of the cylindrical compound. The same approach was followed to derive stress distribution in the FGM hollow cylinder; and then, by implementing the boundary conditions into the solution, parametric constants were calculated and the stresses were quantitatively evaluated.

4.1.2.2. FGM Hollow Cylinder

In the case of a long hollow cylinder with a compositional gradient, where the elastic modulus $E(r)$ and CTE $\alpha(r)$ are functions of the radius, and Poisson ratio, ν, is constant, σ_r and σ_θ were derived as follows [152]:

$$\sigma_r = \frac{E(r)(1-\nu)}{(1+\nu)(1-2\nu)}\varepsilon_r + \frac{E(r)\nu}{(1+\nu)(1-2\nu)}\varepsilon_\theta - \frac{E(r)}{(1-2\nu)}\alpha(r)\Delta T \tag{4.7a}$$

$$\sigma_\theta = \frac{E(r)(1-\nu)}{(1+\nu)(1-2\nu)}\varepsilon_\theta + \frac{E(r)\nu}{(1+\nu)(1-2\nu)}\varepsilon_r - \frac{E(r)}{(1-2\nu)}\alpha(r)\Delta T \tag{4.7b}$$

In a FGM cylinder, the compositional gradient is a function of radius in the form of the following power function:

$$w(r) = w_0 r^p \tag{4.8a}$$

In which, *w(r)* is the weight fraction of metal in the cer-met composite as a function of the radius. The power function exponent, p, characterizes the shape of the distribution and w_0 is a parametric constant, which was calculated using the value of w in the homogeneous core. Corresponding to the composition gradient, the modulus of elasticity and CTE are also expressed as power functions of the radius:

$$E(r) = E_0 r^m \tag{4.8b}$$

$$\alpha(r) = \alpha_0 r^n \tag{4.8c}$$

In which, m and n are the power exponents, which represent the mechanical properties variation and are calculated using a given compositional gradient. Similarly, E_0 and α_0 are parametric constants, which were calculated using the values of E and α in the homogeneous core. Modified stress-strain equations for the hollow cylinder with compositional variation, (4.7a) and (4.7b), as well as the expressions for the material properties, (4.8b) and (4.8c), are substituted into the compatibility and equilibrium

equations, (4.2a), (4.2b) and (4.3). Due to the similar mechanical and thermal loadings and boundary conditions considered in the homogeneous cylinder, the same compatibility and equilibrium equations, (4.2a), (4.2b) and (4.3), were satisfied in the FGM cylinder. The ODE, which governs the FGM hollow cylinder, was derived as:

$$u'' + (m+1)\frac{1}{r}u' + (\frac{\nu m}{1-\nu} - 1)\frac{1}{r^2}u = C_0 r^{n-1} \tag{4.9}$$

This is an Euler differential equation, where:

$$C_0 = (\frac{1+\nu}{1-\nu})\alpha_0 (m+n)\Delta T \tag{4.10}$$

The general solution for equation (4.10) is:

$$u^g_{FGM}(r) = Br^{\beta} \tag{4.11}$$

In which, B and β are parametric constants. Substituting equation (4.11) in (4.9) using compatibility equations, (4.2a) and (4.2b), the parametric constant, β, was calculated from the following equation:

$$\beta^2 + m\beta + (\frac{\nu m}{1-\nu} - 1) = 0 \Rightarrow \beta_{1,2} = -\frac{m}{2} \pm [(\frac{m^2}{4} - (\frac{\nu m}{1-\nu} - 1))]^{1/2} \tag{4.12}$$

Thus, the general solution is:

$$u^g_{FGM}(r) = B_1 r^{\beta_1} + B_2 r^{\beta_2} \tag{4.13}$$

The particular solution was assumed to be of the following form:

$$u_{FGM}^{P}(r) = Cr^{m_2+1} \tag{4.14}$$

Similarly, by substituting (4.14) in (4.9), C was calculated as follows:

$$C = \frac{C_0}{n(n+1)+(m+1)(n+1)+(\frac{\nu m}{1-\nu}-1)} \tag{4.15}$$

Solution for equation (9) is the sum of the general solution and the particular solution which is the sum of equations (13) and (14), and can be written as follows:

$$u_{FGM}(r) = u_{FGM}^{g}(r) + u_{FGM}^{P}(r) = B_1 r^{\beta_1} + B_2 r^{\beta_2} + Cr^{n+1} \tag{4.16}$$

Using the derived total solution for the displacement, stress components with respect to the solution for the displacement were rewritten as follows:

$$\sigma_{r_{FGM}} = \frac{E_0}{(1+\nu)(1-2\nu)} \begin{bmatrix} ((1-\nu)\beta_1 + \nu)B_1 r^{m+\beta_1-1} \\ +((1-\nu)\beta_2 + \nu)B_2 r^{m+\beta_2-1} \\ +(((1-\nu)n+1)C - (1+\nu)\alpha_0 \Delta T)r^{n+n} \end{bmatrix} \tag{4.17}$$

4.1.2.3. Boundary Conditions

The compound cylinder was subjected to external pressure and also to a uniform thermal load. The homogeneous cylinder was exposed to only uniform thermal load while the FGM cylinder was subjected to the uniform thermal load and also the external pressure. At the interface of the hollow homogeneous cylinder and the hollow FGM cylinder, $r = b$, the displacement induced by the thermal load applied to the homogeneous cylinder is different from the one related to the FGM cylinder, however,

the compound cylinder should deform as a solid one-piece element. Therefore, considering the analogy of this problem to the shrink fit conditions, the same technique can be used to describe the boundary condition at the interface [153]. The displacement due to the thermal load at $r = b$, can be calculated for each individual cylinder. The difference in displacement between the two cylinders was then used as the δ in the shrink fit equation of a compound cylinder. The pressure at the interface, P, can be calculated from the shrink-fit equation and used in further boundary conditions. Having P at the interface, the compound cylinder was converted to one homogeneous hollow cylinder with external pressure of P and one FGM hollow cylinder with internal pressure of P and external pressure P_o. Radial stresses at $r = a, b$ and c, are as follows:

$$\sigma_{r_{\text{hom}\,o}}(a) = 0 \tag{4.18a}$$

$$\sigma_{r_{\text{hom}\,o}}(b) = P \tag{4.18b}$$

$$\sigma_{r_{FGM}}(b) = P \tag{4.18c}$$

$$\sigma_{r_{FGM}}(c) = P_0 \tag{4.18d}$$

Substituting the boundary conditions in the equations (4.6a) and (4.17) for the radial stress component, σ_r, which were derived for both homogeneous and FGM cylinders, in order to simplify the set of equations, the parametric constants are defined as follows:

$$D_{11} = 1 \qquad D_{12} = -(1-2\nu)/a^2 \qquad D_{13} = D_{14} = 0$$

$$D_{15} = -(1+\nu)\alpha_0 \Delta T b^n \tag{4.19a}$$

$$D_{21} = 1 \qquad D_{22} = -(1-2\nu)/b^2 \qquad D_{23} = D_{24} = 0 \tag{4.19b}$$

$$D_{31} = D_{32} = 0 \qquad D_{33} = \left((1-\nu)\beta_1 + \nu\right) b^{\beta_1 - 1} \tag{4.19c}$$

$$D_{41} = D_{42} = 0 \qquad D_{43} = \left((1-\nu)\beta_1 + \nu\right) c^{\beta_1 - 1} \tag{4.19d}$$

All the parametric constants, D_{11} to D_{45}, in the above equations, (4.19a) to (4.19d), can be calculated for a prescribed problem with specific geometry, a, b and c, uniform thermal loading, ΔT and material properties, E_0, α_0 and ν. For given compositional variation, *p*, the gradient variables, *m* and *n*, which are power indexes for *E* and *CTE*, were estimated and then β_1 and β_2 were calculated from equation (4.12). A system of four-equations-four-unknowns were created by substituting equations (4.19a) to (4.19d) into equations (4.18a) to (4.18d) and then the unknowns, A_1, A_2, B_1 and B_2, were obtained by solving this system of equations. In equations (4.6a) and (4.17), which express the radial stress fields in the homogeneous and FGM cylinders, A_1, $A2$, B_1 and B_2 are the only unknown parameters. Other parameters can be calculated from either the given material properties and input loading conditions, such as: E, E_0, ν, α_0, α and ΔT or the power function exponent, *p*. For WC-Co tools, *m* and *n* are estimated from the Co content and its related values for the E and α at the interface of the homogeneous and FGM cylinders. Having the values of *m* and *n*, other dependent parameters such as: β_1, β_2 and C were computed. Therefore, having all the parameters defined or calculated, radial stress distribution and similarly hoop stress distribution are predictable using

equations (4.6a), (4.6b) and (4.17). In the next section, different types of composition gradient, as characterized by different power function exponents, are considered and different stress components corresponding to different types of distributions are analyzed and discussed.

4.1.3. Results and Discussion

As mentioned in the introduction, WC-Co is widely used in applications in which very high hardness and wear resistance are demanded. Hardness and abrasion resistance of WC-Co are controlled primarily by the tungsten carbide grain size, as well as the cobalt content. In general, as cobalt content is increased, tougher but less abrasion-resistant WC-Co is obtained. Cobalt contents range from about 2 to 13 wt. % for metal-cutting tools, and 6 to 16 wt. % for rock drilling tools, which can be extended to 30 % for press tools, swaging dies and other wear parts subject to moderate or severe shock.

Considering this range of cobalt content for WC-Co and material properties for each composition, different types of cobalt gradient distribution profiles from the homogeneous core to the surface of the graded region were considered. Different types of cobalt gradients can be described by equation (8a) using different values for the power function, p. The modulus, E, and CTE change accordingly, based on equations (4.8b and 4.8c) with varying exponents, m and n.

Typical types of distributions of Co that were considered are shown in Figure 4.2. Type I has Co distributions with higher Co content in the graded region (at the surface) than in the core ($p>0$ in Figure 4.2), while type II has Co distributions with lower Co content in the graded region than in the core ($p<0$ in Figure 4.2). The distribution of

residual stresses, hence mechanical and thermal properties, is a direct function of the distribution of cobalt. In Figure 4.2, $p = 0$ represents a fully homogeneous cylinder, which results in a stress-free component. In the WC-Co composite system higher cobalt content results in a softer composite, giving rise to a lower modulus of elasticity and higher coefficient of thermal expansion. Therefore, when considering the power function exponents of the distribution functions of the elastic modulus, with increasing cobalt content, the exponent, *m*, decreases, and with CTE, the exponent, *n*, increases.

In the process of making functionally graded WC-Co produced through a carburizing heat treatment technique [7, 150], different compositional profiles, i.e., different types of distributions, and also different gradient thicknesses, can be produced by varying the heat treatment temperature and atmospheric conditions. For example, applying the FG process to a homogeneous WC-15 wt. % Co cylinder, different gradient profiles ranging from 5-15 wt. % Co can be obtained at the surface.

In the analytical model, a WC-15 wt. % Co cylindrical insert with a graded region from the surface to the depth *H*, was considered. Thus, the cylindrical model consisted of a hollow homogeneous cylinder with inner radius *a* and outer radius *b*, superimposed by a FG-WC-Co shell with outer radius *c*. The Co content in the homogenous core of the cylinder was maintained at 15 wt. % from $r = a$ to $r = b$ and varied gradually as a power function of the radius from $r = b$ to $r = c$. In the uniform region, the material properties, i.e., elastic modulus (E) and CTE values for WC-15 wt. % Co are equal to 500 GPa and $6.6 \times 10^{-6} / ^{\circ} C$, respectively, and for the FGM outer shell cylinder, E and CTE vary with the radius, following the power functions (equations 4.8b and 4.8c), and input values of $\Delta T = -1100$ and $P_o = 0$ were considered as the loading conditions.

4.1.3.1. Effect of Cobalt Gradient Profile on Residual Stresses

Different profiles of Co variations were shown in Figure 4.2, and Type I and Type II profiles were defined, respectively, as increasing and decreasing trends of Co content from the interface of the two regions to the surface of the cylinder. Lower Co value at the surface represents higher hardness and elastic modulus. Lower CTE at the surface, which is characterized by positive values of m and negative values of n. Higher Co values at the surface represent lower hardness and elastic modulus and higher CTE at the surface, which is represented by negative values of m and positive values of n. For industrial applications, considering the superior combinations of mechanical properties, Type II profiles are usually preferred. However, applications for Type I are in practice and both Type I and Type II profiles were analyzed in this study to achieve better understanding of the effects of the gradient on the residual stress distributions.

As a result of the variations of Co content and corresponding variations of E and CTE, Figure 4.3 shows the radial stress distribution for different types of gradient distributions. The radial stress at the interface is indicated by σ_b on the y-axis of Figure 4.3, and the variation of σ_b for different values of the power function exponent p are given. The maximum radial stress occurred at the interface between the homogeneous and FGM region. The absolute magnitude of σ_b decreased when the value of the power function exponent, p, increases. Negative values of σ_b corresponded to $p>0$, and positive values of σ_b corresponded to when $p<0$. Thus, a sharper variation of material properties at the interface resulted in a larger magnitude of radial stress at the interface. Generally, compressive radial stresses at the interface would be desirable, although low magnitude tensile stresses may be tolerated without failure of the component.

The radial stress distribution was normalized by the magnitude of radial stress at the interface for each type of gradient profile, and is indicated by $-\sigma_r / \sigma_b$, as shown in Figure 4.4. The effect of the gradient profile on the distribution of radial stress is shown in Figure 4.4, while the effect of the gradient profile on the magnitude of radial stress is given in Figure 4.3. Figure 4.4 shows that once normalized, the radial stress distribution was very similar for all values of p examined.

The hoop stress along the radius is illustrated in Figure 4.5 and Figure 4.6. The hoop stress for $p > 0$ had a positive constant magnitude in the homogeneous region. However, in the FGM region it decreased along the radius, having a negative magnitude.

The absolute magnitude of the hoop stress increased as p was decreased in this range. For $p<0$, i.e., Type II gradient profile, the hoop stress showed a negative constant magnitude in the homogeneous core, which increased with radius and had a positive value in the FGM region. The absolute magnitude of the hoop stress was larger for $p>0$ than for $p<0$ (Type II).

4.1.3.2. Effect of Gradient Thickness

The gradient thickness is represented by H/a, which is the ratio of the thickness of the gradient over the inner radius of the cylindrical insert. Figures 4.7 and 4.8 show the distribution of elastic modulus and thermal expansion coefficient, respectively, along the radial direction of the component for different values of H/a, while the gradient profile remains constant p = -0.6. In this analytical study the thickness ratio, H/a, was varied from 1 to 8.

Figure 4.9 shows the radial stress distribution for different values of gradient

thickness. The radial stress at the interface is σ_b. The radial stress distribution was normalized by the absolute magnitude of radial stress at the interface for $H/a=8$ and expressed as $\sigma_r/\left|(\sigma_b)_{H/a=8}\right|$ in Figure 4.9. The variation of the radial stress distribution and σ_b for different values of gradient thickness is shown in this plot. For each value of gradient thickness, the maximum magnitude of radial stress occurred at the interface between the homogeneous and FGM regions, which is σ_b. The magnitude of σ_b was larger for thicker gradients. The wide range of the variation of the radial stress distribution, shown in Figure 4.9, indicates the high sensitivity of the radial stress to the gradient thickness. Although the maximum stress increased for thicker gradient region, the rate of radial stress change from interface to surface was smaller for larger gradient thicknesses.

The hoop stress along the radius is illustrated in Figure 4.10 and Figure 4.11. The effect of gradient thickness on the magnitude and distribution of the hoop stress is shown in Figure 4.11. As shown, the hoop stress increased rapidly with increasing gradient thickness. In this specific case, the material properties are power functions of the radius with larger gradient thickness representing larger variation of the properties of material, which leads to large magnitudes of the radial and hoop stresses. Figure 4.11 shows that as the gradient thickness decreases the rate of hoop stress variation in the graded region increases.

4.2 FEA Modeling of Different Geometric Shapes: Cylinder

FG-WC-Co cylinder with gradient of Co composition from surface to depth *H* as shown in Figure 4.12 is considered. One-dimensional through-the-radius gradient is

assumed. Cylinder is considered to be homogeneous in $0 < r < R - H$ and heterogeneous (graded) in $R - H \leq r \leq R$. If V_{C1} is defined as the volume fraction of ceramic in the homogeneous region, $0 < r < R - H$, and V_{C2} is named as the volume fraction of ceramic at the surface of the graded region, $r = R$, the volume fraction of ceramic, V_C, in the graded region, $R - H \leq r \leq R$, varies according to the following function:

$$V_C(r) = (V_{C1} - V_{C2})\left(\frac{R - r}{H}\right)^N + V_{C2} \qquad for\ R - H \leq r \leq R \qquad (4.20)$$

Different profiles of Co gradient are considered as shown in Figure 4.13 to study the through-the radius residual stress distribution. Co composition varies from the greater value of 16 wt. % in the substrate and at the interface to the smaller value of 10 wt. % at the surface. This distribution of Co composition creates more wear resistance at the surface and more fracture toughness inside the insert. Therefore, during the cooling cycle of the heat treatment, the outer surface of the cylinder shrunk less rather than the inner core and accordingly, residual stress caused by the composition mismatch in the material is supposed to be compressive at the ceramic-riched region and tensile at the metal-riched part.

Elastic modulus, coefficient of thermal expansion and the Poisson's ratio are determined using equation (3.2) and (3.3) in Chapter 3. Due to the geometric symmetry in the cylindrical FG-WC-Co compound, two-dimensional model with axisymmetric boundary condition is considered. Figure 4.14 demonstrates the residual stress distribution across the two-dimensional FEA model. In this figure, two paths are also defined, one along the outer surface of the cylinder and the other through the radius of the

cylinder. Stress components along each path will be studied and discussed for different gradient profiles and gradient thicknesses. In this figure, the longitudinal stress distribution, σ_L, all over the volume is shown. Over the homogeneous substrate the stress is mostly in tension and reaches to its maximum value, 107MPa, at the intersection of homogeneous substrate and graded region. At the surface, compressive stress is recognized with the maximum value of -297MPa.

The radial stress, σ_R, distribution all over the volume is shown in Figure 4.15. At the surface, radial stress is zero due to boundary condition for free surface. Radial stress is smaller and less significant rather than the longitudinal stress since the material property mismatch is only in radius direction, which affect the longitudinal stress directly but the radial stress laterally.

4.2.1 Effect of Cobalt Gradient Profile on Residual Stresses

Figures 4.14 and 4.15 present two defined paths, one along the outer surface and the other one through the radius and at the middle of the cylinder. Longitudinal stress at the outer surface and as a function of its position from the cylinder base, along path 1, is demonstrated in Figure 4.16 for different profiles of Co gradient, shown before in Figure 4.13. Different profiles of Co variations are represented by N exponent. As seen from Figure 4.16, longitudinal stress component at the outer FGM surface of the FG-WC-Co cylinder, where Co value is lower at the surface rather than its value in depth, is a compressive stress. The magnitude of this compressive stress arising as the profile exponent, N, decreases. As presented, stress distribution for N values of 0.5, 1, 2 and 5 are considered. The maximum longitudinal stress at the outer surface, σ_{L_S}, belongs to the

Co profile represented by N=0.5 and is around -300MPa. This value of compressive stress is induced due to only 6% difference in Co content value between the surface and inside of the cylinder. It should be addressed that compressive stress at the surface is very desirable for cutting inserts applied in oil and gas drilling industry.

Another stress component on the surface is the radial stress, σ_{R_S}, which is perpendicular to the surface and therefore, due to the free surface condition, is zero all along the surface of the FGM cylinder. Due to the axisymmetric condition, all of the stress components in circumferential direction, θ, including σ_{θ_S}, $\tau_{R\theta_S}$ and $\tau_{L\theta_S}$ are zero.

Figure 4.17 shows the longitudinal stress along path 2, which has been defined in Figures 4.14 and 4.15 for different Co profiles, N values of 0.2, 0.5, 1, 2 and 5, while the ratio of gradient thickness over the total radius is constant, H/R=1/3. As a general trend, stress possesses a small value around the cylinder axis that will increase while moving from core to the interface of the homogeneous region and the FGM region. In the homogeneous region, for all the N values, stress has an increasing tensile trend, which reaches to its maximum value at the interface, where the homogeneous region ends. This variation is relatively linear and the variation slope of this increasing trend is directly related to the magnitude of N. Therefore, the maximum variation slope and the maximum value of tensile stress at the surface belongs to the N of 5 and vise versa the minimum tensile stress is referred to the N of 0.2. From the fatigue point of view, tensile stress inside the material is not desired, therefore it is an aim to determine the optimum gradient profile in order to postpone the component fracture and increase the life-length of a product.

Comparing the stress distribution in Figure 4.17 to the Co variation in Figure

4.13, it will be observed that in the graded region the stress trend almost follows the same trend of the Co profile that starts from the tensile stress at the interface and drops rapidly to a compressive stress with much bigger magnitude at the surface. However, it is also seen that for the values of 2 and 5, despite the Co profiles, the stress profiles are deviated from the gradient profile, which results in a smaller compressive stress at the surface. Since the bigger compressive stress at the surface is strongly preferred, the specific Co profile that creates a better combination of small tensile stress at the interface and large compressive stress at the surface can be introduced as the optimized gradient profile for this FG-WC-Co cylindrical compound. In this specific system, the optimum profile is referred to the N=0.5.

Figure 4.18 represents the radial stress distribution along path 2, through the radius, for different Co gradient profiles. Comparing the magnitude of radial stress, Figure 4.18, to the magnitude of longitudinal stress, Figure 4.17, it is observed that the average magnitude of radial stress is significantly smaller than the magnitude of longitudinal stress. The radial stress is around one-tenth of longitudinal stress. In addition, the radial stress trend does not follow the trend of the Co profile. Radial stress is always in tension and its maximum value happens at the cylinder axis and then decreases to the zero value at the surface. This is due to the free surface condition. The rate of radial stress variation varies as the value of N changes. Increasing the N value, the variation rate of through-the-radius radial stress also increases. According to the same tendency of having less tensile stress across the component, which was discussed before, the Co profile referred to the N value of 0.2 is preferred in term of radial stress.

4.2.2 Effect of Cobalt Gradient Thickness on Residual Stresses

Different profiles of Co gradient based on different values of gradient thicknesses are shown in Figure 4.19. Co composition varies from the greater value of 16 wt. % in the substrate, and at the interface, to the smaller value of 10 wt. % at the surface.

Longitudinal stress at the outer surface and as a function of its position from the cylinder base, along path 1, is demonstrated in Figure 4.20 for different Co normalized gradient thicknesses, *H/R*. Longitudinal stress component at the outer FGM surface of the FG-WC-Co cylinder, where Co value is lower at the surface than its value in depth, is a compressive stress. The magnitude of the compressive stress decreases as the gradient thickness, *H*, decreases. As presented, stress distribution for *H/R* values of 1/30, 1/15, 1/3, 1/2, 2/3 and 5/6, are considered. The maximum longitudinal stress at the outer surface, σ_{L_S}, belongs to the Co profile represented by *H/R*=1/30 (0.03333) and is around -450MPa. This value of compressive stress is induced due to only 6% difference in Co content value between the surface and inside of the cylinder.

Figure 4.21 shows the longitudinal stress along path 2. General trend for all gradient thicknesses are the same. As discussed in the last section, through-the-thickness longitudinal stress, starts from a tensile stress at the cylinder axis, which is then linearly increased to its maximum positive value of 100 MPa at the interface. Afterwards, in the graded region, a reverse trend is observed and stress decreases from the peak value to the compressive stress at the FGM surface. The initial value of stress on the axis of the cylinder, the compressive stress at the surface as well as the stress variation slopes in both homogeneous and FGM regions are highly affected by the gradient thickness value. As illustrated, the smaller the gradient thickness is, then the surface compressive stress and

the axial tensile stress are larger. This results in smoother slopes for larger values of normalized gradient thicknesses, *H/R*. Interestingly and despite the significant affect of gradient thickness on the stress distribution, the stress value at the interface, which is a tensile stress, does not vary that much by changing the gradient thickness.

Figure 4.22 represents the radial stress distribution along path 2, through the radius, for different values of gradient thicknesses. Comparing the magnitude of radial stress, Figure 4.22, to the magnitude of longitudinal stress, Figure 4.21, it is observed that the average magnitude of radial stress is significantly smaller than the magnitude of longitudinal stress. The radial stress is one order lower than the order of longitudinal stress. In addition, the radial stress trend does not follow the trend of the Co profile. Radial stress is always in tension and its maximum value happens at the cylinder axis and then decreases to the zero value at the surface, which is due to the free surface condition. The rate of radial stress variation varies as the value of gradient thickness changes. Increasing the *H/R* value, the variation rate of through-the-radius radial stress also increases, however, this growth slows and eventually ceases for big values of *H/R*. According to the same tendency of having less tensile stress across the component, the Co profile referred to the *H/R* value of 1/30 is preferred in terms of radial stress.

4.3 FEA Modeling of Different Geometric Shapes: Dome-top

FG-WC-Co dome-top compound with gradient of Co composition from surface to depth H as shown in Figure 4.23, is considered. One-dimensional through-the-radius gradient is assumed in this problem. The FGM insert is homogeneous in $0 < r < R - H$ and heterogeneous (graded) in $-H \leq r \leq R$. The Co variation follows the same function

considered for the FGM cylinder in the last section, (Eq. 4.20). Different profiles of Co gradient, the same as in the FGM cylinder, are considered to study the through-the-radius residual stress distribution. Co composition varies from the greater value of 16 wt. % in the substrate and at the interface to the smaller value of 10 wt. % on the surface.

Changes in Co composition result in a gradient in the mechanical properties of the material such as mechanical strength and thermal conductivity. Elastic modulus, coefficient of thermal expansion and the Poisson's ratio are determined using Eqs. (3-2) to (3-4) in Chapter 3. The thermomechanical properties differences in the material are the source of residual stress due to nonuniform deformations between the Co and WC during thermal and mechanical loadings. Due to the geometric symmetry in the dome-top FG-WC-Co compound, two-dimensional model with axisymmetric boundary condition is considered. Figure 4-24 demonstrates the residual stress distribution across the two-dimensional FEA model. Residual stress distribution can be engineered through different design and geometric parameters as well as engineering of mechanical and physical factors, such as Co gradient profile and gradient thickness. The optimized distribution of residual stress can improve the functionality and the performance of the FGM component by delaying crack initiation, which eventually postpones the compound's fracture.

Here, the residual stress is calculated using commercial finite element software, ANSYS. The residual stress distribution is affected by different parameters such as the Co gradient profile, gradient thickness and the geometric parameters of the FGM compound. To better understand the stress analysis and make a better comparison, specific paths are defined in the finite element model, Figure 4.25. These paths are selected based on the most critical locations in the compound, in terms of referring more

stress concentration and/or having more contact area to the rock, while employed as a cutting or machining tool.

As illustrated in Figure 4.25, three paths are defined. Path 1 is laid all along the surface from point A on the base plane to point B on the intersection of the cylinder and dome, and to point C on the top of the dome. Since usually the dome part of the insert is in contact with rock during in-service loading and the cylindrical part of the insert is in contact with the holder (and accordingly under pressure loading), path 1 is very important in case of stress analysis. Since the normal stress on this path is zero, or close to zero in the ANSYS modeling, the tangential stress on this path is studied here. Path 2 is located at the intersection of the cylindrical part and the dome part. Path 3 is defined as the midline of the dome (45 degree) in order to get some information about the magnitude and distribution of the residual stress in the dome part. Similar to path 2, the perpendicular stress to the gradient direction is significant along this path; therefore, the circumferential stress is studied on this path. The distribution of tangential stress, σ_L, all over the volume is shown in Figure 4.26. Over the homogeneous substrate the stress is mostly in tension and reaches to its maximum value, only 36 MPa, at the intersection of the homogeneous substrate and graded region. At the surface, compressive stress is recognized with the maximum value of -472 MPa.

The distribution of radial stress, σ_R, all over the volume is shown in Figure 4.27. Over the outer surface, radial stress is zero due to the boundary condition for free surface. Radial stress is smaller and less significant than the longitudinal stress since the material property mismatch is only in the radius direction. This affects the longitudinal stress directly but the radial stress laterally.

4.3.1 Effect of Cobalt Gradient Profile on Residual Stresses

Tangential stress at the outer surface and as a function of its position from the cylinder base along path 1, is demonstrated in Figure 4.28 for different profiles of Co gradient. Different profiles of Co variations are represented by *N* exponent. Similar to the discussion in the cylinder section, tangential stress component at the outer FGM surface of the FG-WC-Co dome-top insert, where the Co value is lower at the surface than its value in depth, is a compressive stress. The magnitude of this compressive stress arises as the profile exponent, *N*, decreases. As presented, stress distribution for *N* values of 0.2, 0.5, 1, 2 and 5 are considered.

The maximum tangential stress along path 1, σ_{t_S}, belongs to the Co profile represented by *N*=0.2 and is around -700MPa. This large value of compressive stress is induced due to only 6% difference in Co content value between surface and inside of the insert. It should be mentioned that compressive stress at the surface is very desirable for cutting inserts applied in oil and gas drilling industry. The compressive stress at the outer surface of the insert is constant all over the dome surface as well as a considerable part of the cylinder. The rate of change in the magnitude of the maximum compressive stress between the two sequence values of *N* is much higher for the smaller *N* values (N<1) than the larger values of *N* (*N*=1, 2 and 5). *N*<1 represents the convex profile of Co gradient while *N*=1 denotes the linear variation of Co and *N*>1 stands for the concave shape of Co profile. Figure 4.29 shows the longitudinal stress along path 2 for different Co profiles, *N* values of 0.2, 0.5, 1, 2 and 5. The ratio of gradient thickness over total radius is constant, *H/R*=1/3. As a general trend, stress possesses a small value around the insert axis. Stress will increase while moving from core to the interface of the homogeneous region and the

FGM region. In the homogeneous region, for all the N values, stress has an increasing tensile trend. It reaches its maximum value at the interface, where the homogeneous region ends. This variation is relatively linear and the variation slope of this increasing trend is directly related to the magnitude of N. Therefore, the maximum variation slope and the maximum value of tensile stress at the surface belongs to the N of 5 and vise versa the minimum tensile stress is referred to the N of 0.2. From the fatigue point of view, tensile stress inside the material is not desired, therefore it is an aim to determine the optimum gradient profile in order to postpone the component fracture and increase the life-length of a product. The same discussion that we had for the longitudinal stress along path 2 is also valid for the circumferential stress along path 3, (Figure 4.30).

Another stress component on the surface is the radial stress, σ_{R_S}, which is perpendicular to the surface and therefore, due to the free surface condition, is zero all along the surface of the FGM cylinder. As illustrated in the cylinder section, even along path 2, radial stress, σ_{Rc}, is very small compared to the longitudinal stress. Therefore, in this section, discussion about radial stress is ignored.

4.3.2 Effect of Cobalt Gradient Thickness on Residual Stresses

Different profiles of Co gradient based on different values of gradient thicknesses, shown in Figure 4.19, study the residual stress distribution. Co composition varies from the greater value of 16 wt. % in the substrate and at the interface to the smaller value of 10 wt. % at the surface.

Tangential stress at the outer surface and as a function of its position from the cylinder base, along path 1, is demonstrated in Figure 4.31 for different Co normalized

gradient thicknesses, *H/R*, Figure 4.19. As seen from Figure 4.31, tangential stress component at the outer FGM surface of the FG-WC-Co cylinder, where Co value is lower at the surface than its value in depth, is a compressive stress. The magnitude of the compressive stress decreases as the gradient thickness, *H*, decreases. As presented, stress distribution for *H/R* values of 1/30, 1/15, 1/3 and 1/2, are considered. The maximum tangential stress at the outer surface, σ_{L_S}, belongs to the Co profile represented by *H/R*=1/30 (0.03333) and is around -470 MPa. This value of compressive stress is induced due to only 6% difference in Co content value between the surface and inside of the cylinder.

Figures 4.32 and 4.33 show the longitudinal stress and circumferential stress along path 2 and path 3, for different normalized gradient thicknesses, *H/R*, while the Co gradient exponent, *N*, is constant, *N*=1. General trend for all gradient thicknesses are the same. As discussed before, through-the-thickness longitudinal stress, starts from a tensile stress at the cylinder axis, which is then linearly increased to its maximum positive value of 100 MPa at the interface. Afterwards, in the graded region, a reverse trend is observed and stress decreases from the peak value to the compressive stress at the FGM surface. The initial value of stress on the axis of the cylinder, the compressive stress at the surface as well as the stress variation slopes in both homogeneous and FGM regions are highly affected by the gradient thickness value.

As illustrated, the smaller the gradient thickness is, then both of the surface compressive stress and the axial tensile stress are larger. This results in smoother slopes for larger values of normalized gradient thicknesses, *H/R*. Interestingly and despite the significant affect of gradient thickness on the stress distribution, the stress value at the

interface, which is a tensile stress, does not vary that much by changing the gradient thickness.

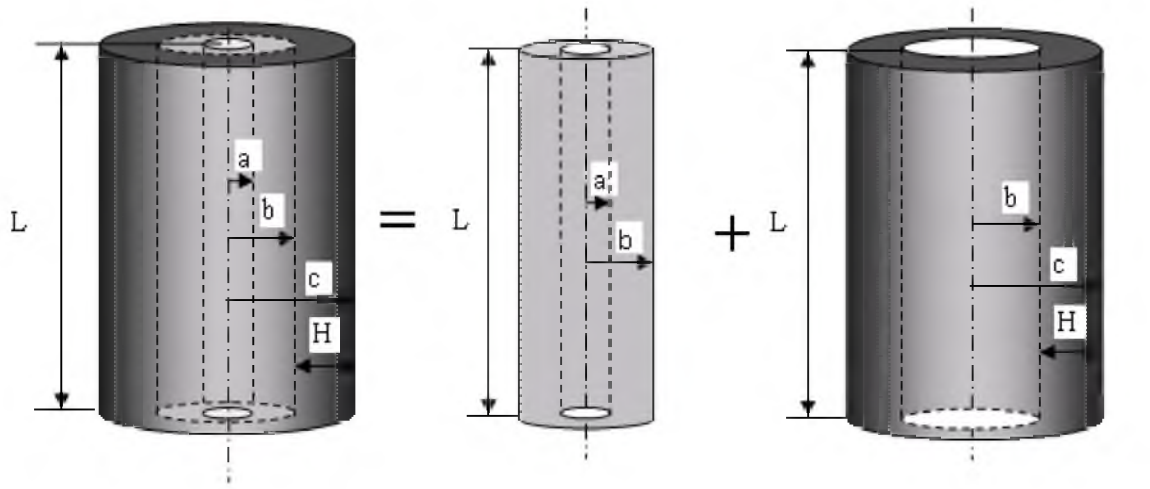

Figure 4.1 A long cylindrical component (shown at far left) as a construct of two elements: a hollow homogeneous cylinder with inner radius, a, and outer radius, b (center), and a hollow FGM cylinder with inner radius, b, and outer radius, c (far right).

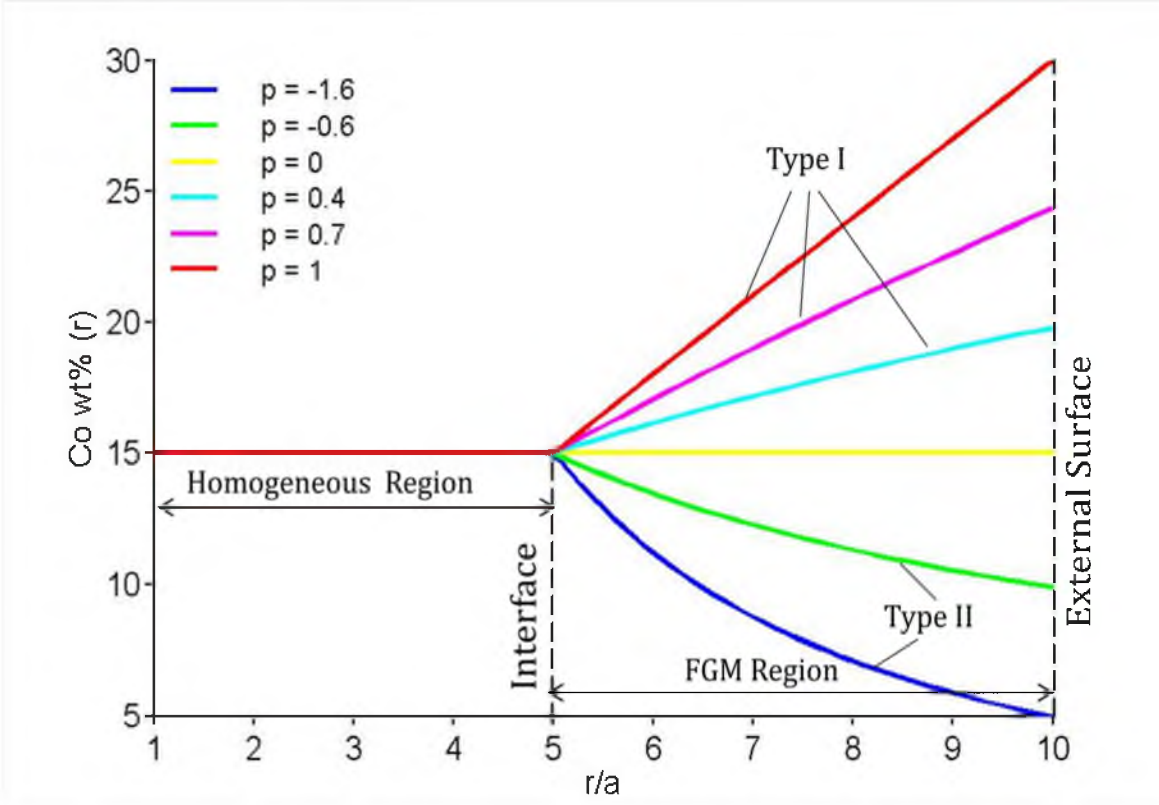

Figure 4.2 Co content gradient in WC-Co compound cylinder represented by power law index, p, where, $w(r) = w_0 r^p$, in which $w\ (r)$ is the weight fraction of Co as a function of the radius. The inner radius is assumed as a=1 mm, the interface of homogeneous and FGM regions radius is considered as b=5 mm and the outer radius is c=10 mm. E_a=550 *(GPa)*, α_a=6.6x10^{-6} /ºC [127] (these variables may be assumed for all remaining figures, except where noted otherwise).

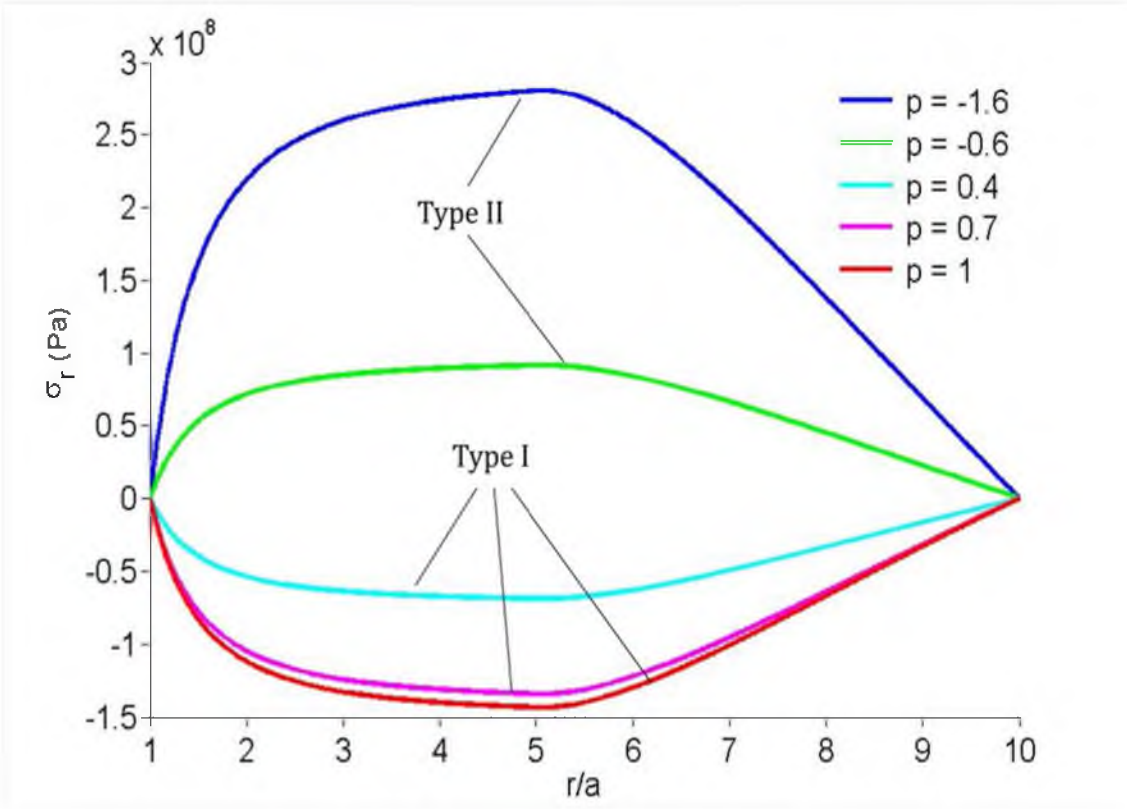

Figure 4.3 Radial stress distribution in WC-Co compound cylinder as a function of the radius for different gradient profiles, represented by power law index, *p*.

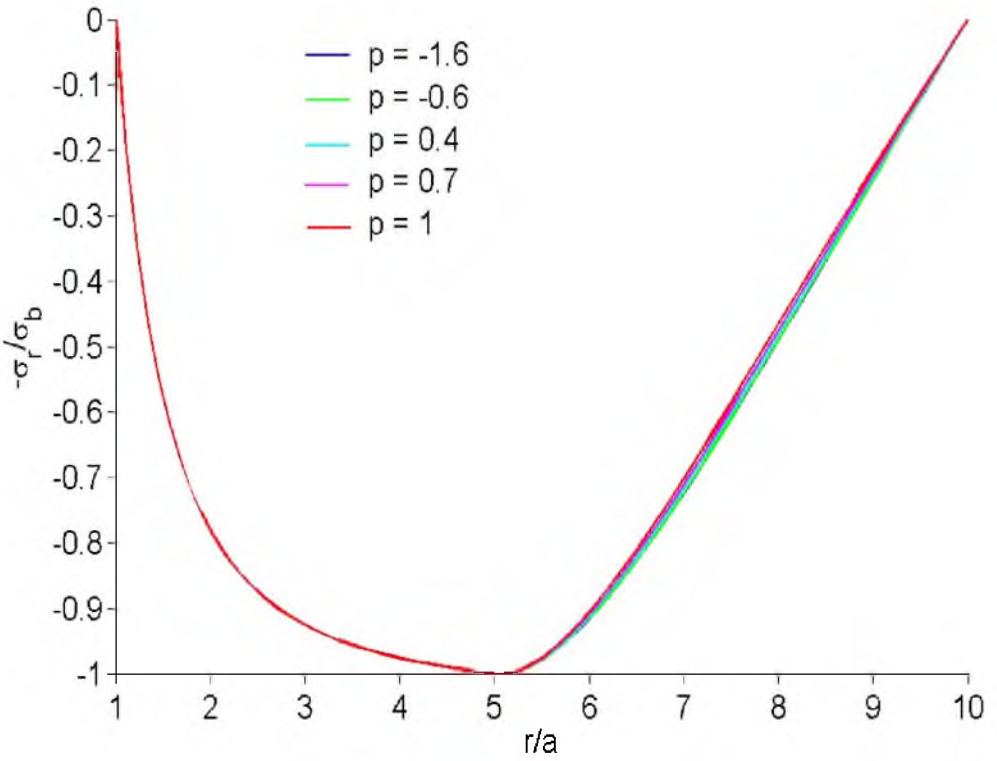

Figure 4.4 Normalized radial stress distribution in WC-Co compound cylinder as a function of the radius for different gradient profiles, represented by power law index, *p*.

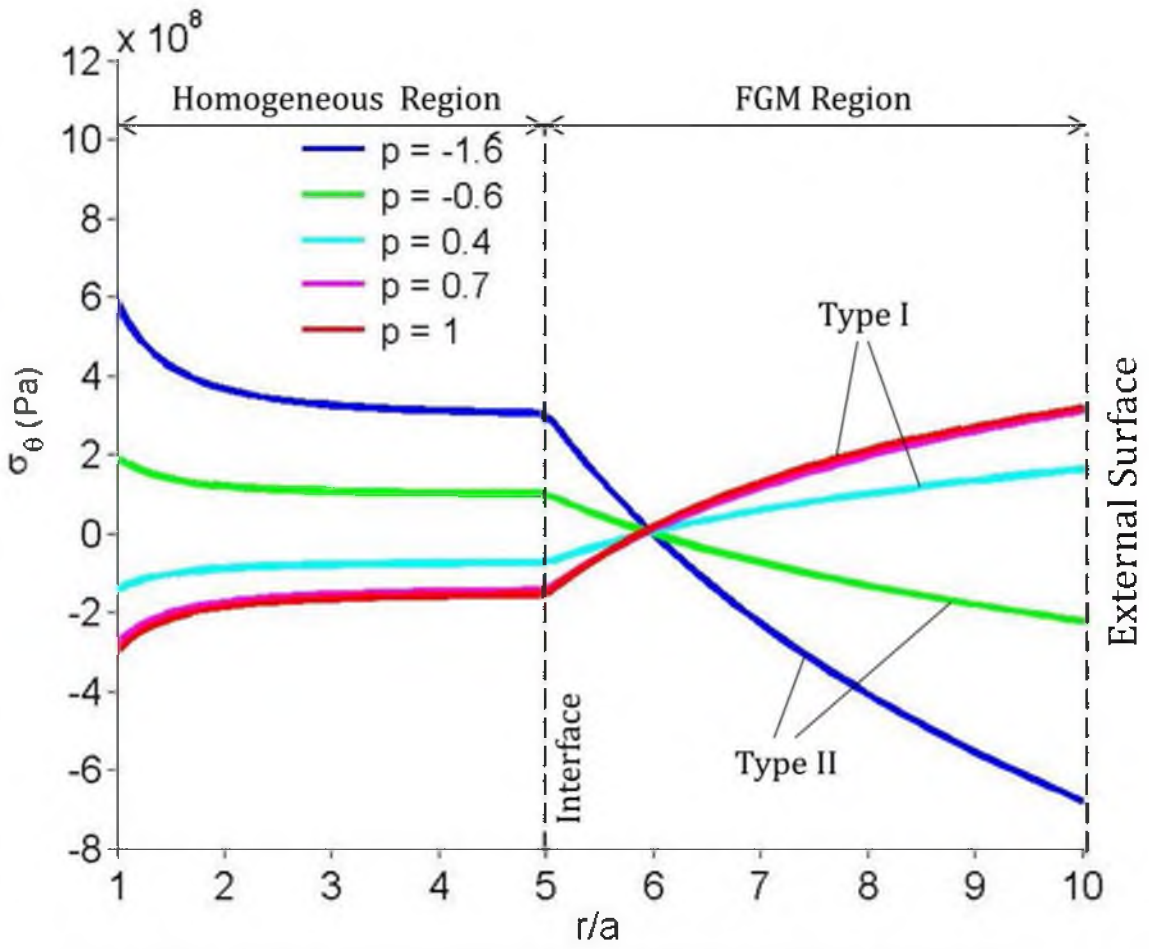

Figure 4.5 Hoop stress distribution in WC-Co compound cylinder as a function of the radius for different gradient profiles, represented by power law index, *p*.

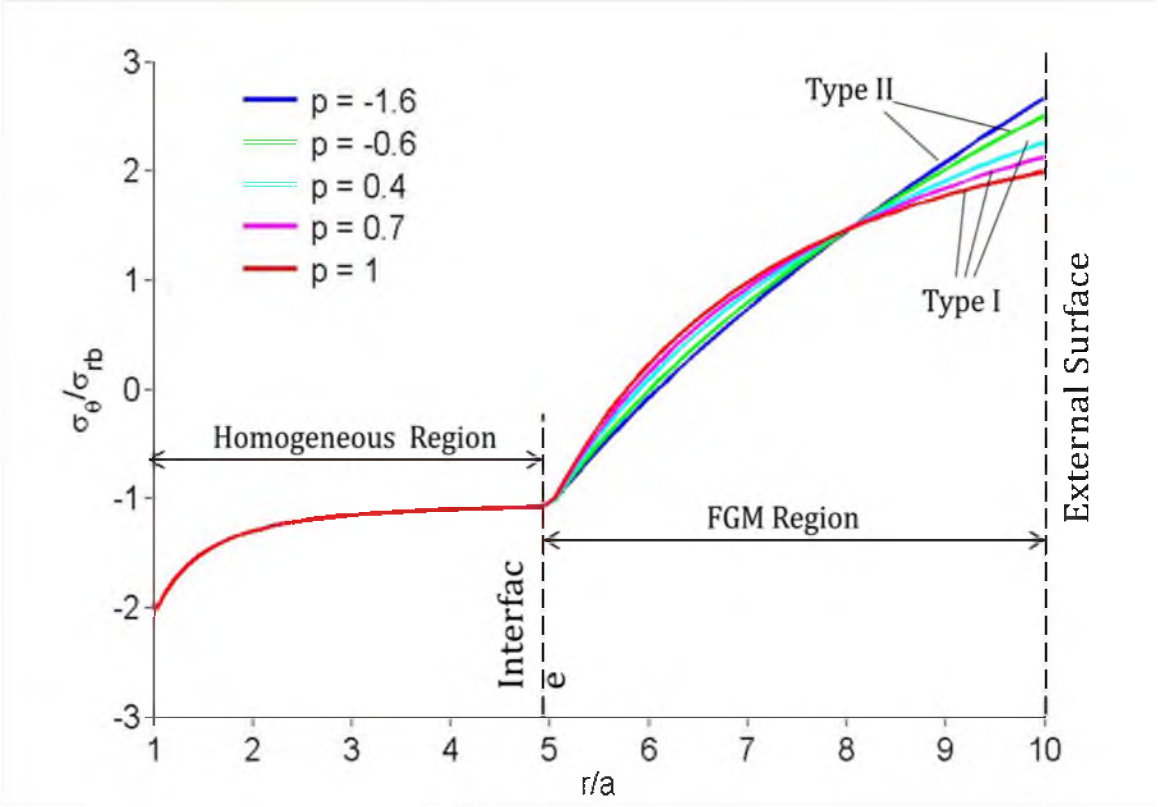

Figure 4.6 Normalized hoop stress distribution in WC-Co compound cylinder as a function of the radius for different gradient profiles, represented by power law index, *p*.

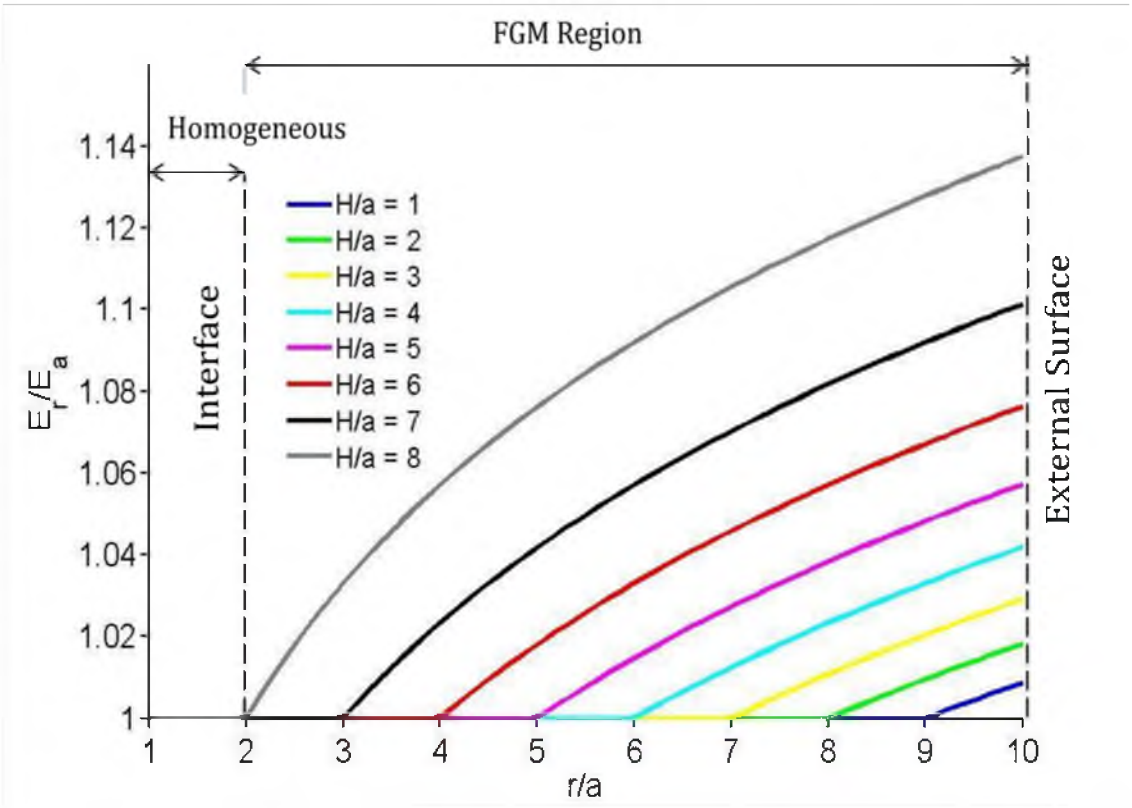

Figure 4.7 Variation of elastic modulus in WC-Co compound cylinder as a function of the radius for different gradient thicknesses, represented by *H/a*, with gradient power index p = -0.6, where, $w(r) = w_0 r^p$ in which *w(r)* is the weight fraction of Co as a function of the radius.

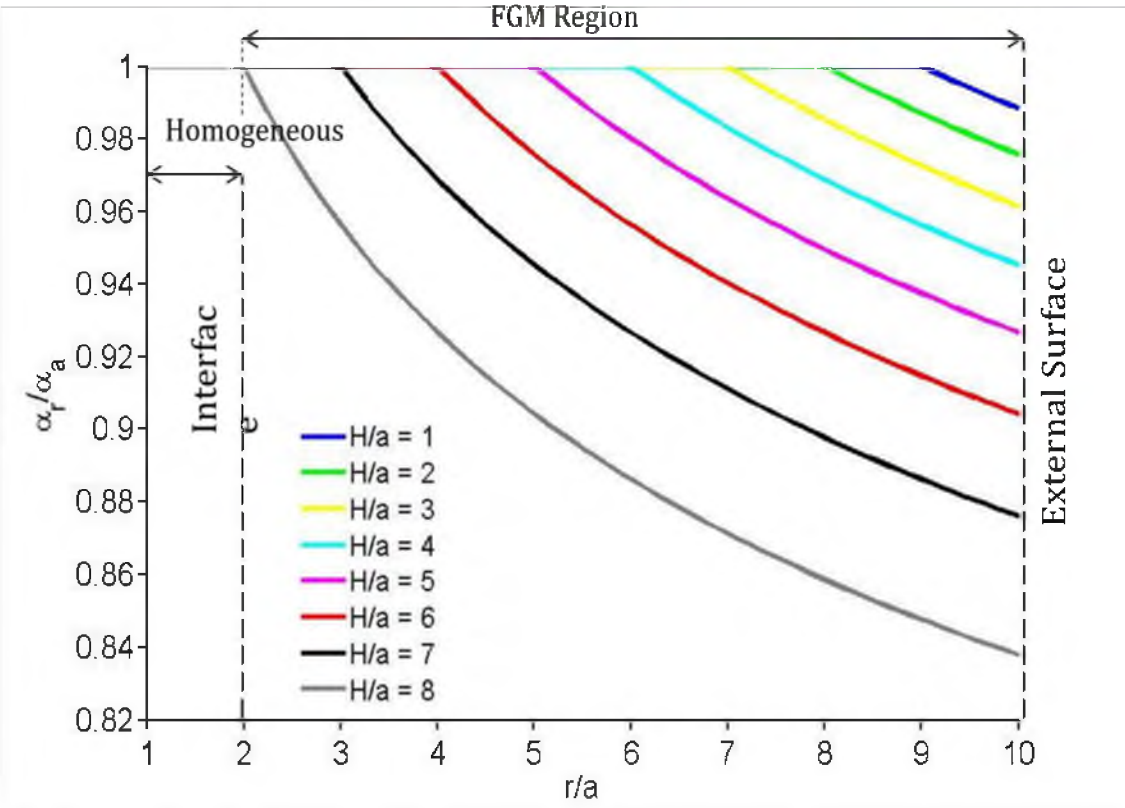

Figure 4.8 Variation of coefficient of thermal expansion in WC-Co compound cylinder as a function of the radius for different gradient thicknesses, represented by H/a, with gradient power index p = -0.6.

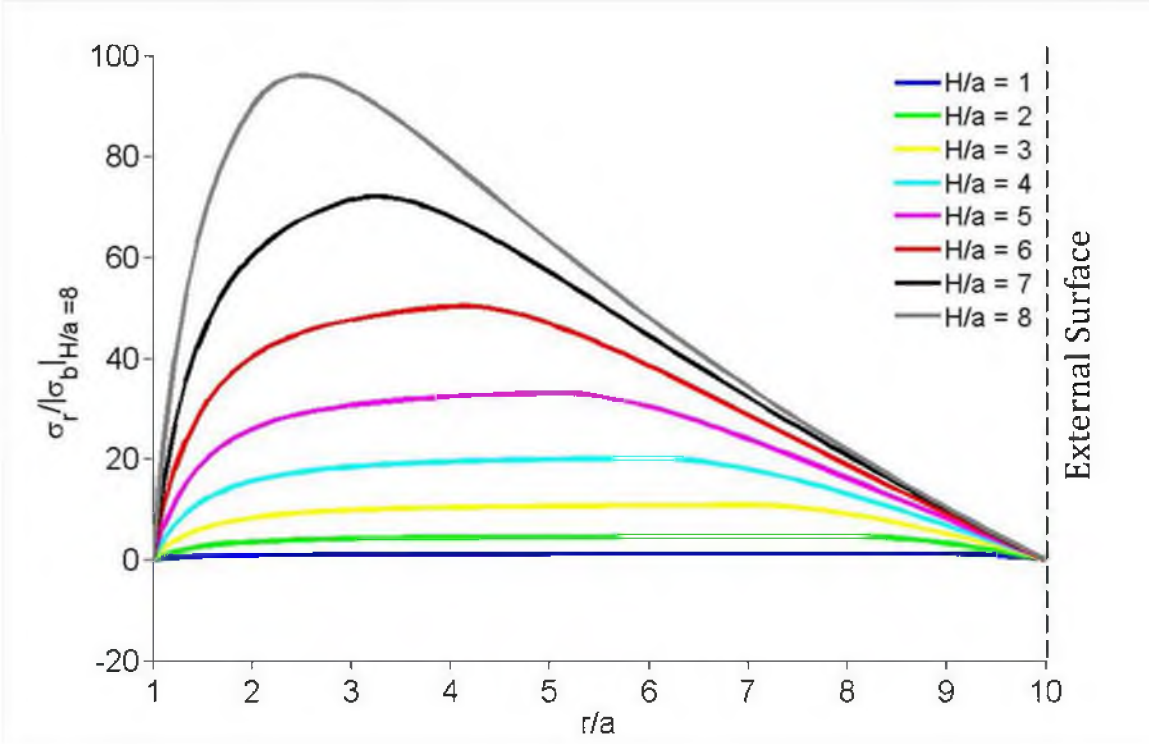

Figure 4.9 Distribution of normalized radial stress in WC-Co compound cylinder as a function of the radius for different gradient thicknesses, represented by H/a, with gradient power index p=-0.6.

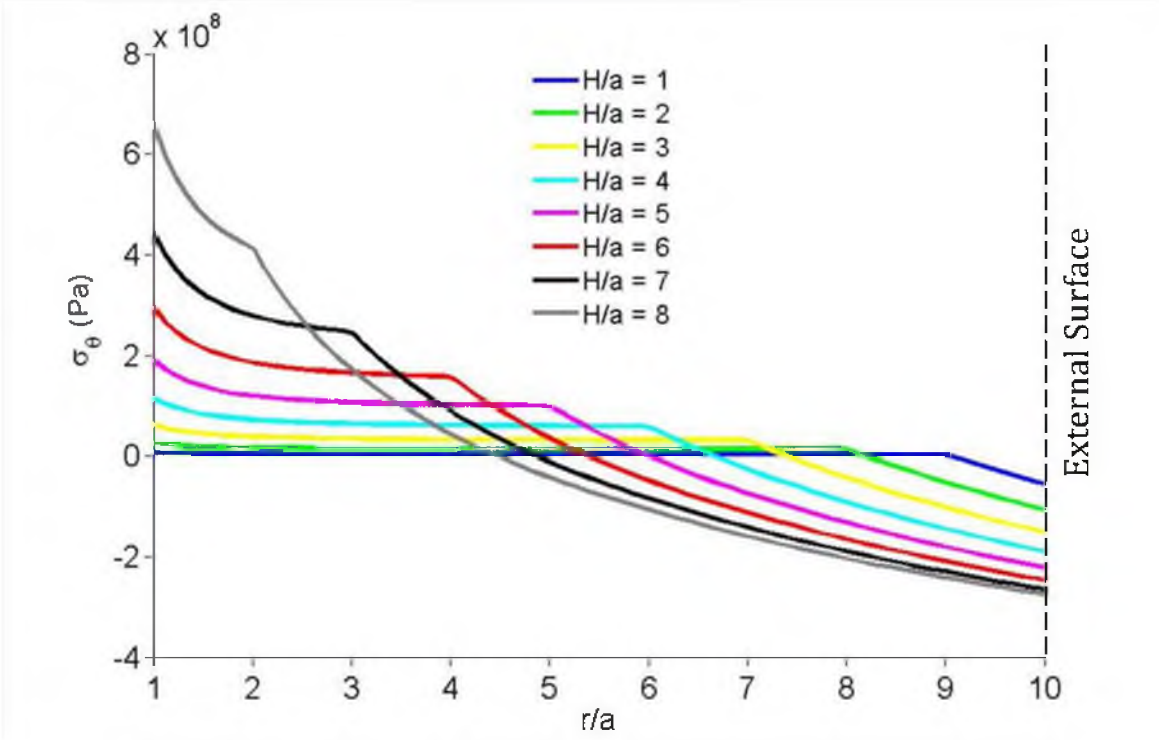

Figure 4.10 Distribution of hoop stress in WC-Co compound cylinder as a function of the radius for different gradient thicknesses, represented by *H/a*, with gradient power index p = -0.6.

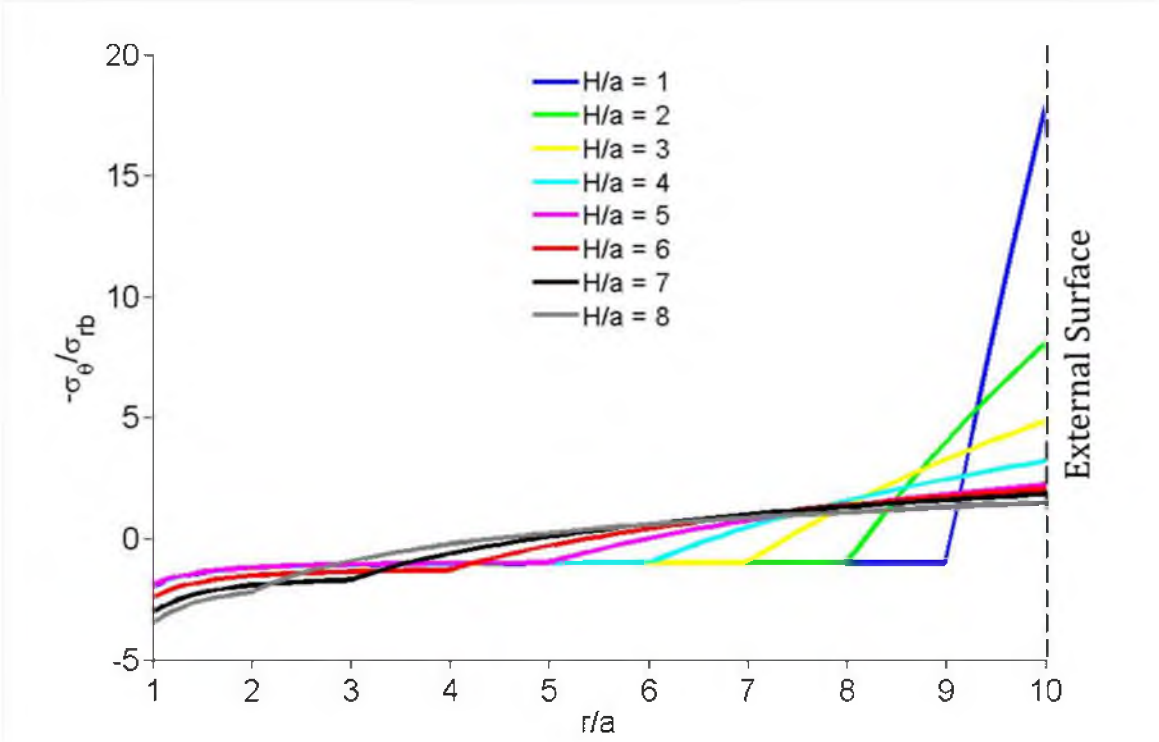

Figure 4.11 Distribution of normalized hoop stress in WC-Co compound cylinder as a function of the radius for different gradient thicknesses, represented by H/a, with gradient power index p = -0.6.

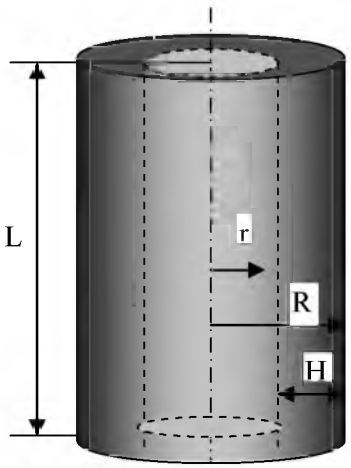

Figure 4.12 Schematic of FG-WC-Co cylindrical compound with length of *L*, total radius of *R* and gradient thickness of *H*

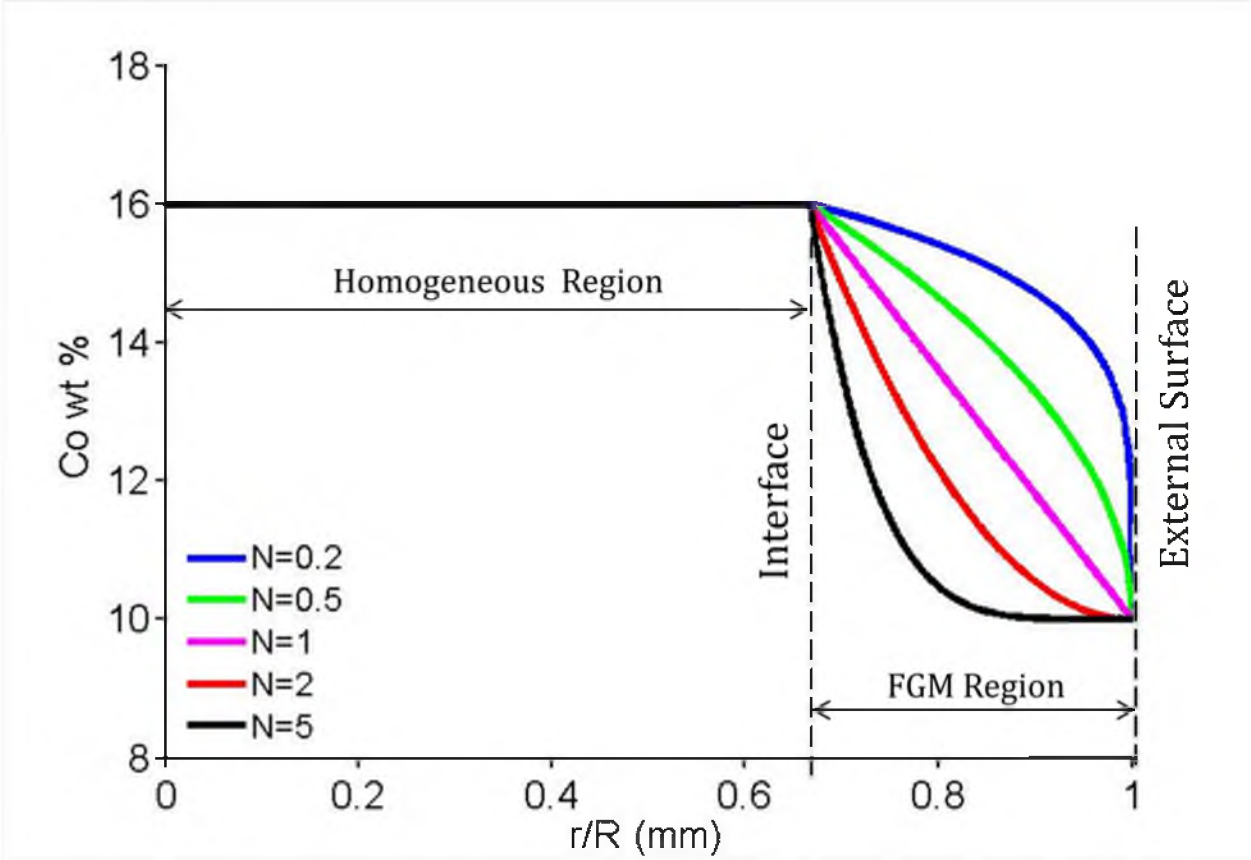

Figure 4.13 Co content gradient in WC-Co compound cylinder represented by power law index, N, where, $V_C(r) = (V_{C1} - V_{C2})\left(\frac{R-r}{H}\right)^N + V_{C2}, for\ R - H \leq r \leq R$, in which $V_C\ (r)$ is the volume fraction of Co as a function of the radius. E_{homo}=540 (GPa), α_{homo}=6.8x10-6 /°C [127], H/R=1/3.

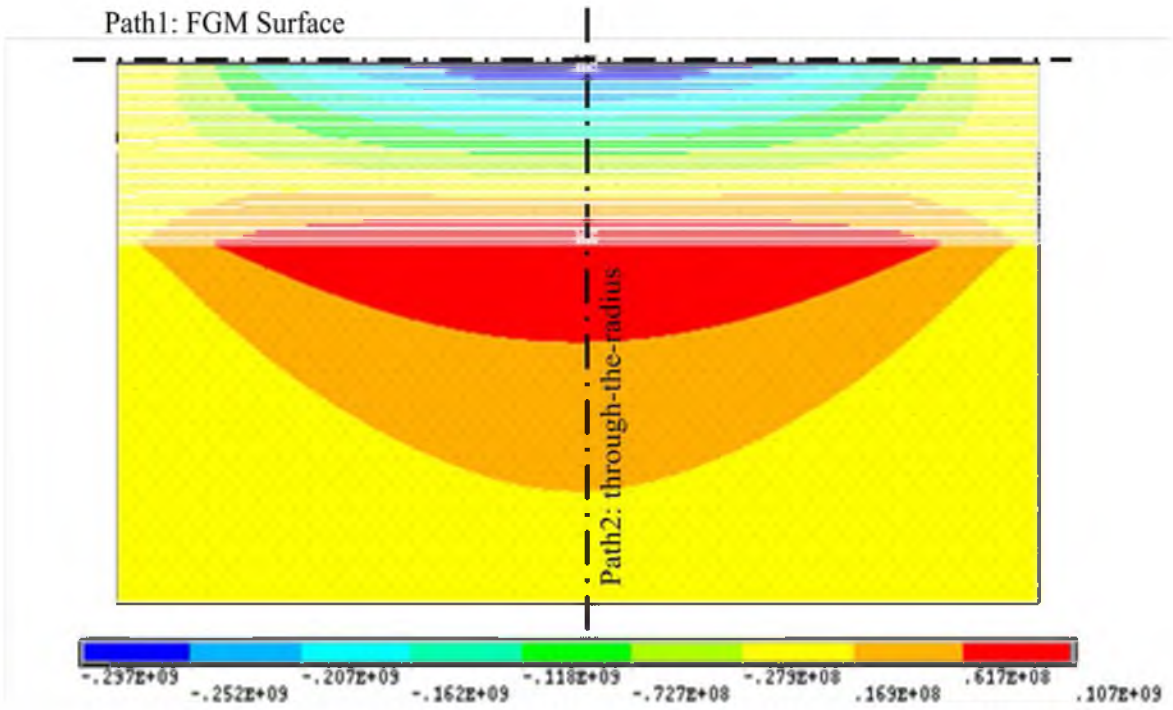

Figure 4.14 Longitudinal stress distribution in a cylinder with, N=1, H=1 and R=3.

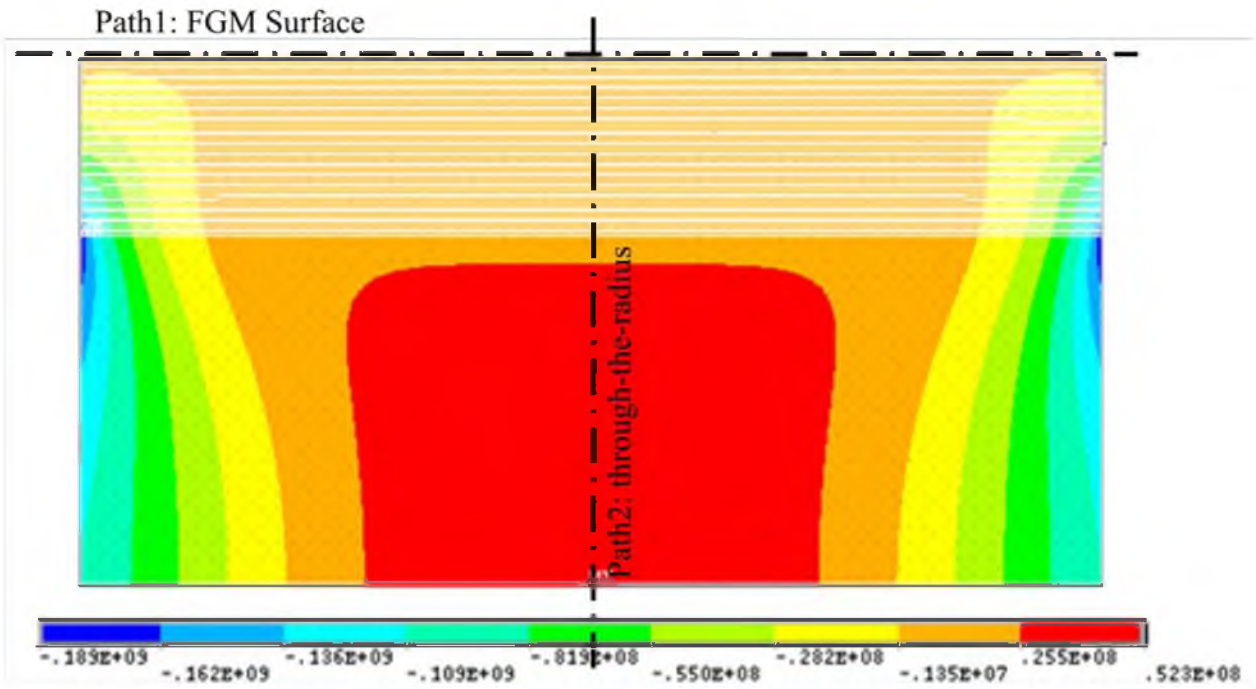

Figure 4.15 Radial stress distribution in a cylinder with, N=1, H=1 and R=3.

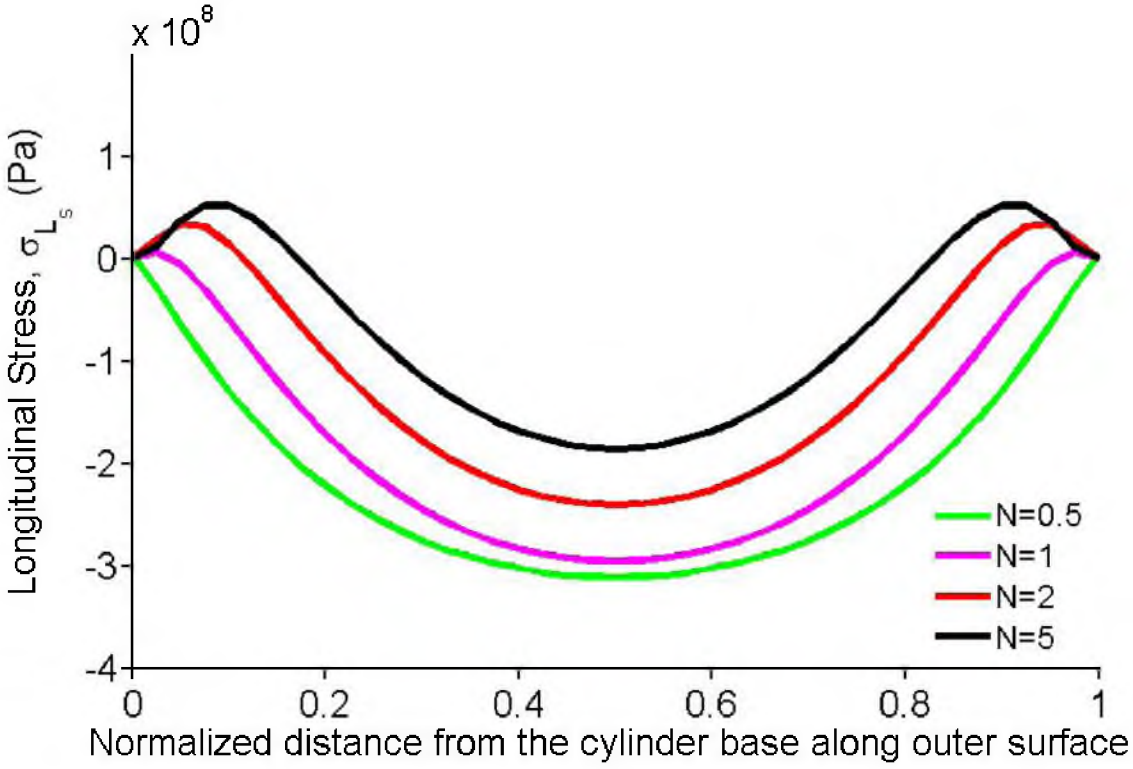

Figure 4.16 Longitudinal stress, σ_{L_S}, at the outer surface and along path 1 as a function of normalized distance from the cylinder base for different gradient profiles, where H/R=1/3.

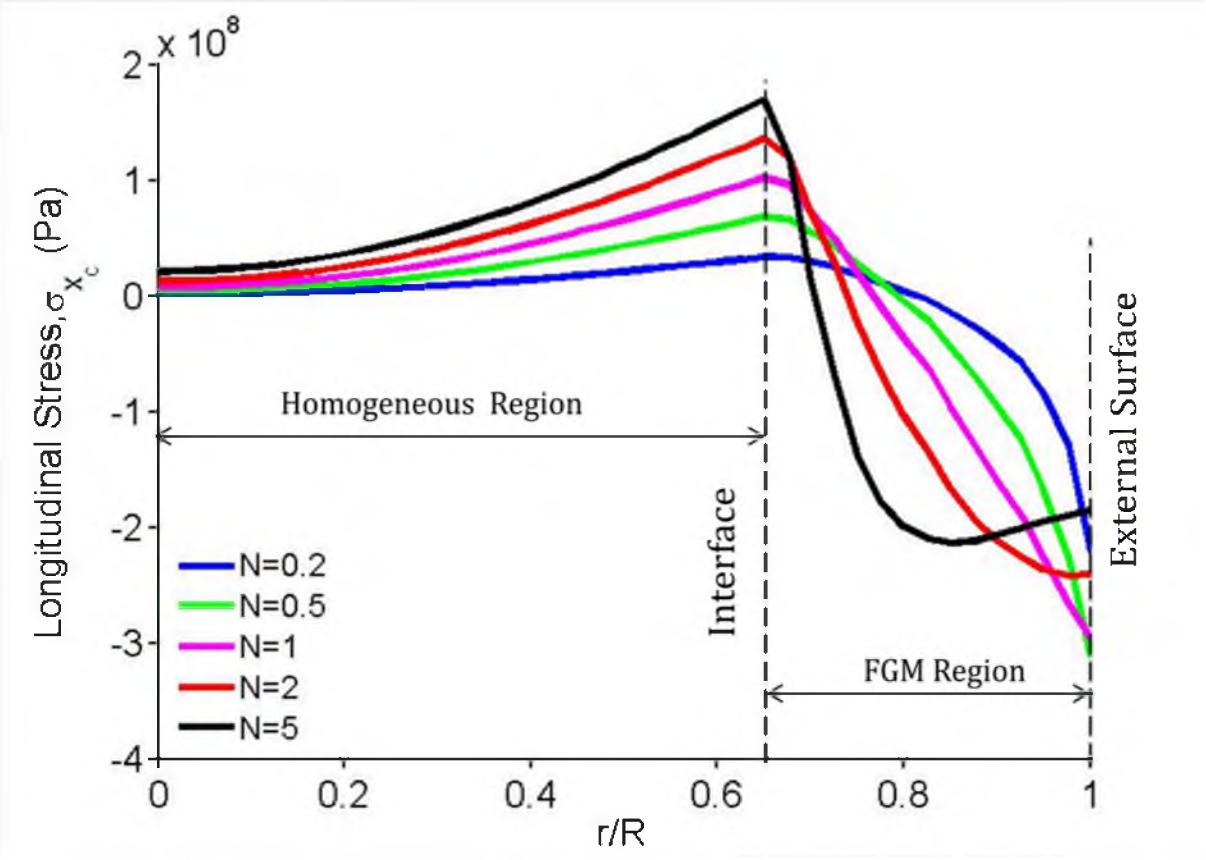

Figure 4.17 Through-the-radius longitudinal stress, σ_{L_C}, along path 2 as a function of normalized radius for different gradient profiles, where H/R=1/3.

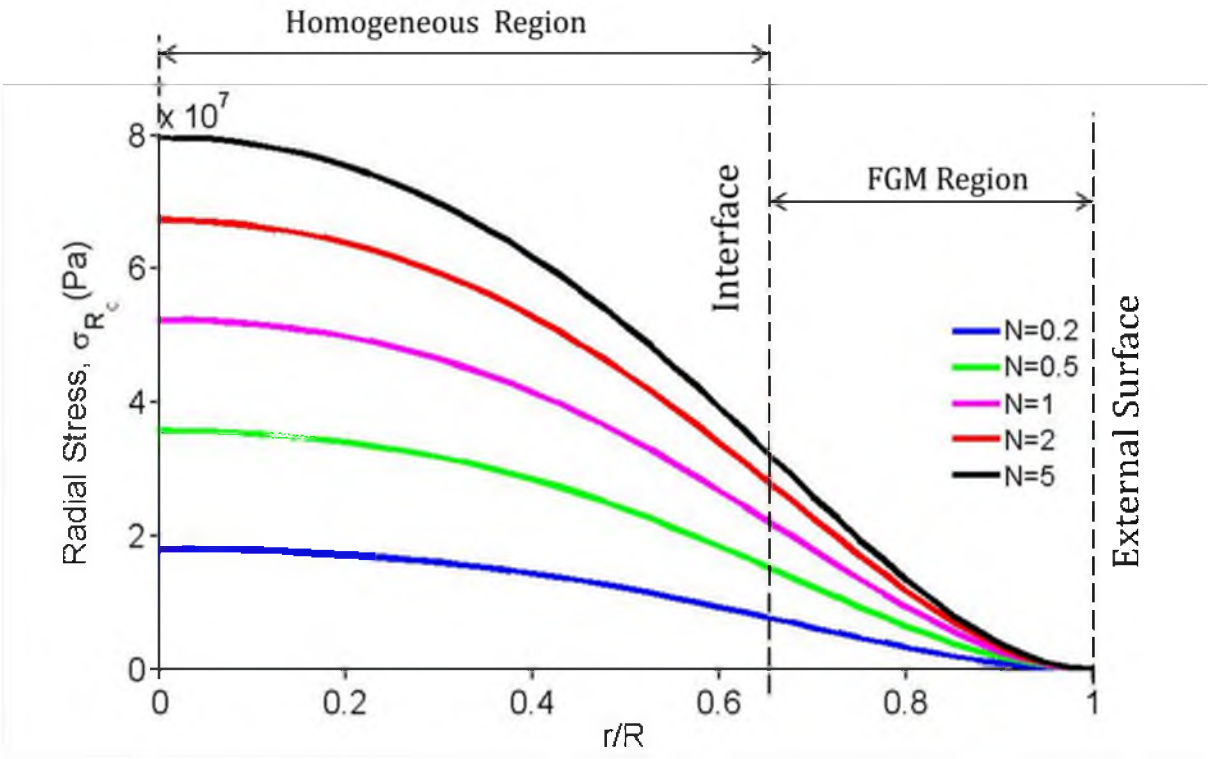

Figure 4.18 Through-the-thickness radial stress, σ_{R_C}, along path 2 as a function of normalized radius for different gradient profiles, where H/R=1/3.

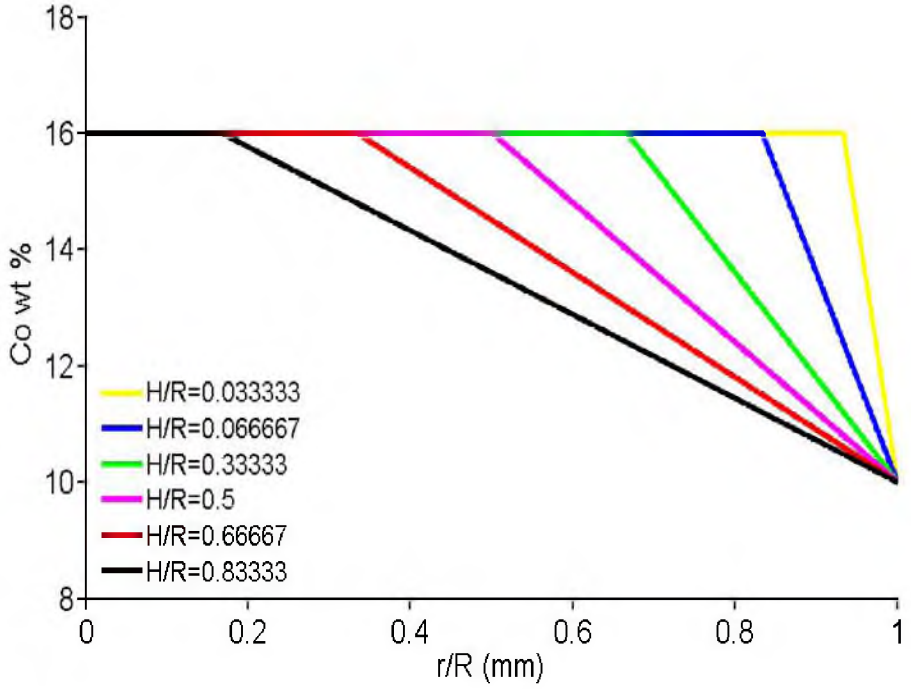

Figure 4.19 Co content gradient in WC-Co compound cylinder for different normalized gradient thickness, *H/R*, E_{homo}=540 *(GPa)*, α_{homo}=6.8x10-6 /ºC [127], *N*=1.

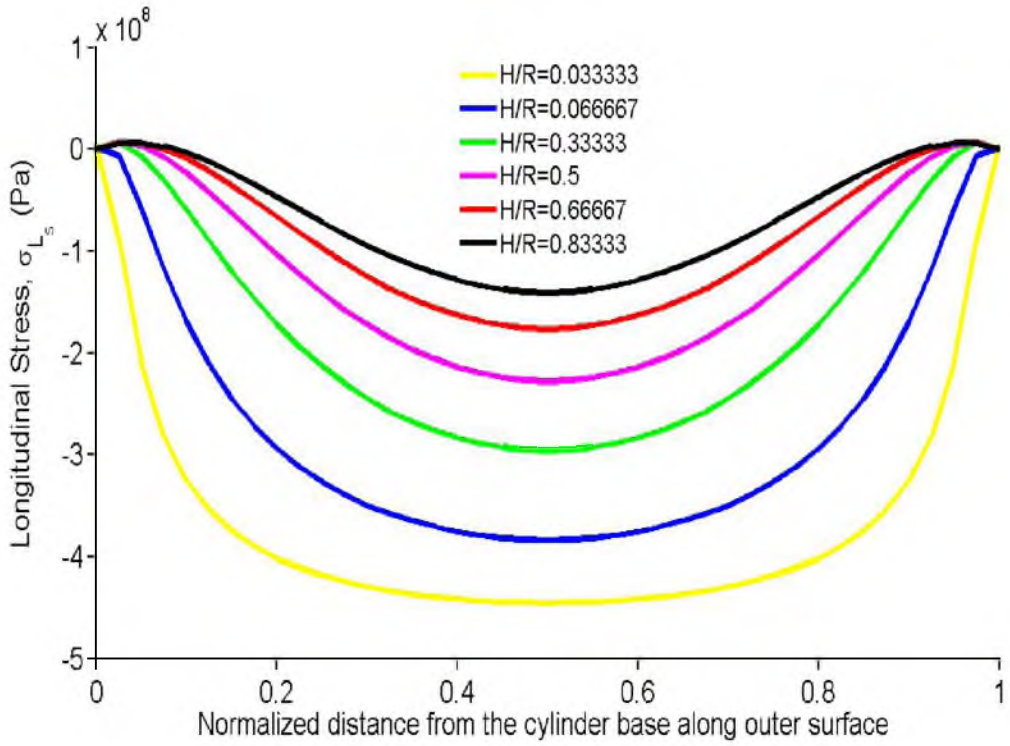

Figure 4.20 Longitudinal stress, σ_{L_S}, at the outer surface along path 1 as a function of normalized distance from the cylinder base for different normalized gradient thicknesses, where N=1.

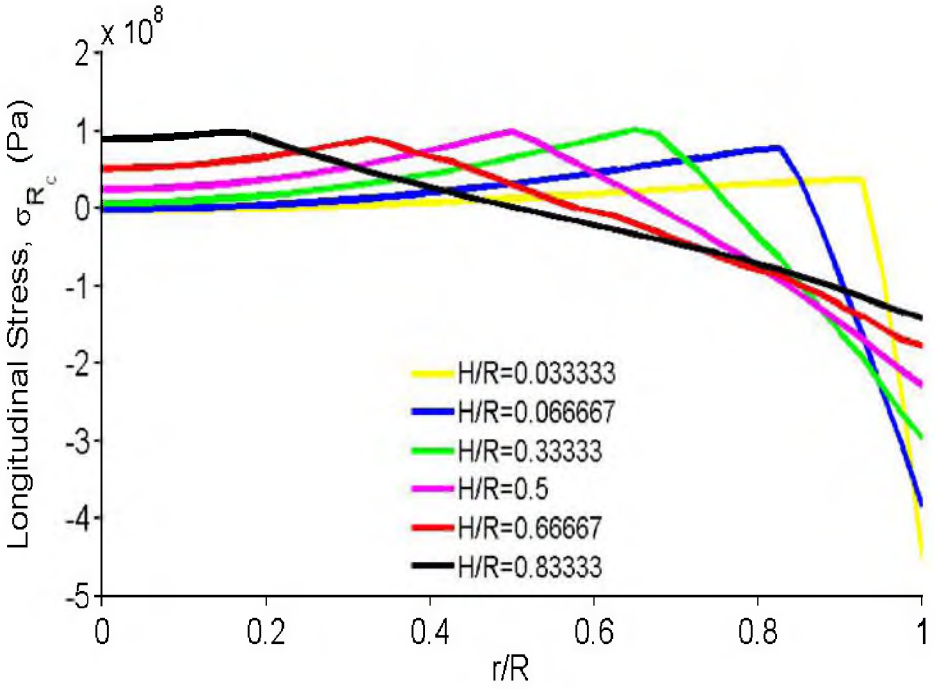

Figure 4.21 Through-the-thickness longitudinal stress, σ_{L_C}, along path 2 as a function of normalized radius for different normalized gradient thicknesses, where N=1.

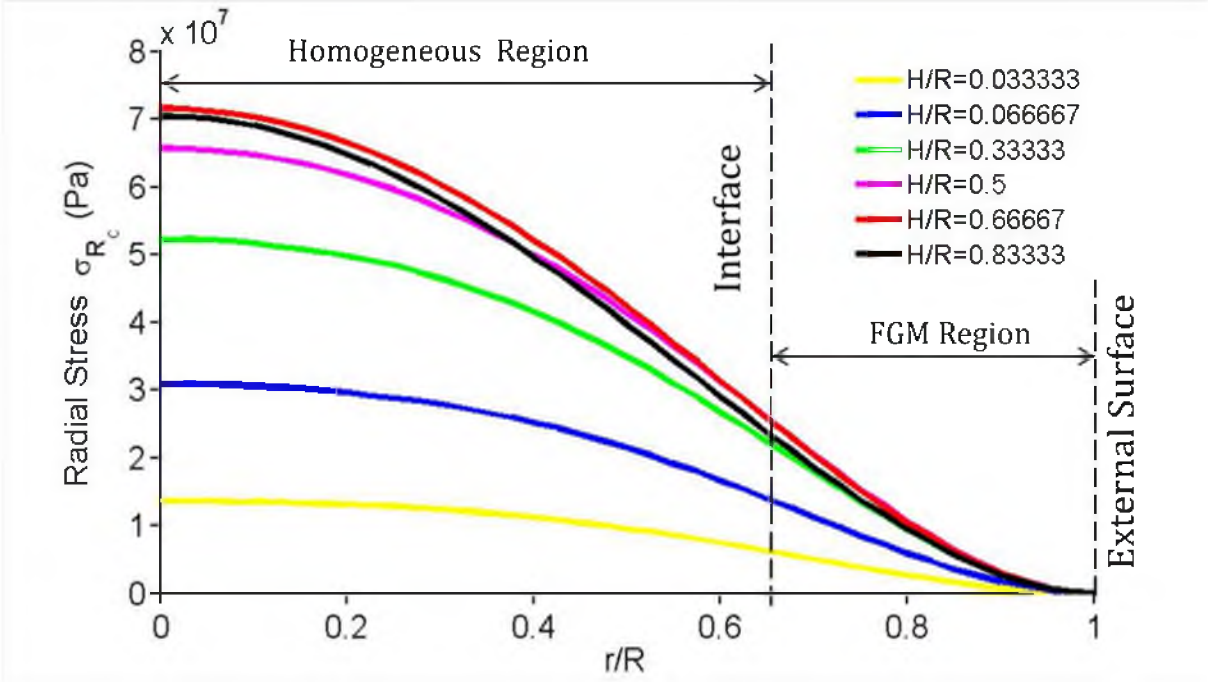

Figure 4.22 Through-the-thickness radial stress, σ_{R_C}, along path 2 as a function of normalized radius for different gradient profiles for different normalized gradient thicknesses, where N=1.

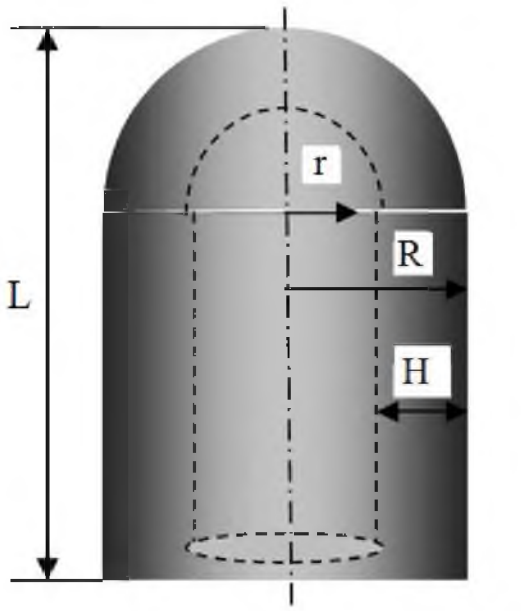

Figure 4.23 Schematic of FG-WC-Co dome-top compound with length of *L*, total radius of *R* and gradient thickness of *H*.

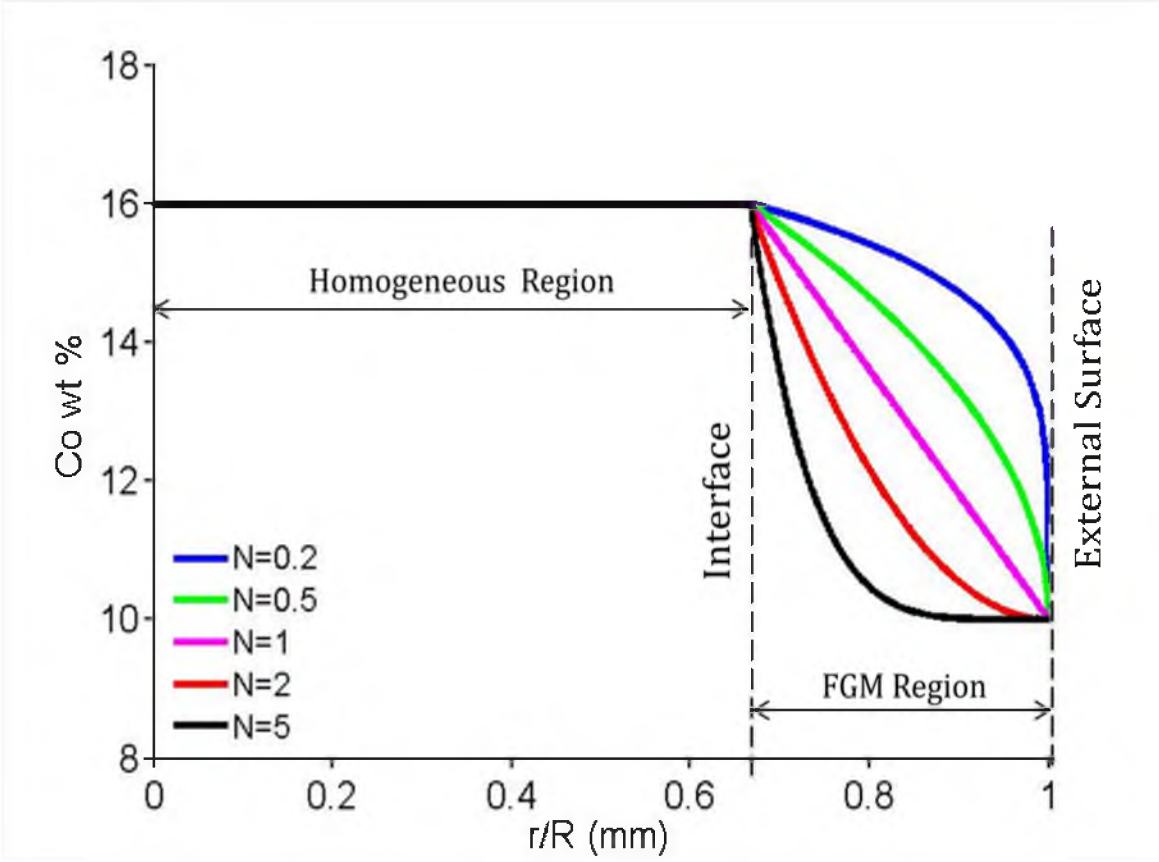

Figure 4.24 Co content gradient in WC-Co compound cylinder represented by power law index, N, where, $V_C(r) = (V_{C1} - V_{C2})\left(\frac{R-r}{H}\right)^N + V_{C2}, for\ R - H \leq r \leq R$, in which $V_C\ (r)$ is the volume fraction of Co as a function of the radius. E_{homo}=540 (GPa), α_{homo}=6.8x10-6 /°C [127], H/R=1/3.

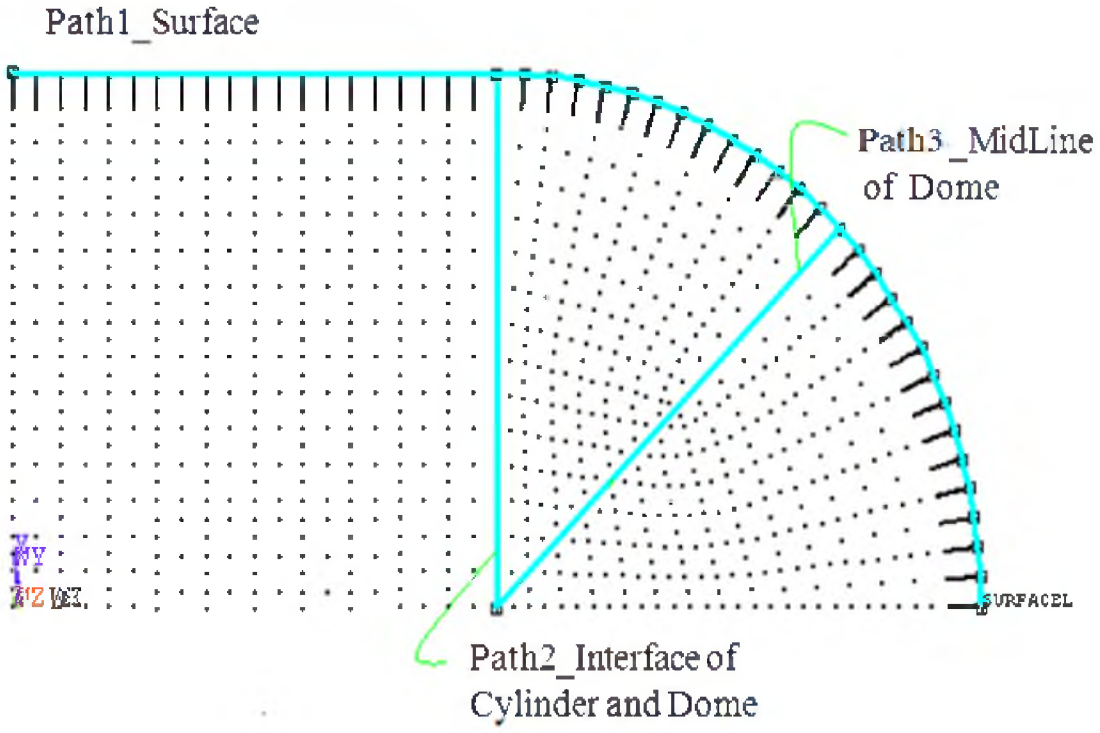

Figure 4.25 Three defined paths on the FG-WC-Co dome-top FEA model.

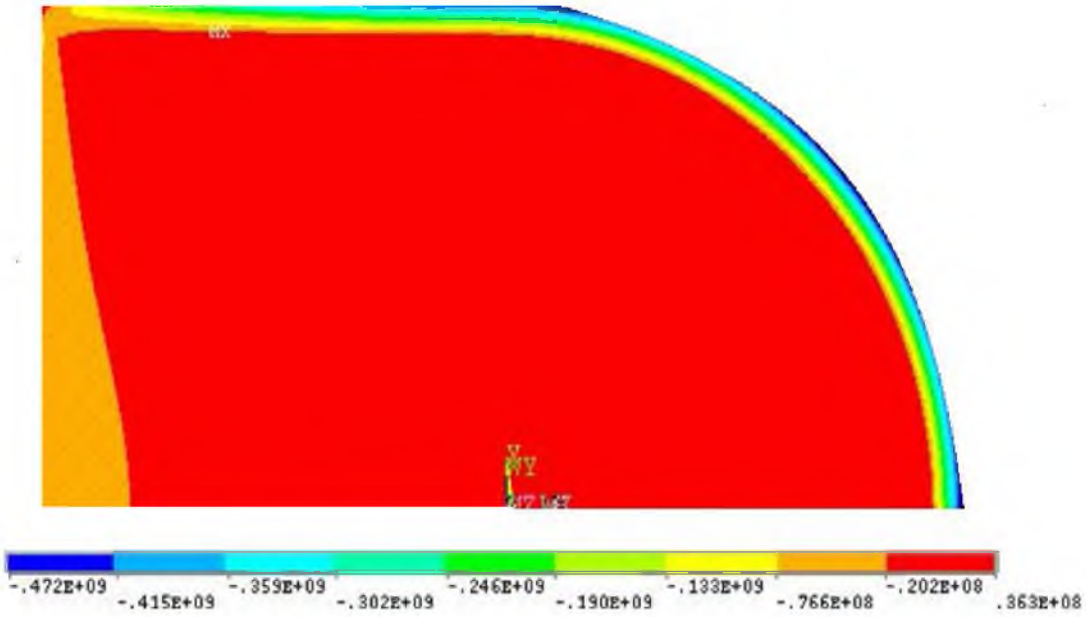

Figure 4.26 Tangential stress distribution of an FG-WC-Co dome-top FEA model with N=1, H/R=1/3.

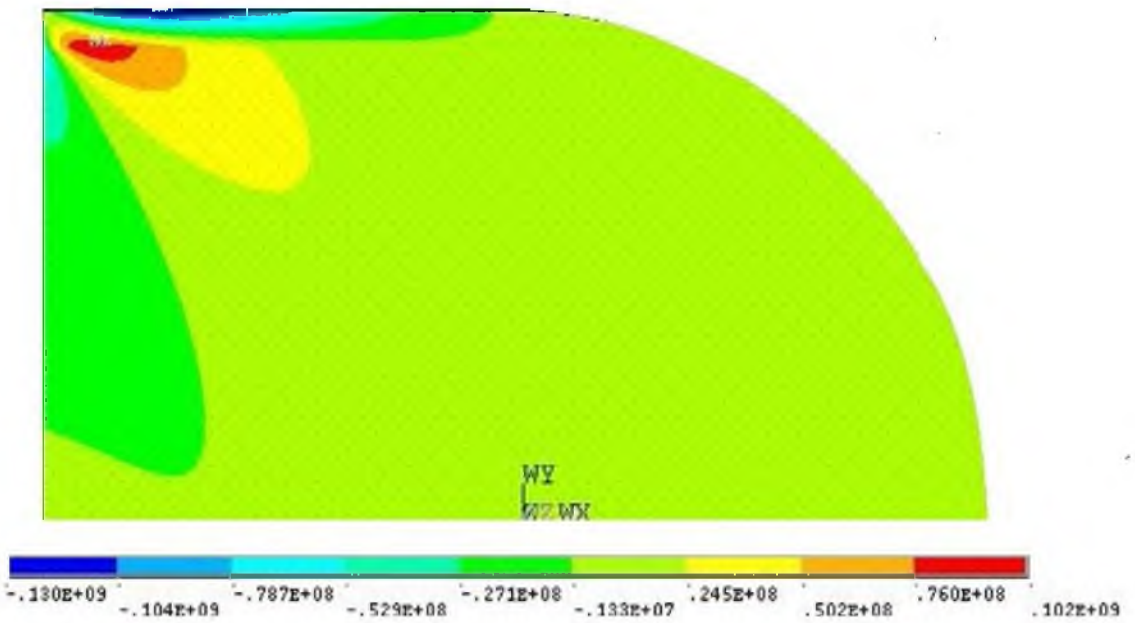

Figure 4.27 Radial stress distribution of an FG-WC-Co dome-top FEA model with N=1, H/R=1/3.

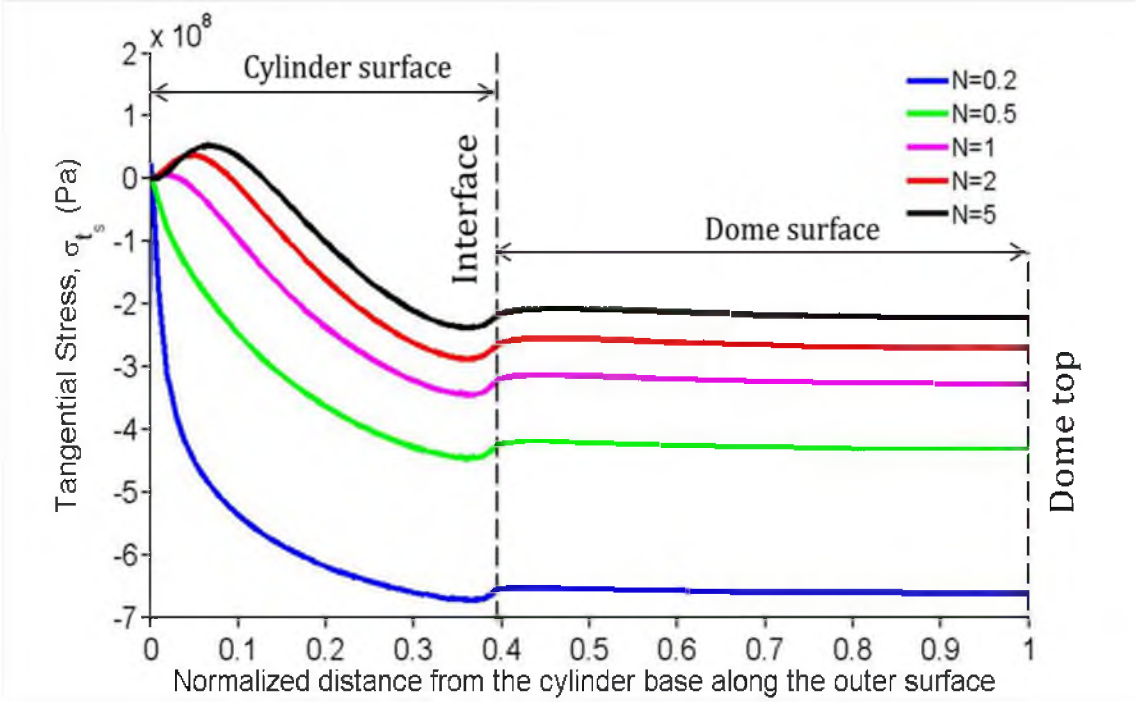

Figure 4.28 Distribution of tangential stress, σ_{t_s}, along the surface, path 1, of dome-top compound as a function of position for different gradient profile, where H/R=1/3.

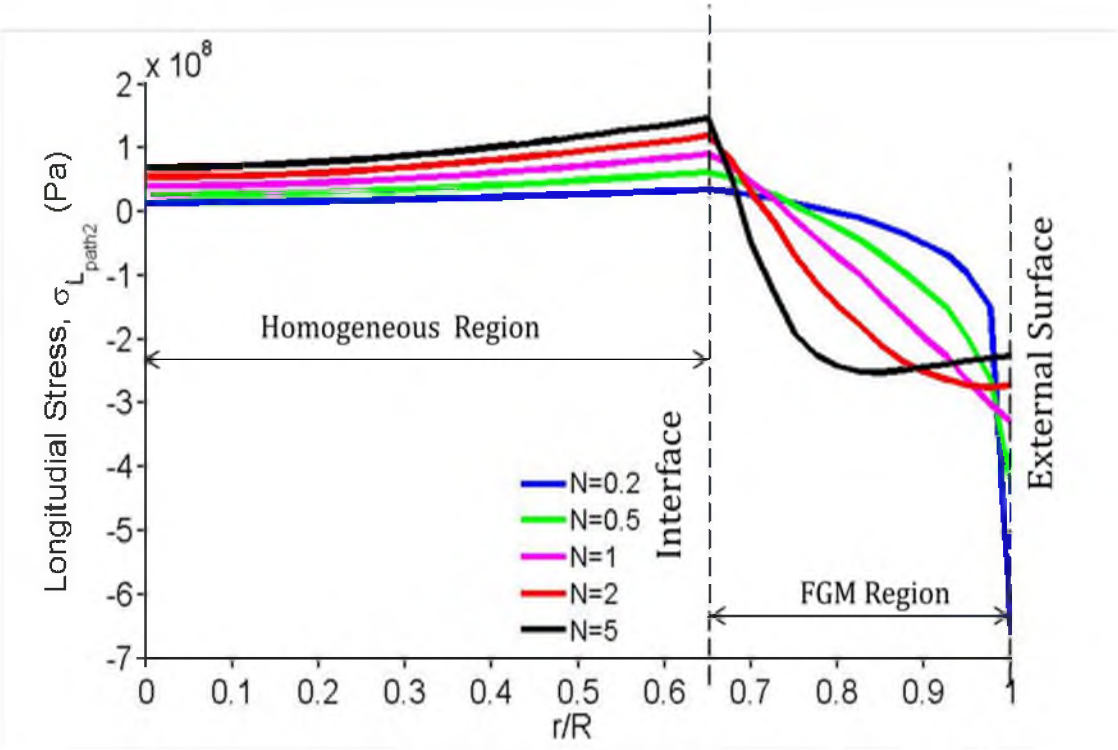

Figure 4.29 Through-the-radius longitudinal stress, σ_{Lpath2}, along path 2 as a function of normalized radius for different gradient profiles, where H/R=1/3.

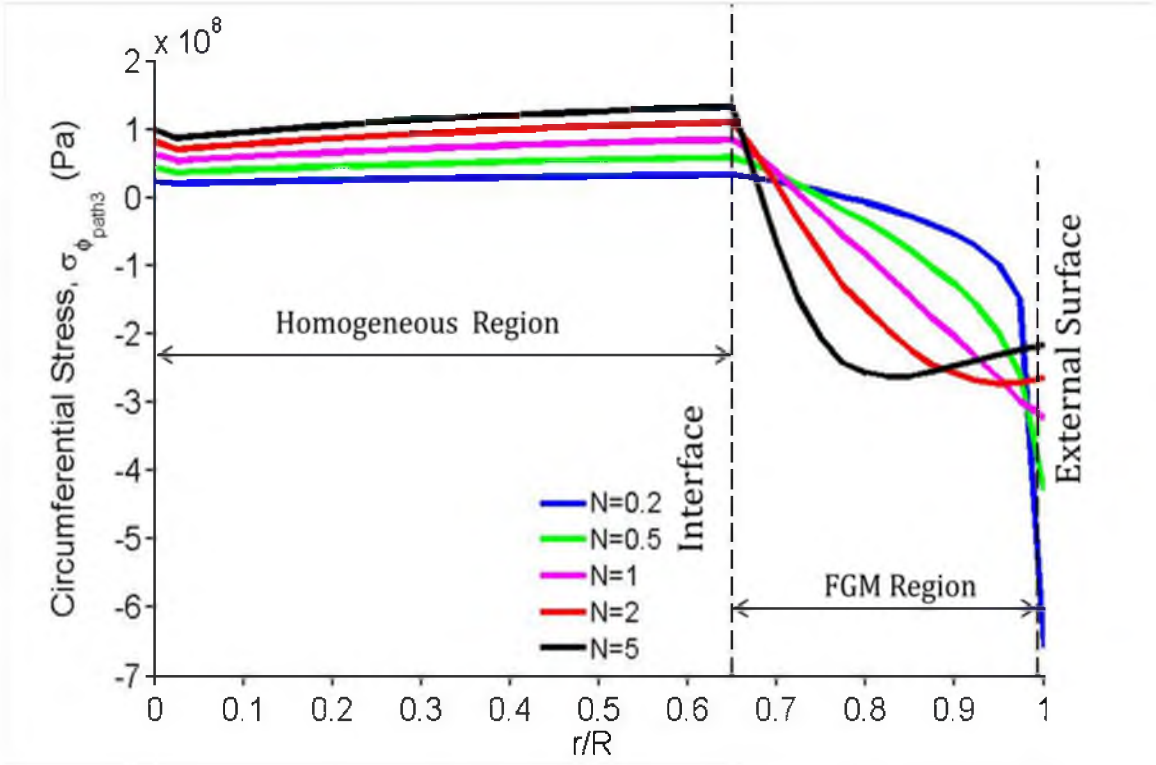

Figure 4.30 Through-the-radius circumferential stress, $\sigma_{\varphi_{path3}}$, along path 3 as a function of normalized radius for different gradient profiles, where H/R=1/3.

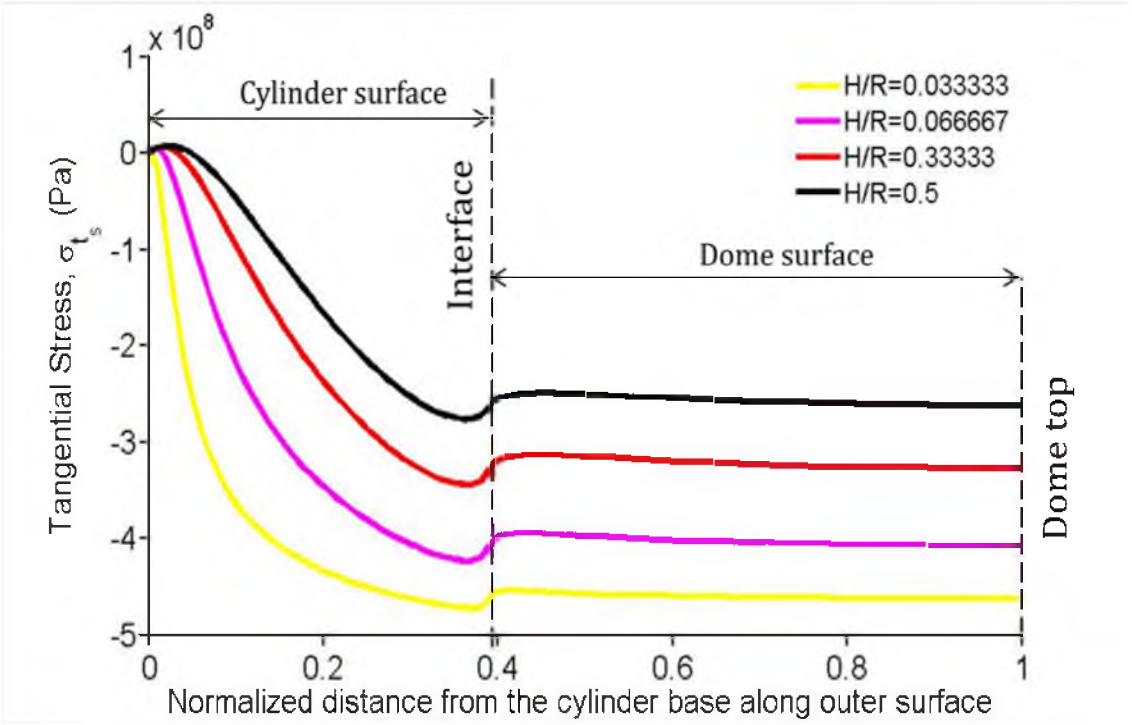

Figure 4.31 Distribution of tangential stress, σ_{t_s}, along the surface, path1, of dome-top compound as a function of position for different gradient thicknesses, where N=1.

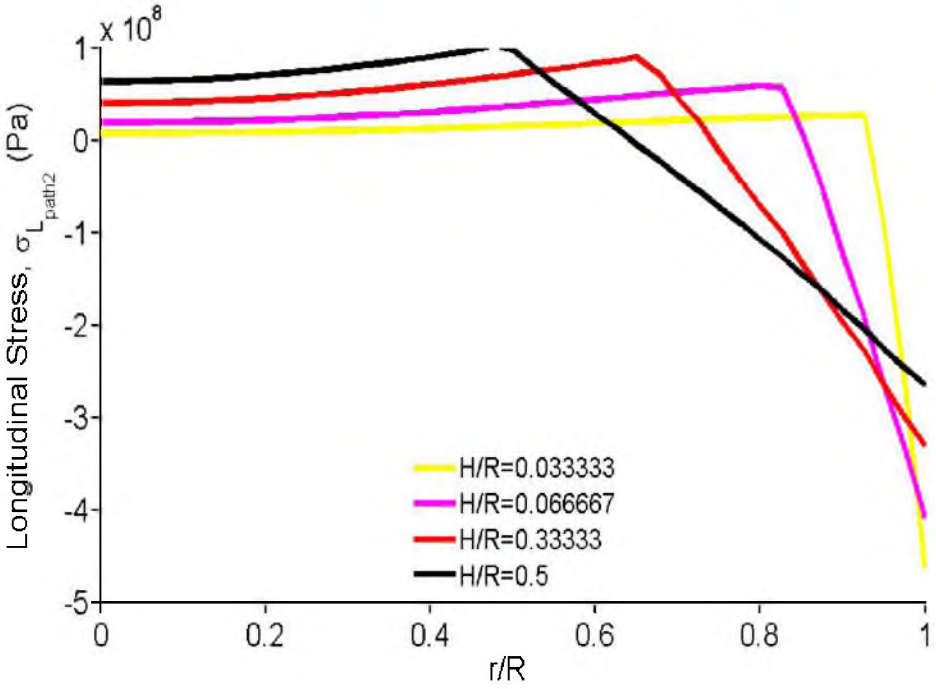

Figure 4.32 Through-the-radius longitudinal stress, σ_{Lpath2}, along path 2 as a function of normalized radius for different gradient thicknesses, where N=1.

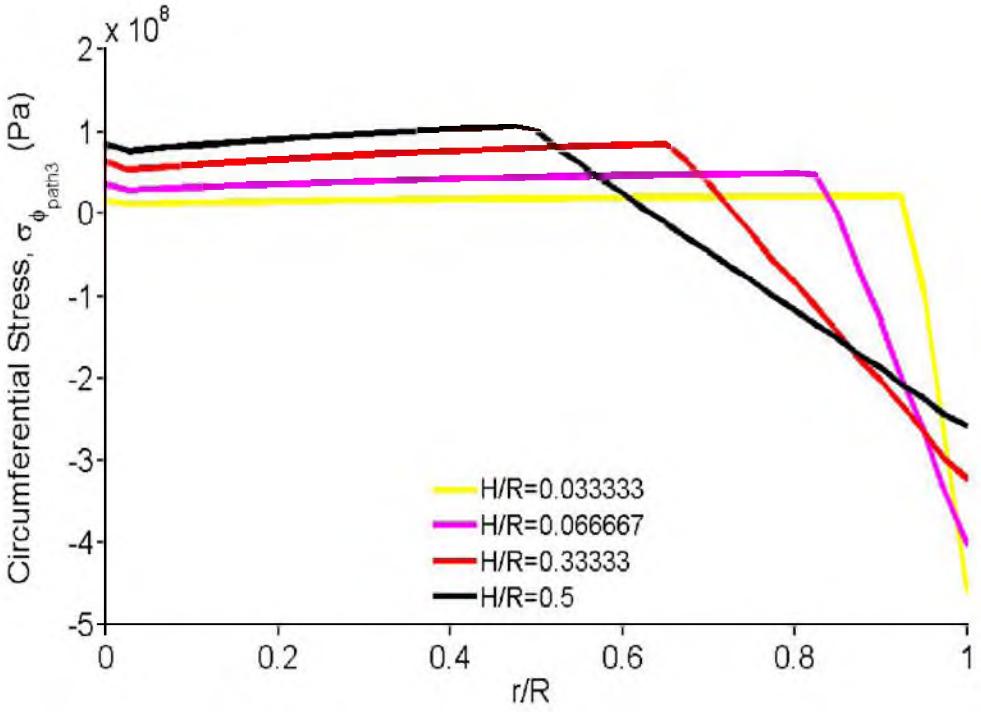

Figure 4.33 Through-the-radius circumferential stress, $\sigma_{\varphi_{path3}}$, along path 3 as a function of normalized radius for different gradient profiles, where *H/R*=1/3.

CHAPTER 5

CONCLUSION

To achieve a reliable method for predicting residual stress distribution in the FGM plate, an FEA model was developed, and then verified by an analytical method. Residual stress distributions for three gradient profiles were plotted for selected N values, and it was shown that the stress distributions were highly dependent on the gradient profile, represented by the exponent, N. As a result, lower N values corresponded to higher compressive stress at the surface, which is desirable for cutting tool performance.

The designed FEA model was employed to simulate the layer removal technique, and the results were compared with those from experimental findings, as well as with the analytical method. The integrity of the mathematical approach was then evaluated by comparing values for $\varepsilon_m(\delta)$ acquired from the simulated layer removal technique with those obtained from the analytical method. It was demonstrated that results from both numerical and analytical methods effectively predicted strain in FGM WC-Co, and that strain magnitude and its distribution were strongly affected by the composition profiles. Additionally, the analytical layer removal model agreed very well with the FEA layer removal model, thus demonstrating that analytic equations can be used without FEA modeling and vise versa. Significant variations in back face strain were seen during layer removal of the FGM, indicating that the experimental approach was sufficiently sensitive

for validation of the FEA and analytical methods. The experimental back face strain was in general agreement with back face strain from FEA. This confirms that analytical theory can be employed to determine residual stresses from back face layer removal.

Since the FEA model was verified and validated with analytical and experimental methods, respectively, FEA was examined for more complex geometries. An analysis of thermal residual stresses in a compound cylinder composed of a functionally graded material (FGM) surrounding a homogeneous core was presented. Residual stress distribution as a function of the radius, based on the specific geometry and boundary conditions studied, was derived in the form of a mathematical equation. The analytical solution was applied to the WC-Co cylindrical compound structure, and different gradient profiles and gradient thicknesses were studied.

The effect of the gradient profile on radial stress and hoop stress showed that different stress components were fairly sensitive to the gradient profile. Radial stress at the surface of the cylindrical compound is always zero, however, its magnitude at the interface of the homogeneous core and the FGM region is particularly relevant, because of the critical role these stresses play in radial crack production, an effect potentially detrimental to the interface and to tool performance. The normalized radial stress of each profile with respect to its radial stress value at the interface revealed that the general distribution of the radial stress was less sensitive to the gradient profile than to its magnitude.

An examination of the effect of different gradient profiles showed that with excess Co content in the FGM region, compressive radial stresses were created, while with decreased Co content in the graded region, tensile stresses were generated at the

interface. Increased cobalt also created tensile hoop stresses in the homogeneous region and compressive hoop stress in the FGM region. The effect of gradient thickness was shown to have a greater effect on radial stress, compared to hoop stress, and increasing the gradient thickness significantly increased the magnitude of the radial stress. The magnitude of the hoop stress changed more gradually, particularly when the gradient thickness was smaller than the homogeneous thickness, which is typical in the microstructures of most tools and applications. For gradient regions thicker than the homogenous region, a situation which was examined for academic rather than practical interest, hoop stress varied more abruptly. In general, the distribution of residual stress in these materials was more sensitive to the gradient thickness than to the gradient profile.

REFERENCES

[1] S. Suresh, A. Mortensen, Fundamental of functionally graded materials: Processing and Thermo-mechanical Behavior of Graded Metals and Metal-Ceramic Composites, third ed., IOM Communications ltd, London (1998).

[2] A.J. Markworth, K. S. Ramesh, W. P. Parks, J. Mater. Sci. 30 (1995) 2183-2186.

[3] N. Noda, J. Therm. Stresses 22 (1999) 477-512.

[4] V. Birman, L.W. Byrd, Appl. Mech. 60 (2007) 195–216.

[5] Z. Fang, G. Lockwood, A. Griffo, Metall. Trans. A. 30A (1999) 3231-3238.

[6] B. Roebuck, E. A. Almond, Int. Mater. Rev. 33 (1988) 90-110.

[7] Z.Z. Fang, P. Fan, J. Guo, U.S. Patent, US20110116963 (2011).

[8] X. Wang, K.S. Hwang, M. Koopman, Z.Z. Fang, L. Zhang, Int. J. Refract. Met. H, 36 (2013) 46-51.

[9] D.N. French, J. Amer. Cer. Soc. Part I 52(5) (1969) 267-271.

[10] D.N. French, J. Amer. Cer. Soc. Part II 52(5) (1969) 271-275.

[11] A.D. Krawitz, M.L. Crapenhoft, D.G. Reichel, R. Warren, Mater. Sci. Eng. A. 105 (1988) 275–281.

[12] D. Mari, A.D. Krawitz, J.W. Richardson, W. Benoit, Mater. Sci. Eng. A. 209(1-2) (1996) 197–205.

[13] D.L. Coats, A.D. Krawitz, Mater. Sci. Eng. A. 359 (2003) 338–342.

[14] D. Delfosse, N. Cherradi, B. Ilschner, Compos. Part B. 28B (1997) 127–141.

[15] C. Larsson, M. Ode´n, Int. J. Refract. Met. H. 22 (2004) 177–184.

[16] D. Rosenthal, J.T. Norton, Weld. J. 24 (1945) 295S-307S.

[17] R.T.R. McGrann, E.F. Rybicki, J.R. Shadley, ASM Internationa TSS (1997).

[18] M.P.I.M. Eijpe, P.C. Powell, Compos. Struct. 37(314) (1997) 335-342,

[19] A.V. Virkar, J.F. Jue, J. Am. Ceram. Soc. 71(3) (1988) 148-151.

[20] K. S. Ravi Chandran, L. Tahvillian and Z. Fang, (2012) unpublished manuscript.

[21] L. Xian-Fang, P. Xu-Long, J. Elast. 96 (2009) 81-95.

[22] G.J. Nie, R.C. Batra, J. Elast. 99 (2010) 179-201.

[23] T. Hirai, L. Chen, Mater. Sci. Forum 308-311 (1999) 509-512.

[24] U. Leushake, Y. Y. Yang, W. Schaller, Mater. Sci. Forum 308-311 (1999) 936-938.

[25] F. Watari, A. Yokoyama, F. Seso, M. Uo, Kawasaki, Composites Part B, 28B (1997) 5-8.

[26] A. Tampieri, G. Celotti, S. Sprio, A. Delcogliano, S. Franzese, Biomaterials 22 (2001) 1365-1367.

[27] C. C. Ge, J. T. Li., Z. J. Zhou, W. B. Cao, W. P. Shen, M. X. Wang, N. M. Zhang, X. Liu, Z. Y. Xu, J. Nuc. Mat. 283-287 (2000) 1116-1119.

[28] N. Cherradi, A. Kawasaki, M. Gasik, Compos. Eng. 4 (1994) 883-885.

[29] A. Mortensen, S. Suresh, Int. Mater. 40 (1995) 239-243.

[30] A. Neubrand, J. Z. Roedel, Metallkd 88 (1997) 358-360.

[31] B. Kieback, A. Neubrand, H. Riede, Mat. Sci. Eng. 362 (2003) 81-84.

[32] W. E. Windes, Thesis (Ph.D.) University of Idaho, (2003).

[33] Z.Z. Fang, ASM Handbook, ASM International, Materials Park, OH (1998).

[34] G.S. Upadhyaya, Cemented Tungsten Carbides - Production, Properties, and Testing, Noyes, New Jersey (1998).

[35] U.K.R. Fischer, E.T. Hartzell, J. Akerman, US Patent No.4743515, (1988).

[36] U.K.R. Fischer, E.T. Hartzell, J. Akerman, US Patent No.4820482, (1989).

[37] J. Akerman, U.K.R. Fischer, E.T. Hartzell, US Patent No.5453241, (1995).

[38] R. Tucker, Metal Powder Report 47 (1992) 48-50.

[39] P. Fan, Z.Z. Fang, Int. J. of Refrac. Met.H. 27(1) (2009) 37-42.

[40] P. Fan, J. Guo, Z.Z. Fang, Int. J. Refract. Met. H. 27(2009) 256-260.

[41] N. Boonyachut, Thesis (Ph.D.) University of Utah, (1993).

[42] I.C. Noyan, J.B. Cohen, Residual Stress Measurement by Diffraction and Interpretation, Springer-Verlag, New York (1987).

[43] W.A. Kaysser (ed), Proc. of the 5th Int. Symp. on Func. Graded Mater., New Town Hall, Dresden, Germany, October 26-29, (1998).

[44] Y. Miyamoto, W.A. Kaysser, B.H. Rabin, A. Kawasaki, R.G. Ford, Functionally Graded Material: Design, Processing and Applications, Kluwer Academic Publishers, Boston (1999).

[45] R. L. Williamson, B. H. Rabin and G. Byerly, FGM 94, Switzerland, (1995).

[46] B. L. Dalgleish, M.C. Lu, A.G. Evans, Acta. Metall. 36(8) (1988) 2029-2035.

[47] B. L. Dalgleish, K. P. Trumble, A. G. Evans, Acta. Metall., 37(7) (1989) 1923-1931.

[48] J. R. Cavanagh, K. R. Cross, R. L. Newman, W.C. Spicer, AIAA/ASME/SAE 13th structures, Structural, Dynamics and Materials Conference, San Antonio, Texas (1972)

[49] F. Nogata, W.A. Kaysser, Trans. Tech. Publications (1998) 331-332.

[50] V. Birman, Composites Eng. 5 (1995) 913–921.

[51] V. Birman, Smart Mater. Struct. 6 (1997) 278–286.

[52] H.M. Yin, L.Z. Sun, G. H. Paulino, Acta Mater. 52 (2004) 3535–3543.

[53] H. E. Exner, Int. Met. Rev. 4 (1979) 149-155.

[54] J. Gurland, J. D. Knox, Tungsten and Refractory Metals, third ed., Metal Powder Industries Federation, Princeton (1996).

[55] G.S. Upadhyaya, Cemented Tungsten Carbides Production, Properties, and Testing, Noyes (1998).

[56] C.S. Kim, Thesis (Ph.D) Carnegie Mellon University, (2006).

[57] C. Colin, L. Durant, N. Favrot, J. Besson, G. Barbier, F. Delannay, Int. J. Refract. Met. H. 12 (1993) 145-148.

[58] M.S. Greenfield, US Patent No. 5623723, (1997).

[59] S. Put, J. Vleugels, O. Van der Biest, Scripta Mater. 45 (2001) 1139-1141.

[60] M. Tokita, Mater. Sci. Forum 39 (2003) 423-425.

[61] T. Li, G.F. Li, J.Y.H. Fuh, P.C. Yu, Int. J. Refract. Met. H. 27 (2009) 95-97.

[62] D. Bolton, R.J. Keely, Int. J. Refract. Met. H. 1 (1982) 103-105.

[63] K.H. Cho, J.W. Lee, I.S. Chung, Mater. Sci. Tech. A209 (1996) 298-300.

[64] P. J. Withers, H. K. D. H. Bhadeshia, Mater. Sci. Tech. 17 (2001) 366-374.

[65] T. Hirano, K. Wakashima, MRS Bull. 20 (1995) 40-42.

[66] M. Koizumi, Ceram. Eng. Sci. Proc.13 (1992) 333-335.

[67] R. L. Williamson, B. H. Rabin, J. T. Drake, J. Appl. Phys. 74 (1993) 1310-1314.

[68] A. E. Giannakopoulos, S. Suresh. M. Finot, M. Olsson, Acta Metall. Mater. 43, (1995) 1310-1312.

[69] F. Erdogan, A. C. Kaya, P. F. Joseph, J. Appl. Mech. 58 (1991) 400-404.

[70] F. Erdogan, Comp. Eng. 5 (1995) 753-755.

[71] A. S. Kim, S. Suresh, C. F. Shih, Intl. J. Solids Struct. 34 (1997) 3415-3420.

[72] A. S. Kim, J. Besson, A. Pineau, Intl. J. Solids Struct. 36 (1999) 1845-1847.

[73] S. Suresh, Science 292 (2001) 2447-2451.

[74] N. Cherradi, P. Moeckli, K. Dollmeier, FGM 94, Switzerland, (1995).

[75] H.E. Pettermann, E. Weissenbek, S. Suresh, in Proceedings of the 4th Symposium on Functionally Graded Materials, Tsukuba, Japan (1996).

[76] V. Teixeira, M. Andritschky, D. Stover, Mater. Sci. Forum 308-311 (1999) 930-935.

[77] M. Gasik, M. Firman, M. Kambe, Ceram. Trans. 114 (2001) 553-555.

[78] B. H. Rabin, R. L. Williamson, H. Bruck, X. L. Wang, T. R. Watkins, Y. Z. Feng, D. R. Clarke, J. Am. Ceram. Soc. 81(6) (1998) 1541-1544.

[79] S. Suresh, A. E. Giannakopoulos, J. Alcala, Acta. Mater. 45(4) (1997) 1307-1321.

[80] D. Rosenthal, J. T. Norton, Weld. J. 24 (1945) 295S- 307S.

[81] R. G. Treuting, W. T. Read, J. Appl. Phys. 22 (1951) 130-132.

[82] W. T. Read, J. Appl. Phys. 22 (1951) 415-419.

[83] P. So, L. J. Broutman, Polym. Eng. Sci. 16 (1976) 185-191.

[84] D.P, Russel, P.W.R. Beaumont, J. Mater. Sci. 15 (1980) 208-212.

[85] A. Siegmann, A. Buchman, S. Kenig, Polym. Eng. Sci. 21 (1981) 997-1000.

[86] A.I. Isayev, C.A, Hieber, D.L. Crouthamel, SPE 39th ANTEC, Boston (1981).

[87] L.D. Coxon, J.R. white, J. Mater. Sci. 14 (1979) 1114-1120.

[88] G.J. Sandilands, J.R. White, Polymer 21 (1980) 338-341.

[89] B. Hawortg, G.J. Sandilands, J.R. White, Plast. Rubb. Int. 5 (1980) 109-111.

[90] C.S. Hindle, J.R. White, D. Dawson, W.J. Greenwood, K. Thomas, SPE 39th ANTEC, Boston (1981).

[91] T. Mura, H. Yoshimoto, J. Appl. Phys. 29 (1958) 115-117.

[92] F. O. Rathbun, L. F. Coffin, J. Exp. Mech. (1966) 519-521.

[93] B. R. Lake, F. J. Appl, C. W. Bert. J. Exp. Mech. (1970) 233-239.

[94] J.R. White, J. Mater. Sci. 20 (1985) 2377-2387.

[95] M.W.A. Paterson, J.R. White, J. Mater. Sci. 20 (1989) 3521-3528.

[96] W. Cheng, I. Finnie, J. Exp. Mech. (1986) 150-154.

[97] K. Feja, V. Hauk, W.K. Krug, Mater. Sci. Eng. 92 (1987) 13-21.

[98] A.V. Virkar, J.F. Jue, J. Am. Ceram. Soc. 71(3) (1988) 148-151.

[99] SAE Information Report, Methods of Residual Stress Measurement, SAE J936, (1965).

[100] D.J. Greving, J.R. Shadley, E.F. Rybicki, ASM Inter. 3(4) (1994) 639-645.

[101] D.J. Greving, E.F. Rybicki, J.R. Shadley, ASM Inter. 3(4) (1994) 379-388.

[102] M.P.I.M. Eupe, P.C. Powell, J. Thermoplast. Compos. Mater. 10 (1997) 334-352.

[103] F. R. Edmund, ASM International T.S.S. AP MP001-022002 (2002).

[104] R.M. Giannakopulos, S. Suresh, M. Olsson, Acta Metall. Mater. 43(3) (1995) 1335-1338.

[105] M. Koizumi, Ceram. Eng. Sci. Proc. 13 (1992) 333-335.

[106] J.R. Cho, J.T. Oden, Comput. Methods Appl. Mech. Eng. 188 (2000) 17-20.

[107] Y. Tomata, K. Kukori, K. Mori, T. Tamura, Mater. Sci. Eng. 24 (1976) 85.

[108] T. Mori, K. Tanaka, Acta Metall. 21 (1973) 571-574.

[109] K. Wakashima, H. Tsukamoto, Mater. Sci. Eng. A. 146 (1991) 291-293.

[110] K.S. Ravichandran, J. Am. Ceram. Soc. 77(5) (1994) 1178-1180.

[111] R.M. Christensen, Mechanics of Composite Materials, Wiley, New York (1979).

[112] R. Hill, J. Mech. Phys. Solids 11 (1963) 357-360.

[113] Z. Fan, P. Tsakiropoulos, A. P. Miodownik, J. Mater. Sci. 29 (1994) 141-143.

[114] K. Wakashima, T. Hirano, M. Niino, European Space Agency (1990).

[115] R. L. Williamson, B. H. Rabin, J. T. Drake, J. Appl. Phys. 74 (1993) 1310-1313.

[116] L. D. Croce, P. Venini, Comput. Methods Appl. Mech. Eng. 193 (2004) 705–725.

[117] S. Pitakthapanaphong, E. P. Busso, J. Mech. Phys. Solids 50 (2002) 695–716.

[118] K.S. Na, J.H. Kim, J. Therm. Stresses 29 (2006) 245–261.

[119] K.S. Na, J.H. Kim, Composites Part B 35 (2004) 429– 437.

[120] M. Jabbari, S. Sohrabpour, M.R. Eslami, Int. J. Pres. Ves. Pip. 79 (2002) 493-497.

[121] L. Xian-Fang, P. Xu-Long, J. Elast. 96 (2009) 81-95.

[122] G.J. Nie, R.C. Batra, J. Elast. 99 (2010) 179-201.

[123] M.P. Lutz, R.W. Zimmerman, Thermal Stress, 19 (1996) 39-54.

[124] Y. Obata, N.Noda, Thermal Stress, 10 (1995) 335-338.

[125] Y. Obata, N.Noda, Thermal Stress, 17 (1994) 471-487.

[126] N. Tutuncu, M. Ozturk, Composites Part B 32 (2001) 683-686.

[127] K. S. Ravichandran, Mater. Sci. Eng A 201 (1995) 269-273.

[128] R.M. Christensen, Mechanics of Composite Materials, Wiley, New York, (1981).

[129] J. R. Cho, D. Y. Ha, Mater. Sci. Eng. A 302 (2001) 187–196.

[130] Y. Tomata, K. Kukori, K. Mori, T. Tamura, Mater. Sci. Eng. 24 (1976) 85-88.

[131] T. Mori, K. Tanaka, Acta Metall. 21 (1973) 571-574.

[132] K. Wakashima, H. Tsukamoto, Mater. Sci. Eng. A 146 (1991) 291-295.

[133] K.L. Choy, E. Felix, Mater. Sci. Eng. A 278 (2000) 162–169.

[134] K. A. Khor, Y. W. Gu, Mater. Sci. Eng. A 277 (2000) 64–76.

[135] J. N. Reddy, Int. J. Numer. Mech. Engng. 47 (2000) 663–684.

[136] Z. Q. Cheng, R. C. Batra, Arch. Mech. 52 (2000) 143–158.

[137] Z. Q. Cheng, R. C. Batra, J. Sound Vib. 229 (2000) 879–895.

[138] Z. Q. Cheng, R. C. Batra, Composites Part B 31 (2000) 97–106.

[139] C. T. Loy, J. N. Reddy, K. Y. Lam, Inter. J. Mech. Sci. 41 (1999) 309–324.

[140] S. S. Vel, R. C. Batra, Inter. J. Solids Struct. 40 (2004) 7187–7196.

[141] S. S. Vel, R. C. Batra, J. Sound Vib. 272 (2004) 703–730.

[142] Z. H. Jin, R. C. Batra, J. Mech. Physics Solids 44 (1996) 1221–1235.

[143] Z. H. Jin, R. C. Batra, J. Therm. Stresses 19 (1996) 317–339.

[144] Z. H. Jin, R. C. Batra, Mater. Sci. Eng. A2 42 (1998) 70–76.

[145] S. S. Vel, R. C. Batra, AIAA J. 40 (2002) 1421–1433.

[146] S.P. Timoshenko, J.N. Goodier, Theory of Elasticity, 3rd ed. McGraw-Hill, (1970) 433-439.

[147] J. Guo, P. Fan, X. Wang, Z.Z. Fang, Int. J. Powder Metall. 47(3) (2011) 55-62.

[148] J Guo, Z.Z. Fang, P. Fan, X. Wang, Acta Mater. 59 (2011) 4719–4731.

[149] S. Timoshenko, J.N. Goodier, Theory of Elasticity. McGraw-Hill, (1970) 273-283

[150] M. Jabbari, S. Sohrabpour, M.R. Eslami, J. Appl. Mech. 70(1) (2003) 111-118.

[151] J.R. Barber, Elasticity, Kluwer Academic Publisher, Durdrecht, The Netherlands (1992).